

國立交通大學

電機與控制工程研究所

碩士論文

SOI 基板上利用 SU-8 機構組裝之三維微結構

**Assembly of Three Dimensional  
Microstructures on SOI Wafers Using SU-8  
Mechanisms**

研究生：黃煒智

指導教授：邱一 博士

中華民國九十六年十月

SOI 基板上利用 SU-8 機構組裝之三維微結構

**Assembly of Three Dimensional  
Microstructures on SOI Wafers Using SU-8  
Mechanisms**

研 究 生:黃煒智

Student: Wei Zhi Huang

指 導 教 授:邱一

Advisor: Yi Chiu

國立交通大學 電機學院

電機與控制工程研究所

碩士論文

A Thesis

Submitted to Department of Electrical and Control Engineering

College of Electrical and Computer Engineering

National Chiao Tung University

In Partial Fulfillment of the Requirement

For the Degree of

Master

In

Electrical and Control Engineering

October 2007

Hsinchu, Taiwan, R.O. C

中華民國九十六年十月

## 中文摘要

近年來在半導體產業的發展之下，微機電製程技術有許多重大的發展，而在許多應用領域中對於三維微結構的要求更是甚多。如何使三維微結構的製造更加有效率且能夠有良好的定位功能是我們的目標。

因為我們所製作的結構最終目標是要應用在光學系統方面，因此採用應力幾乎為零且結構較厚的 SOI (Silicon On Insulator) 基板製作微鏡面，避免一般利用多晶矽製作時可能發生的翹曲現象，並且整合 SU-8 以製作其他所需的微結構。由於 SU-8 有良好的機械特性和低溫製程，使得往後的電路整合更加容易。

我們提出了 one-push 式的三維微結構組裝方式來簡化組裝複雜度。也就是只要經過一個探針下壓的動作就可以完成組裝。由於結構的定位準確性和結構上的蝕刻孔對於光學上的應用會造成很大的影響，因此我們提出了一種 V 型絞鏈的新設計來增加組裝結構的定位準確性。另外，為了消除在表面微加工中常出現的蝕刻孔，我們也利用背向乾蝕刻的方式去解決此問題。

在論本文中，我們成功的製造並組裝出上述的元件，其可行性已經獲得證實。而面臨的問題(例如彈簧結構設計不良)和改善方向也將會討論，以利之後對光學系統的制作和電路整合上的要求。

## Abstract

Recently, the Micro Electro Mechanical Systems (MEMS) technology has many important developments with the rapid progress in the semiconductor industry. In many applications, there is demand for three-dimensional (3-D) structures. More effective assembly technique and positioning accuracy are needed for 3-D microstructures.

In this thesis, the silicon on insulator (SOI) wafers with almost zero stress are used in order to prevent the stress-induced curvature in micro devices made of poly silicon for optical applications. SU8 has good mechanical property and low temperature process, making it suitable as another structural layer and integration with circuit.

In this thesis, a new assembly approach with one push operation is proposed to reduce the assembly complexity. Namely, all probe manipulation is reduced to a simple one-push operation. A novel V-shaped hinge is used to eliminate the play in traditional hinge designs and therefore improves the positioning accuracy. In order to address the issues with etch holes in surface micromachining, the structure without etch holes is used. The etching from the backside of the substrate is performed.

The feasibility of the proposed one-push assembly process, V-shaped hinge elements and structure without etch holes, is verified in this thesis. The encountered problems, such as the robustness of spring structures, are discussed for further researches.



## 致謝

結束了碩士班的研究生活，謹懷著感激的心謝謝大家，首先要感謝的是我的指導教授邱一博士，他給了我許多很棒的專業指導和建議，帶領我走出錯誤的觀念和認知，使實驗成果能一直順利的進行。再來要感謝博士班企桓學長對我不論在實驗上和觀念上的種種幫助，讓我的實驗能正確的執行下去，真的非常感謝你。

非常感謝我的口試委員，邱俊誠主任、方維倫老師和施錫富老師，能在繁忙之餘對我的論文指導建議和鼓勵，讓我銘記在心。

還有感謝實驗室學長，忠衛、勳哥、炯廷、Z哥和亦謙對我的指導，讓我能銜接你們步伐前進，以及邱俊誠實驗室的同學學長亞書、賢哥、一帆和倪哥，謝謝你們對我在實驗上的建議和幫助。感謝奈米中心徐小姐、黃小姐、陳小姐和葉先生以及機械所的志柏，讓我能迅速的完成許多的製程實驗。

當然，很感動能有繁果、子麟、弘諳、昇儒和昌修這些珍貴的實驗室伙伴，幫助我的論文和一起度過了愉快又另人難忘的實驗室生活

謝謝我爸爸媽媽，在求學的路上全力的幫助我支持我，讓我能無憂無慮的完成我的學業，並且給我永遠的支持，真的非常非常感謝。最後，我也要對很疼我的外婆說：我會永遠想念妳的。

## Table of Content

---

中文摘要.....	i
Abstract.....	ii
誌謝.....	iii
Table of Content.....	iv
List of Figures.....	vi
List of Tables.....	x
<b>Chapter1 Introduction.....</b>	<b>1</b>
1-1 Motivation.....	1
1-2 Literature survey.....	5
1-2-1 Microfabricated hinges.....	5
1-2-2 Scratch drive actuator.....	7
1-2-3 Magnetic force assembly.....	8
1-2-4 Electrostatic force assembly.....	9
1-2-5 Centrifugal force assembly.....	9
1-2-6 Surface tension-powered self-assembly.....	11
1-2-7 Microassembly of 3-D microstructures using microgrippers.....	12
1-2-8 Microassembly of hingeless 90° microstructures.....	14
1-3 Objectives and thesis organization.....	16
<b>Chapter2 Principle and Design.....</b>	<b>18</b>
2-1 Introduction.....	18
2-2 Integration of SOI wafer and SU-8 structural layer.....	21
2-3 Device design.....	22
2-3-1 Assembly process.....	22
2-3-2 Locking mechanism.....	24

2-4 V-shaped hinge.....	28
2-5 Flexible side latch.....	32
2-6 Micromachined mirrors without etch holes.....	35
2-7 Summary.....	36
<b>Chapter3 Fabrication Process .....</b>	<b>37</b>
3-1 Integration of SOI and SU-8.....	37
3-2 Process flow.....	38
3-3 Fabrication problems and discussions.....	49
3-3-1 Adhesion of SU-8 structures.....	49
3-3-2 Vapor HF release.....	52
3-4 Fabricated structure.....	54
3-5 Summary.....	56
<b>Chapter4 Measurement and Experiment Results.....</b>	<b>57</b>
4-1 Assembly experiment.....	57
4-1-1 Feasibility.....	57
4-1-2 Problems during the assembly process.....	60
4-1-3 Assembly time.....	64
4-2 Device measurement.....	65
4-2-1 V-shaped hinge measurement.....	65
4-2-2 Angle measurement.....	66
4-2-3 Optical measurement of mirror without etch holes.....	69
4-3 Summary.....	74
<b>Chapter5 Conclusion and Future Work.....</b>	<b>75</b>
5-1 Conclusion.....	75
5-2 Future Work.....	75
<b>Reference.....</b>	<b>79</b>

## List of Figures

---

Figure 1-1	(a) Anisotropic etching, (b) deep reactive ion etching, (c) isotropic etching.....	2
Figure 1-2	(a) Thin film deposition and photolithography, (b) releasing the structure.....	3
Figure 1-3	(a) X-ray irradiation, (b) development, (c) electroforming of metal structures and mold inserts, (d) replication by molding.....	4
Figure 1-4	(a) On-chip optical-disk pickup head system [8], (b) fractal antenna (c) 4½-turn meander inductors after self-assembly.....	5
Figure 1-5	(a) Fabrication processes of micro hinges, (b) SEM micrograph of a hinged structure .....	6
Figure 1-6	(a) Configuration of the SDA, (b) schematic view of the SDA, (c) schematic principle of step motion of the SDA.....	7
Figure 1-7	Microassembly by magnetic actuation.....	8
Figure 1-8	Sequential assembly by using different volumes of Permalloy.....	8
Figure 1-9	Microassembly by electrostatic force.....	9
Figure 1-10	(a) Schematic of the rotation assembly system, (b) Side view of the hinged structure, (c) SEM micrograph of the batch micro-assembled micromirror arrays.....	10
Figure 1-11	(a) Process flow of surface tension assembly, (b) 45° self-assembled mirror based on photoresist hinges, (c) pyramid enclosure assembled by the surface tension forces of molten solder.....	11
Figure 1-12	(a) Five axis robotic workstation, (b) solder bonded microgripper.....	13
Figure 1-13	Assembly process, (a) bonded microgripper grasps micro-part, (b) move the micro-part to the place of assembly, (c) insert the micro-part into the slot, (d) out-of-plane 3-Dmicroassembly.....	13
Figure 1-14	Hingeless device concept.....	15
Figure 1-15	Schematic assembly sequence.....	15
Figure 1-16	(a) Assembly of the SU-8 structures, (b) SEM image of 90 out-of-plane SU-8 structures.....	15
Figure 2-1	(a) Cross section view of the conventional hinge, (b) SEM image exhibits a large amount of play in the hinge.....	19
Figure 2-2	Side latch plates with V-shaped lock slots to fix the hinged plate.....	20
Figure 2-3	Multiple assembly processes are applied to complete the 3-D structure. The final assembled structure is fixed in position by friction force.....	20
Figure 2-4	(a) Layout of the proposed micromirror device, (b) 3-D solid model of the micromirror device.....	23

Figure 2-5	Assembly process with only one push operation.....	24
Figure 2-6	(a) Layout of the V-shaped hinge, (b) 3-D solid model.....	25
Figure 2-7	3-D view of the V-shaped hinge during assembly process.....	25
Figure 2-8	(a) 3-D solid model of the V-shaped hinge after assembly, (b) cross-section view of the restricted z-direction movement, (c) top view of the positioning mechanism.....	26
Figure 2-9	(a) Layout of the side plate structure, (b) 3-D solid model.....	27
Figure 2-10	Flexible side latch assembly process.....	28
Figure 2-11	Top view of a V-shaped cantilever showing dimensions and load F.....	28
Figure 2-12	Cross-section view of the V-shaped hinge, (a) before release oxide, (b) after release and assembly.....	29
Figure 2-13	Design room for V-shaped element.....	30
Figure 2-14	Simulations of the V-shaped spring (a) x-component of stress, (b) y-component of stress, (c) z-component of stress, (d) Von stress.....	32
Figure 2-15	Four types of springs, (a) serpentine spring, (b) box spring, (c) meander spring, (d) skewed box spring.....	34
Figure 2-16	An example of box springs.....	34
Figure 2-17	Cross-section view of the side latch.....	35
Figure 2-18	Backside pattern with a large open hole.....	36
Figure 2-19	Backside pattern with a pillar array.....	36
Figure 3-1	Schematic of a 90° micromirror.....	38
Figure 3-2	Fabrication process of the proposed device.....	44
Figure 3-3	Photographs of the device structures during the fabrication process.....	47
Figure 3-4	(a) The mirror plate is lifted by a probe, (b) as the plate is lifted further, the weak SU-8 anchor is detached.....	50
Figure 3-5	Experimental process of SU-8 adhesion test.....	51
Figure 3-6	Assembly failure due to the stiction.....	52
Figure 3-7	Schematic illustration of a vapor HF release apparatus. The chip is placed on a plastic film.....	53
Figure 3-8	Vapor HF setup used in this thesis.....	54
Figure 3-9	SEM photographs of assembled devices.....	55
Figure 4-1	Assembly process of a 90° mirror with conventional hinges.....	58
Figure 4-2	Assembly process of a 90° mirror with V-shaped hinges.....	59
Figure 4-3	Assembly process of a 90° mirror without etch holes.....	60
Figure 4-4	Assembly failure due to spring was too soft(box-type spring).....	61
Figure 4-5	Assembly failure due to springs soft springs(other spring designs).....	62
Figure 4-6	Successful assembly process.....	63
Figure 4-7	Assembly failure due to displaced hinge pins.....	63

Figure 4-8	Bending of the V-shaped hinge after assembly.....	65
Figure 4-9	Bending of the V-shaped hinge after assembly, measured by interferometry.....	66
Figure 4-10	A mirror sample at 89.14° .....	67
Figure 4-11	Reasons of the angle deviation.....	67
Figure 4-12	Big opening pattern causes the bending of the frontside mirror.....	69
Figure 4-13	Mirror curvature of device with the big hole backside pattern.....	69
Figure 4-14	Pillar opening pattern results in flat frontside structure.....	70
Figure 4-15	Mirror curvature of device with the pillar array pattern.....	70
Figure 4-16	Two samples after releasing process, (a) mirror with the big hole backside pattern, (b) mirror with the pillar array pattern.....	71
Figure 4-17	Curvature of the mirror with big hole pattern after releasing.....	72
Figure 4-18	Curvature of the mirror with array pattern after releasing.....	72
Figure 5-1	The concept of batch assembly with one push operation.....	76
Figure 5-2	Micro optical pick-up head.....	76
Figure 5-3	Curvature compensation by stress balance.....	77



## List of Tables

---

Table 1-1	Comparison of assembly method.....	17
Table 2-1	SU-8 material properties and spring geometric parameters.....	30
Table 2-2	Comparison of two V-shaped structures.....	31
Table 3-1	Comparison of process.....	37
Table 3-2	Modified SU-8 parameters.....	50
Table 4-1	Assembly time of 10 samples.....	64
Table 4-2	Angle measurement of 10 samples.....	67



# Chapter 1

## Introduction

### 1-1 Motivation

MEMS (Micro Electro-Mechanical Systems), as its name suggests, is a microfabrication technique for making miniaturized mechanical devices with the sizes of  $\mu\text{m}$  to mm. The mechanical elements, sensors, movable structures, and electronics are integrated on a single silicon substrate through microfabrication technology. The electronics are fabricated using conventional integrated circuit (IC) processing methods (such as CMOS, Bipolar, or BiCMOS processes), and the micromechanical elements are fabricated using compatible micromachining processes. This technology brings together silicon-based microelectronics with micromachined structures, making possible the realization of complete system-on-a-chip (SOC). The main microfabrication technologies for MEMS can generally be categorized into three types, which are, bulk micromachining [1], surface micromachining [2], and LIGA process [3]. A variety of micromechanical devices have been fabricated by these micromachining approaches.

Bulk micromachining fabricates micromechanical components by etching into the substrate material. Several materials can be used as the substrates, such as silicon, quartz, and GaAs. Silicon is the most commonly used substrate material in MEMS. In general, there are two ways to etch silicon, namely, anisotropic etching and isotropic etching. Many liquid etchants possess large etching rate difference in different crystalline directions. Certain crystal planes are etched faster than others, as shown in Figure 1-1 (a). TMAH (tetramethylammonium hydroxide), KOH (potassium



hydroxide), and EDP (ethylenedamine pyrocatochol) are typical anisotropic etchants for silicon etching. Another anisotropic etching technique is deep reactive ion etching (DRIE), as shown in Figure 1-1 (b). It uses a plasma to etch high-aspect-ratio microstructures on the silicon wafer. In contrast to anisotropic etching, isotropic etching etches all directions in the silicon substrates with nearly the same rate. Figure 1-1 (c) shows this feature. Many microstructures have been fabricated by means of bulk micromachining techniques, such as suspended membranes and AFM tips [4].

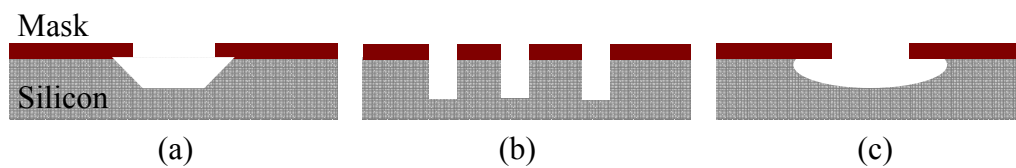


Figure 1-1 (a) Anisotropic etching, (b) deep reactive ion etching, (c) isotropic etching.

Surface micromachining is the microfabrication technique by deposition and etching of thin structural and sacrificial films to form the micromechanical structures. This micromachining technique is based upon the process steps used to produce IC. As shown in Figure 1-2, to make a mechanical element, deposition, photolithography and etching processes are repetitively utilized to achieve the desired patterns. When the underlying “sacrificial layer” is dissolved, the mechanical elements are “freed” except for the support position. Suspended or movable microstructures can be easily constructed by using the sacrificial-layer technology. Surface micromachining is a popular microfabrication approach due to its compatibility with IC processing. Several standard surface micromachining processes, such as MUMPs [5], SUMMiT [6], have been available for the general public users.

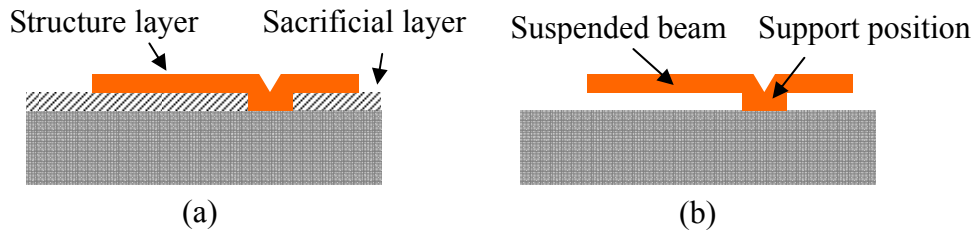


Figure 1-2 (a) Thin film deposition and photolithography, (b) releasing the structure.

LIGA is the abbreviation from the German words, “Lithographie”, “Galvanik”, and “Abformung”, which mean lithography, electroforming, and molding, respectively. It is suitable for making microstructures with depths greater than lateral dimensions. Figure 1-3 illustrates the basic LIGA process. The X-ray resist, such as polymethylmethacrylate (PMMA), is exposed to synchrotron radiation. After exposure and development, the resist is used as a mold for metal electroforming. Nickel, copper, gold, nickel iron, nickel manganese, nickel cobalt, and dispersion-strengthened nickel are commonly used for this electroforming process. The resist structure is then removed and the released metal mold is utilized as a primary mold to create repetitively other final plastic or ceramic microstructures. Although the LIGA technique brings the great ability to construct high aspect ratio structures, some problems still limit its practical application. The biggest problem is the need for an X-ray source. Obviously, it is expensive and unsuitable for laboratory use. Therefore, other LIGA-like processes, such as UV-LIGA, ICP-LIGA, have been developed as the low-cost alternatives [3].

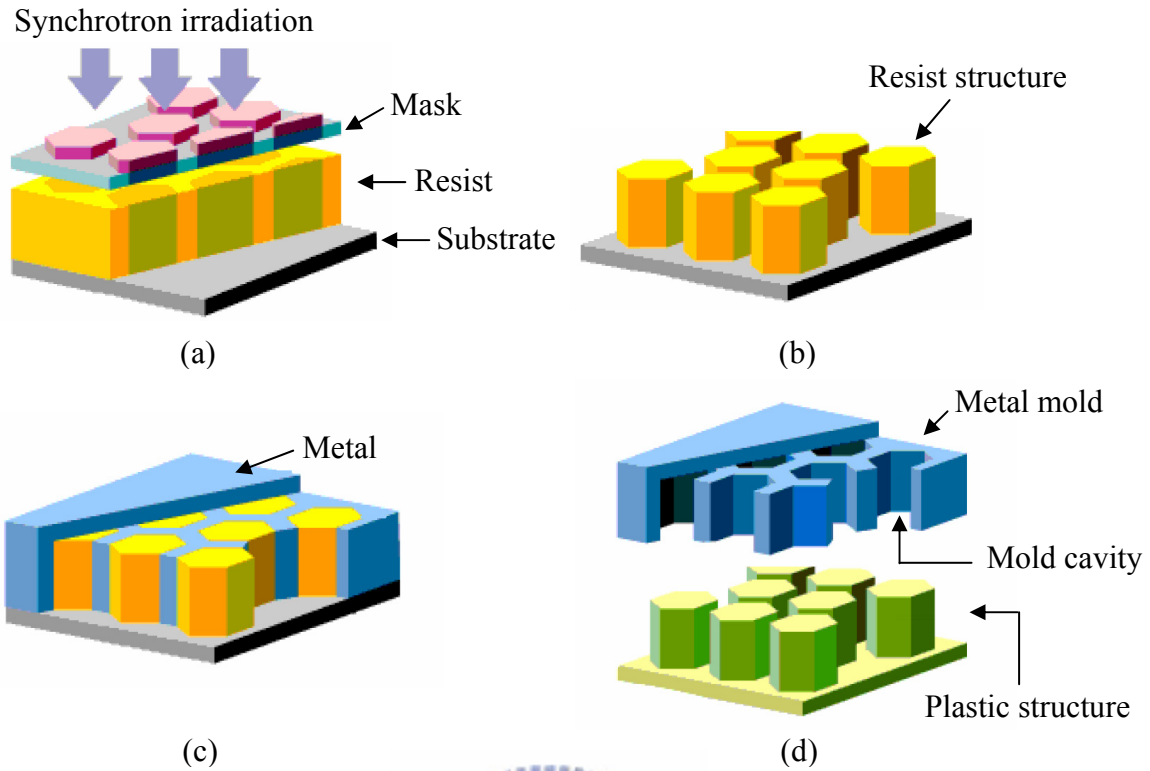
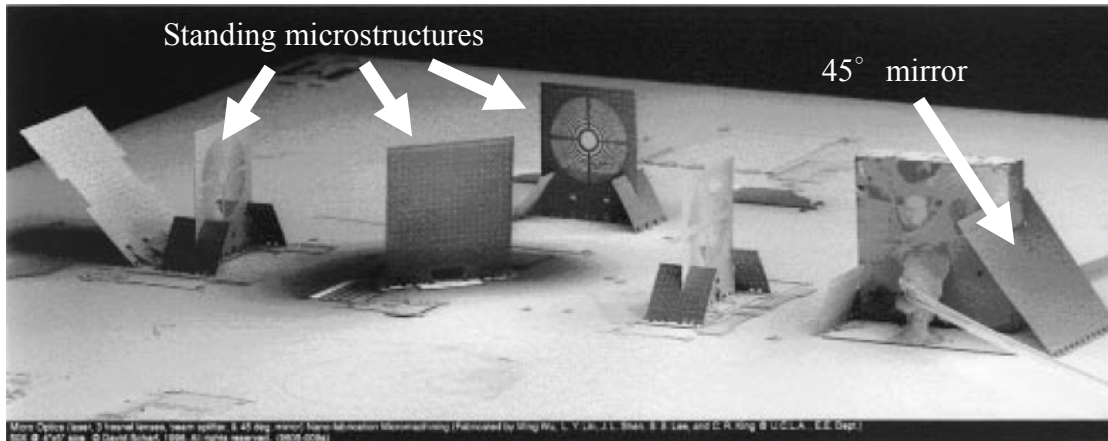
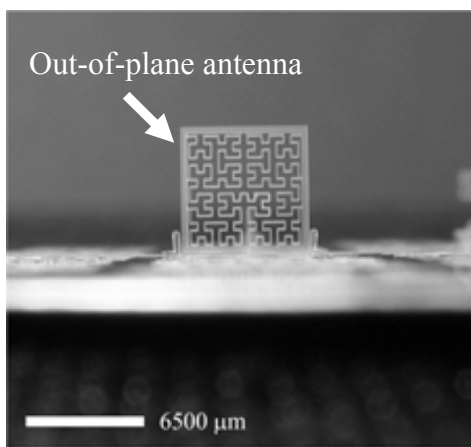


Figure 1-3 (a) X-ray irradiation, (b) development, (c) electroforming of metal structures and mold inserts, (d) replication by molding [3].

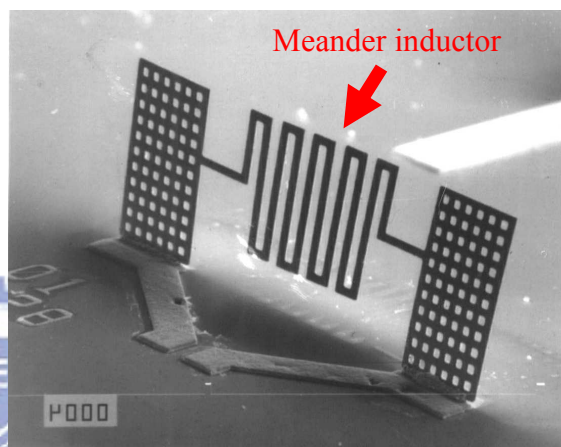
In the past years, MEMS technology has been applied in several fields, including biomedical engineering, optical engineering, and radio frequency devices, etc. In many applications, there is demand for three-dimensional (3-D) structures, such as 3-D coil inductors for wireless communication applications [7] and micromirrors for on-chip optics [8]. Figure 1-4 shows the SEM micrographs of some 3-D microstructures [8-10]. The complexity of the assembly process is very important to 3-D devices. There have been many proposed techniques for the fabrication and construction of complex 3-D components in recent years. However, more effective assembly technique is necessary. Positioning accuracy is also critical to the assembled structures, especially in optics. A new assembly method is desired for reducing the complexity of the assembly process and improving the positioning accuracy of the assembled devices.



(a)



(b)



(c)

Figure 1-4 (a) On-chip optical-disk pickup head system [8], (b) fractal antenna [9], (c) 4½-turn meander inductors after self-assembly [10].

## 1-2 Literature survey

Many researchers have been working on the 3-D assembly techniques. Some techniques for microassembly is reviewed in this section.

### 1-2-1 Microfabricated hinges

One of the most common techniques for manufacturing MEMS devices is surface micromachining. But standard surface micromachining is a planar process which has high planar resolution and limited vertical range (typically less than 5 μm).

These features make surface micromachining suitable for planar applications, but have problems with three-dimensional designs. A common solution is the hinged structures introduced by K. S. J. Pister et al. in the early 90's [11]. The surface micromachined structures with integrated hinges are rotated out of plane with respect to the wafer, and assembled to form complex 3-D components. This microhinge technique improves the lack of surface micromachining for three-dimensional designs. The schematic view of the hinge fabrication process and the SEM micrograph of an assembled device are shown in Figure 1-5.

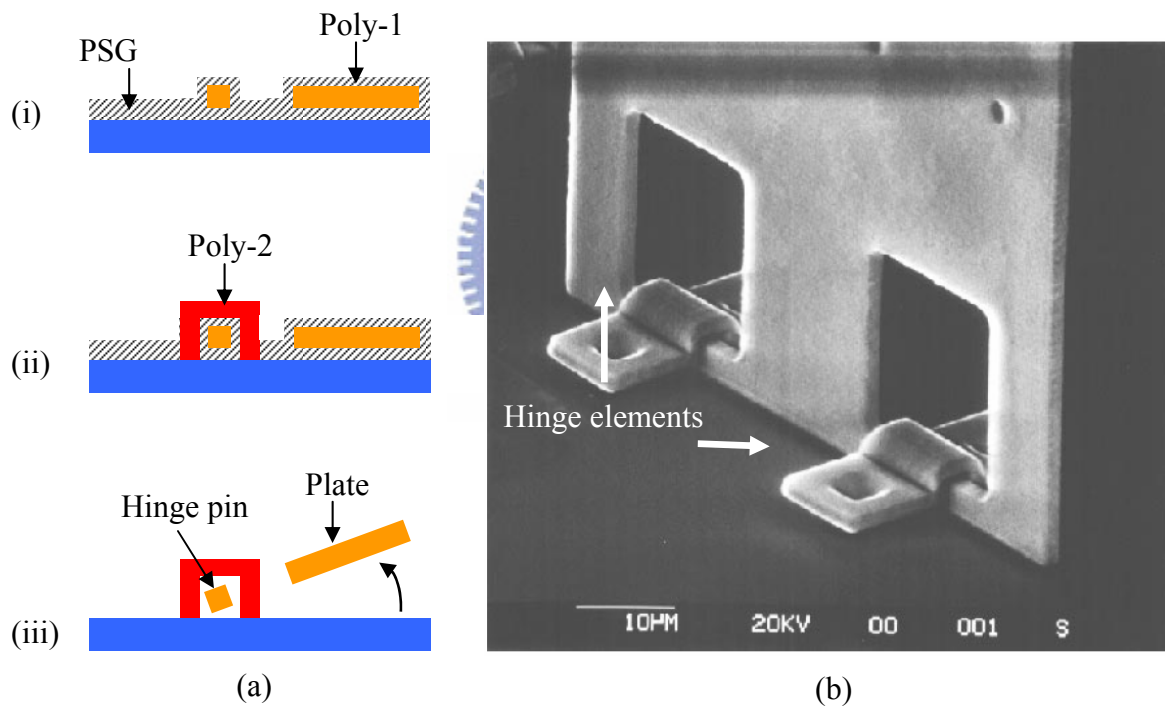


Figure 1-5 (a) Fabrication processes of micro hinges, (b) SEM micrograph of a hinged structure [11].

### 1-2-2 Scratch drive actuator

The scratch drive actuator (SDA), first proposed by T. Akiyama et al. in 1993 [12], is an electrostatic microactuator. As illustrated in Figure 1-6, the SDA consists of the plate, bushing, insulator and substrate electrode. The capacitor-like structure is formed by the plate and the substrate. Once the voltage is on, the plate experiences an electrostatic force that pulls it down toward the substrate. The bushing will be tilted due to the warped plate and thereby gliding toward the edge on the substrate. When the voltage is removed, the plate and bushing return to their original position, but translate forwards by a small distance. By a periodic driving voltage, the SDA can move forward at a velocity and step size determined by the frequency and amplitude of the driving voltage. Figure 1-6 illustrates the structure and the motion principle of the SDA. Using integrated SDA to assemble 3-D microstructure was proposed in [13].

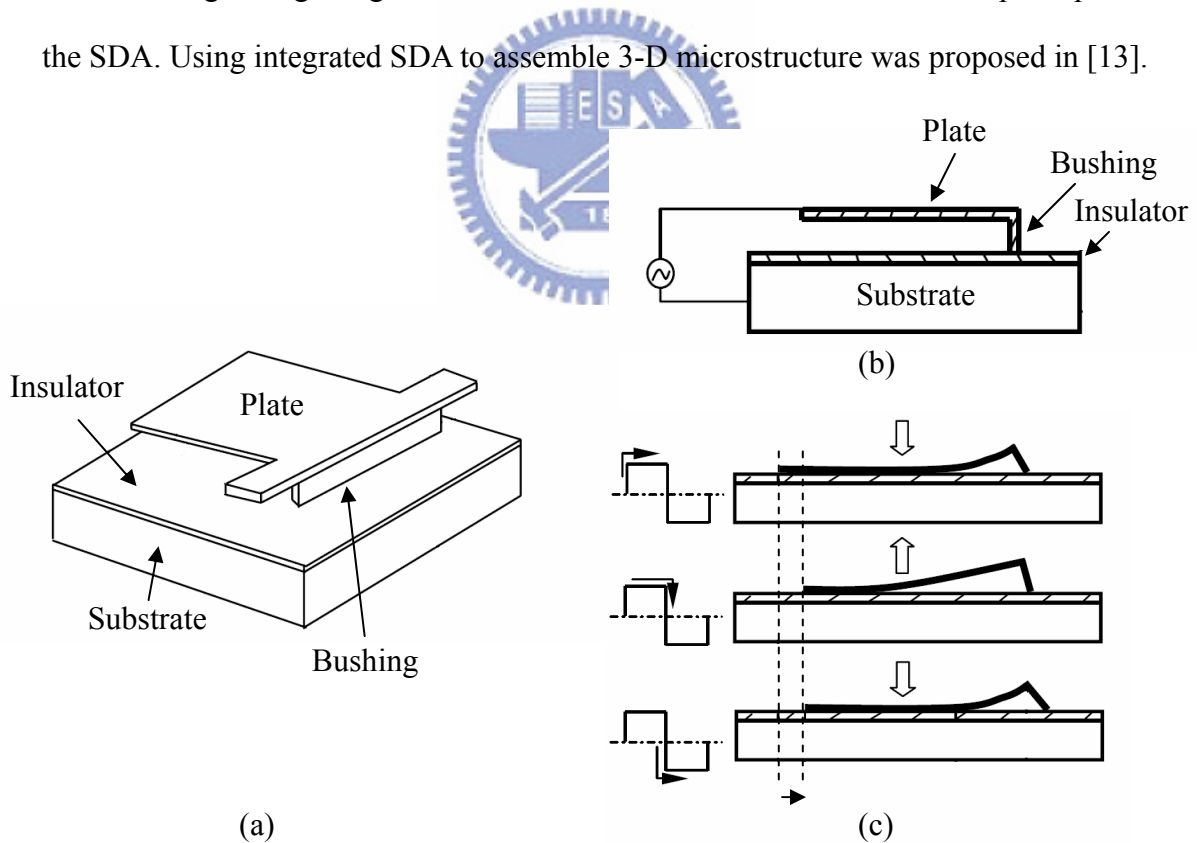


Figure 1-6 (a) Configuration of the SDA, (b) schematic view of the SDA, (c) schematic principle of step motion of the SDA [12].



### 1-2-3 Magnetic force assembly

Figure 1-7 shows the principle of employing the magnetic force to lift hinged surface micromachined plates [14]. Magnetic material (Permalloy) is electroplated on the hinged flap. When an external magnetic field is applied, the magnetic force will make the hinged flap rotate about the pin axis. The rotational angle of the hinged flap is determined by the volume of the magnetic material and the strength of the magnetic field. Figure 1-8 demonstrates an assembled device through a sequence of magnetic actuation approaches. The actuation order is controlled by using different volumes of Permalloy. The primary flap with a larger volume of Permalloy will rise to  $90^\circ$  first. Then the secondary flaps with a smaller Permalloy reach to  $90^\circ$  and lock the primary flap into the upright position.

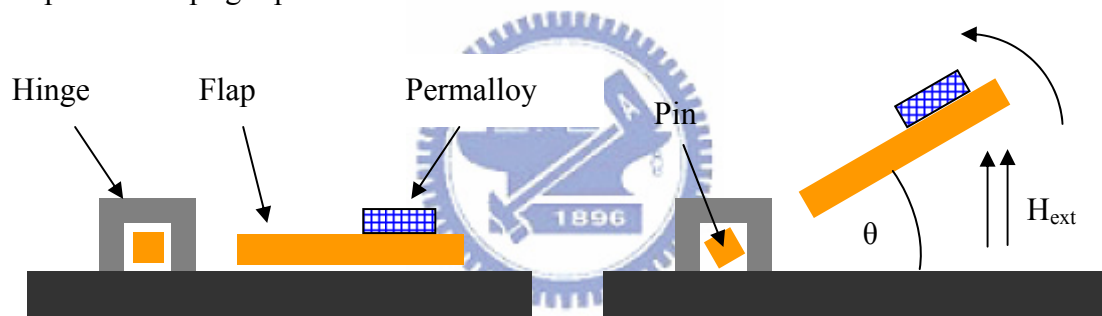


Figure 1-7 Microassembly by magnetic actuation

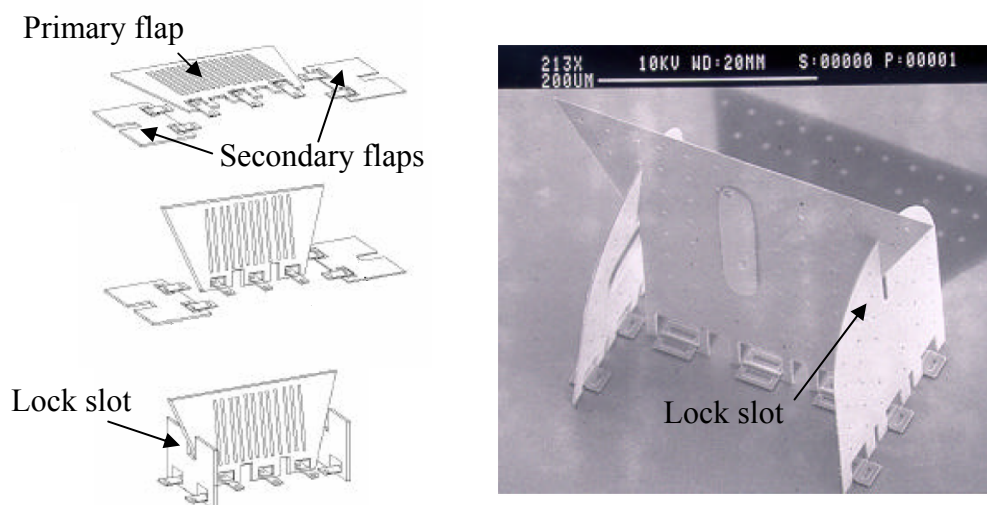


Figure 1-8 Sequential assembly by using different volumes of Permalloy [14].

#### 1-2-4 Electrostatic force assembly

In addition to magnetic force, electrostatic force is also a choice for assembly driving force [15]. Figure 1-9 shows the operation principle of the electrostatic force assembly. The plate, which is free to rotate about pin axis, is held in place by gravity when there is no voltage applied. Once voltage is on, the electric field between the ground plane and the plate are created. By providing a sufficiently strong electric field, the plate can be lifted out of the substrate and assembled in the upright position.

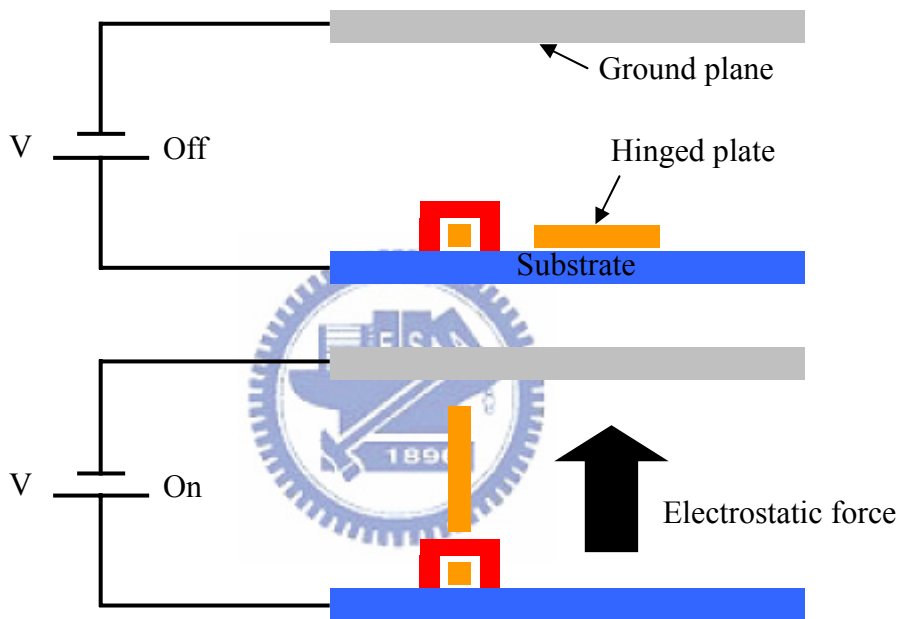


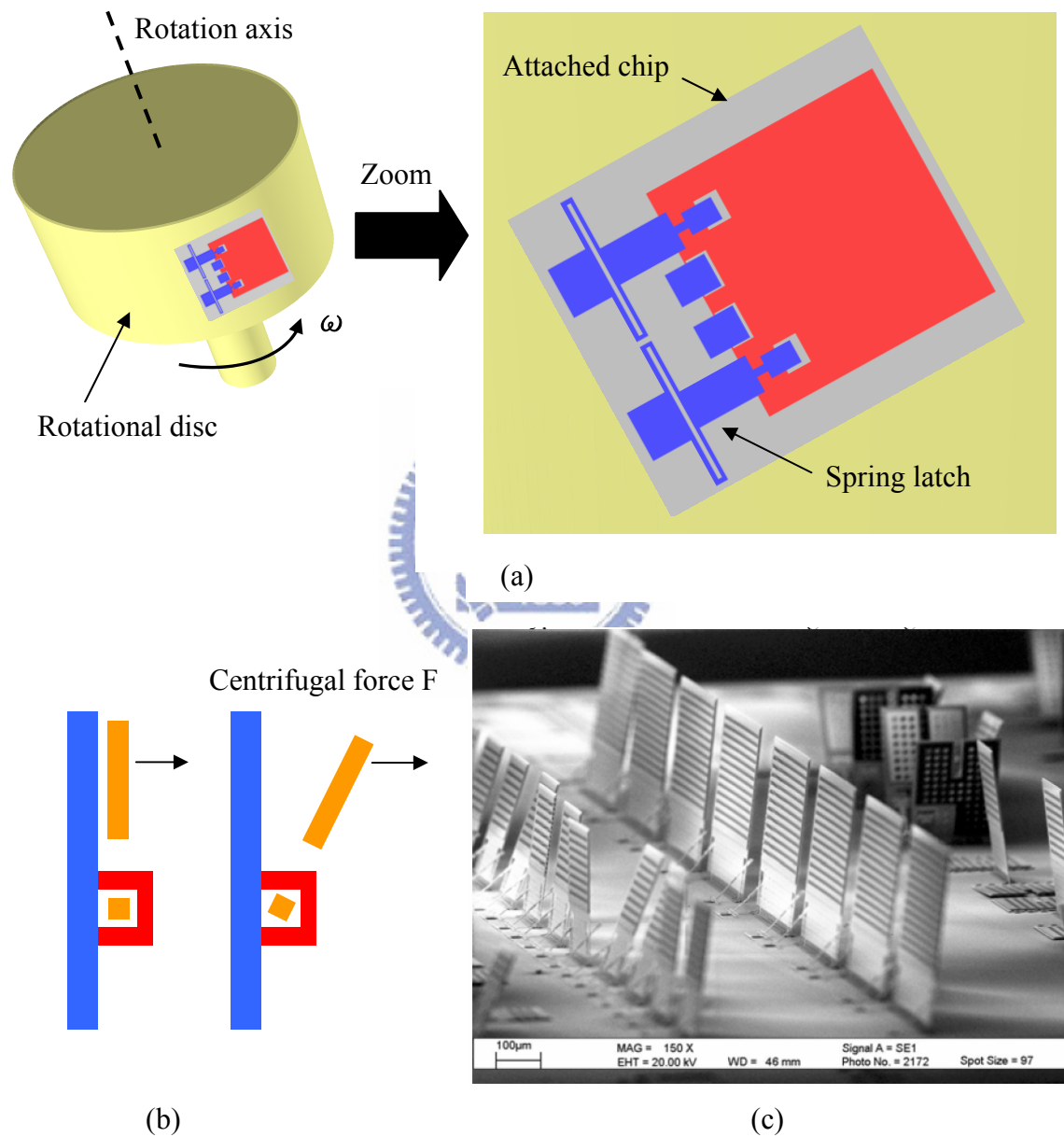
Figure 1-9 Microassembly by electrostatic force [15].

#### 1-2-5 Centrifugal force assembly

K. W. C. Lai et al. [16] proposed a microassembly technique by using centrifugal force to raise the hinged surface micromachining structures. The basic concept of this technique is illustrated in Figure 1-10. The chip is attached to a rotational disc and is placed perpendicular to the rotation axis, as shown in Figure 1-10 (a). The hinged microstructures will be pulled away from the substrate due to the centrifugal force once rotation is started, as shown in Figure 1-10 (b). The latch structures are used to



engage and lock these structures into position. Figure 1-10 (c) shows the batch microassembly by using centrifugal force.



### 1-2-6 Surface tension-powered self-assembly

Because of the force scaling law, as systems are miniaturized, surface forces become increasingly dominant compared to volume forces. This feature makes the surface tension appropriated as the driving force in the microstructure size domain. The basic process concept of surface tension self-assembly and SEM of assembled structures are illustrated in Figure 1-11 [17]. The SOI structure is patterned by RIE, and a meltable material, such as resist, is coated and patterned. To improve the adhesion of the resist pads during the HF release process, the premelt step is necessary. After the mechanical parts are freed, the molten resist creates the surface tension torque which causes the flap to rotate out of plane. The final rotation angle is determined by the geometry features of the meltable pad [18].

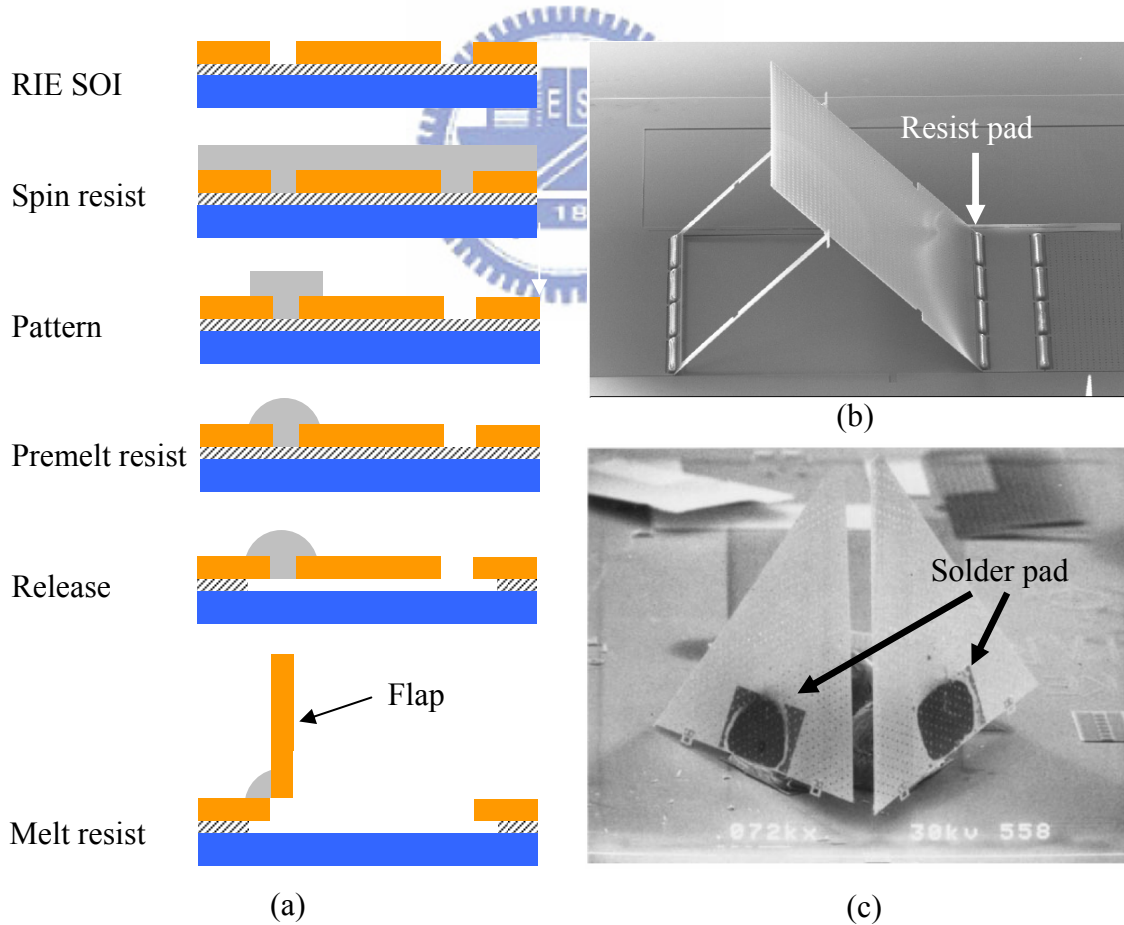


Figure 1-11 (a) Process flow of surface tension assembly, (b) 45° self-assembled mirror based on photoresist hinges, (c) pyramid enclosure assembled by the surface tension forces of molten solder [17].

### **1-2-7 Microassembly of 3-D microstructures using microgrippers**

N. Dechev et al. [19] proposed a novel microassembly system, which made use of a compliant microgripper to construct out-of-plane 3-D microstructures. This approach is based on three entities: a surface-micromachined microgripper, a robotic workstation, and surface micromachined micro-parts. The surface-micromachined microgripper is initially attached to the substrate by tethers. The tethers are designed to hold the microgripper onto the substrate during shipping but are weak enough to break away during the solder bonding process. The goal of the solder bonding process is to tightly attach the microgripper to the contact head of the robotic arm. The contact head, which has a metal tip, is used as the interface between the robotic arm and the microgrippers. The tin-lead solder is applied to the heated metal tip of the contact head and melts. Simultaneously, the metal tip is aligned to the solder pad of the microgripper and then pressed down on it. When the solder solidifies during the cooling phase, the tethers break away and therefore free the microgripper from the substrate. The attached microgripper is translated by the robotic station to align with the surface micromachined micro-parts. The passive, compliant microgripper is used to grasp the micro-parts and reorients it from the original position of fabrication to the place of assembly. The microgripper is released after inserting the micro-parts into slots of the substrate, and the whole assembly is complete. Figure 1-12 shows the five-axis robotic manipulator and the close-up view of a microgripper which is solder bonded to the metal tip. Figure 1-13 shows the whole assembly process and the image of the assembled microstructures.

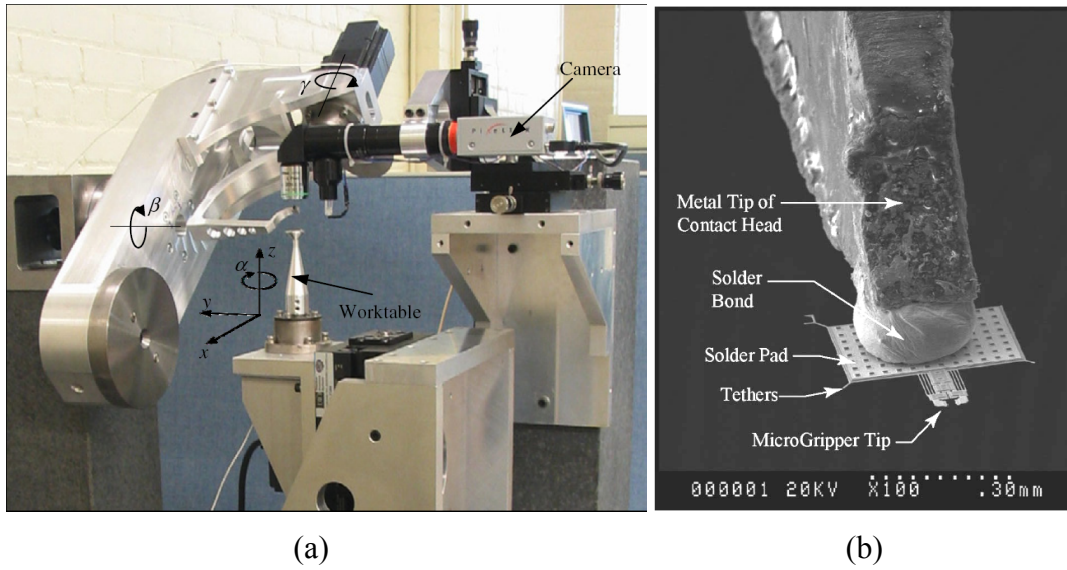


Figure 1-12 (a) Five axis robotic workstation, (b) solder bonded microgripper [19].

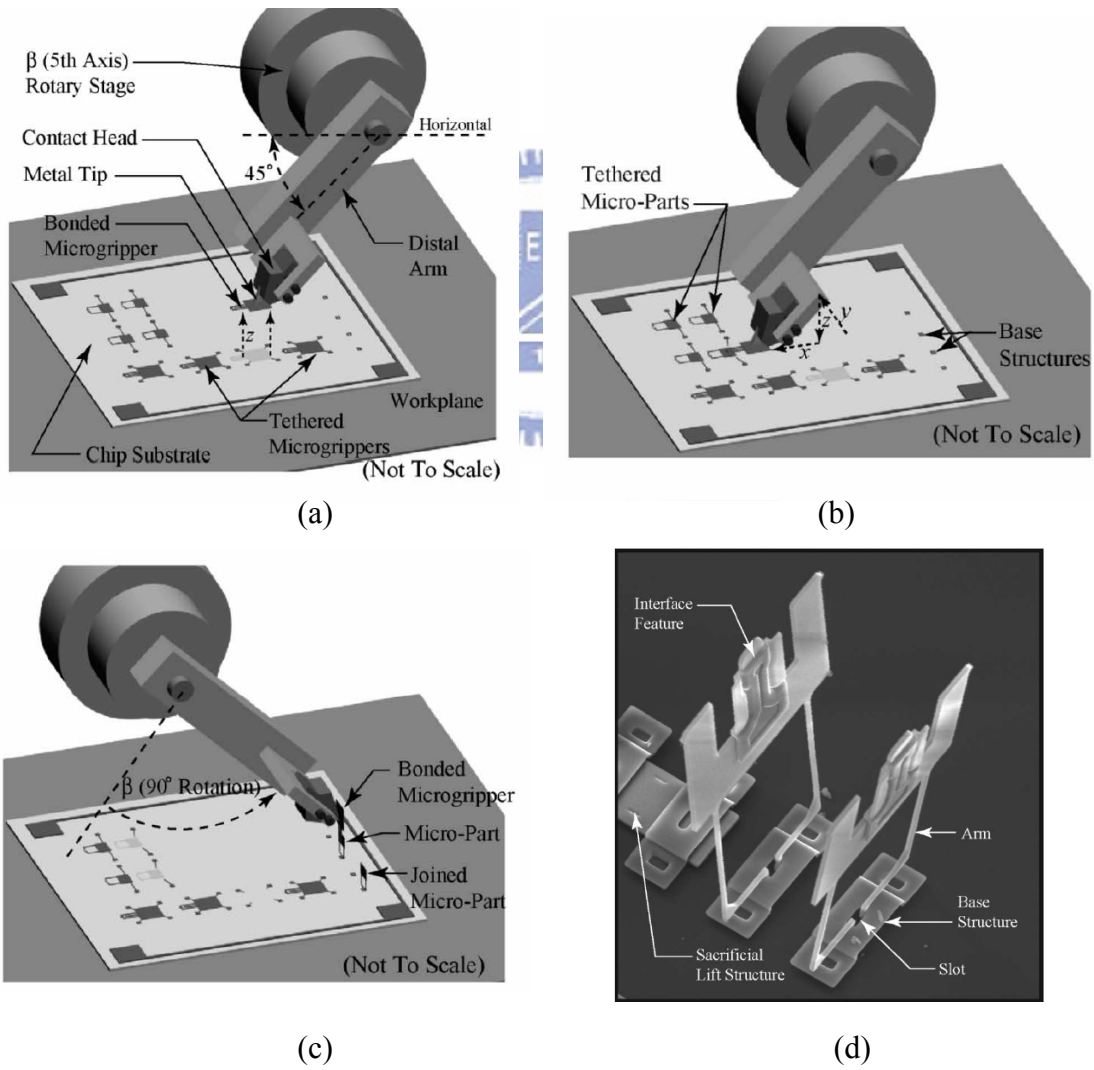


Figure 1-13 Assembly process, (a) bonded microgripper grasps micro-part, (b) move the micro-part to the place of assembly, (c) insert the micro-part into the slot, (d) out-of-plane 3-D microassembly [19].

### 1-2-8 Microassembly of hingeless 90° microstructures

S. H. Tsang et al. [20] used automated probing systems and hingeless microstructures to reduce the cost and complexity of out-of-plane microassembly. The concept is based on compliant hinges which can provide out-of-plane motion by redirecting lateral displacement into rotation. As shown in Figure 1-14, the device is attached to the substrate by serpentine springs which are relatively stiff in the in-plane direction and compliant in the out-of-plane direction and rotation. When a force is applied to the actuation point, the resulting moment twists the spring and causes out-of-plane rotation. This device is fabricated by a single structural layer instead of the multiple structural layers used in staple hinges. The assembly sequence is illustrated in Figure 1-15. The actuation force ( $F_A$ ) and the restoring force of the springs ( $F_S$ ) can create an out-of-plane torque (Figure 1-15 (b)). When the probe slides forward, the rotational torque continues to increase and the spring is stretched (Figure 1-15 (c)). Once the device reaches a certain angle, the spring will begin to pull the device (Figure 1-15 (e)) until it becomes upright (Figure 1-15 (f)). Figure 1-16 (a) shows the optical micrograph of this assembly process. Figure 1-16 (b) demonstrates the SEM image of the assembled SU-8 devices.

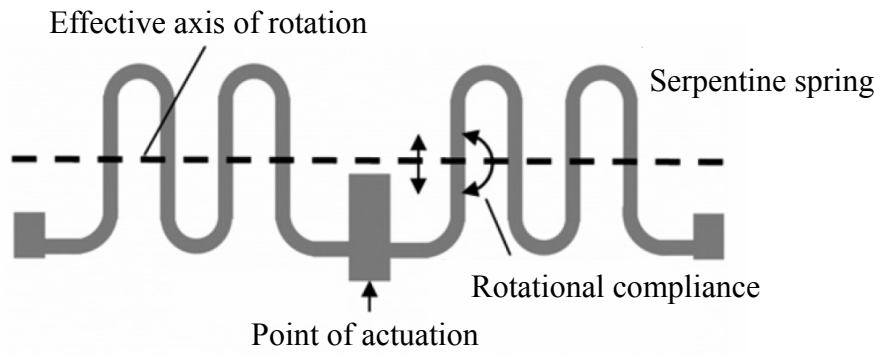


Figure 1-14 Hingeless device concept [20].

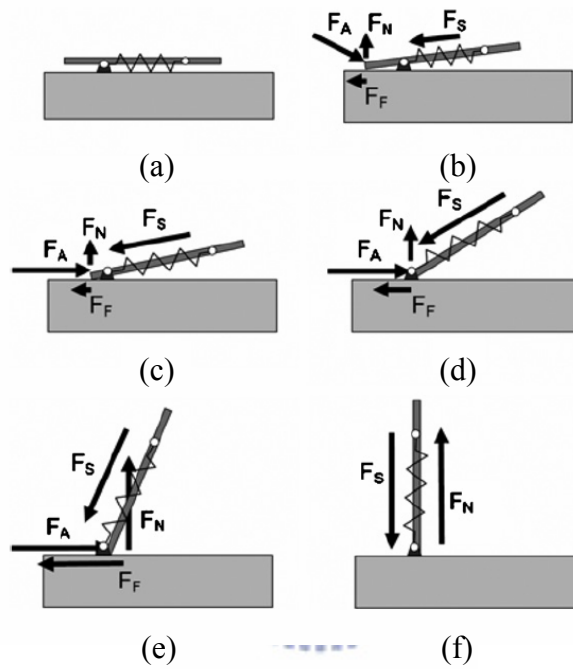


Figure 1-15 Schematic assembly sequence [20].

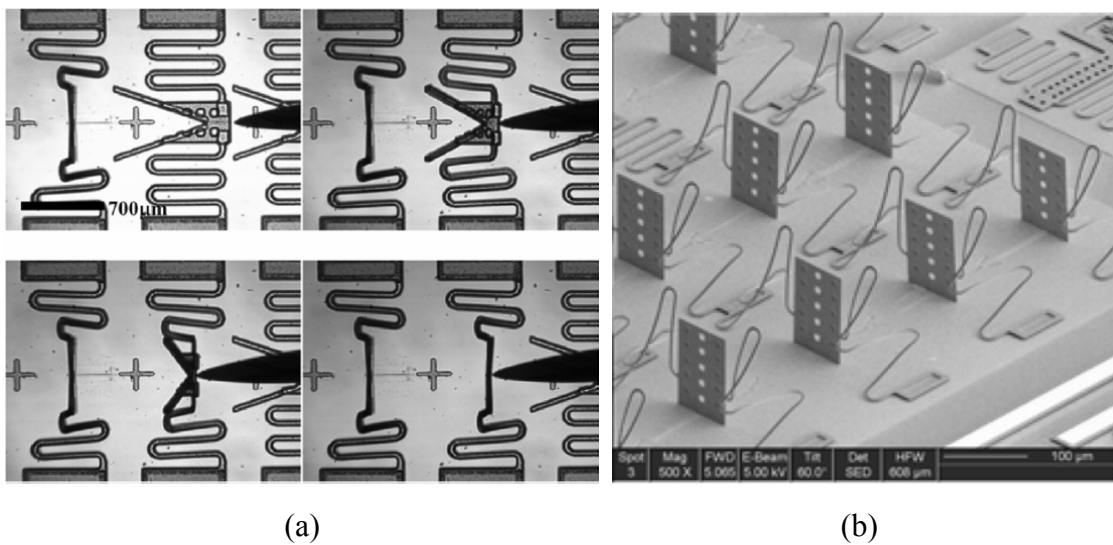


Figure 1-16 (a) Assembly of the SU-8 structures, (b) SEM image of 90° out-of-plane SU-8 structures [20].



### 1-3 Objectives and thesis organization

Table 1-1 is a brief comparison of the above-mentioned assembly methods. Assembly by built-in actuators, such as SDA, usually occupies large chip area, and the design of optimal actuator is difficult. Assembly by external forces, such as magnetic and electrostatic forces, requires materials not compatible IC process or needs a large electrical field. Assembly by surface-tension forces is subject to precise control the fabrication conditions. Assembly using micromanipulators is a low cost and easily accessible solution. However, its drawbacks are mainly time consuming and non-batch fabrication. More effective and batch assembly technique are necessary. The assembly technique with one push operation is proposed to reduce the assembly complexity. A new hinge design for improving position accuracy of the assembled device is proposed. Therefore, the objectives of this thesis include:

1. Simplify the lifting and manipulating operations in manual assembly to a single push operation.
2. Enhance the microstructure positioning accuracy by a novel hinge design.

The basic principles and simulations of the proposed microstructures and assembly method are presented in Chapter 2. The fabrication processes and process issues are discussed in Chapter 3. The experiment and measurement results are presented in Chapter 4. Conclusion and future work are discussed in Chapter 5.

Table 1-1 Comparison of assembly methods

Assembly method	Advantage	Disadvantage
SDA	Precise assembly	Occupying large chip area, complexity
Magnetic force	Batch	Incompatibility with IC process
Electrostatic force	Batch	Requiring large electrical field.
Centrifugal force	Batch	Low yield
Surface-tension force	Batch, simple	Difficult to fabrication control
Microgrippers assembly	Complex structure	Expensive equipment is needed
Manual assembly	Low cost	Complexity, time consuming





# Chapter 2

## Principle and Design

A novel 3-D MEMS structure design concept is proposed to implement vertically standing micromirrors using SOI and SU-8. The operation principle and design are discussed in this chapter. The finite-element simulations of the structures using ANSYS are also presented. Finally, the micromachined mirrors without etch holes are investigated to improve the optical quality.

### 2-1 Introduction

Structures with large vertical dimensions can be implanted by integrating the hinge elements and hinged microstructures. However, there are some problems with conventional hinge design. As shown in Figure 2-1, the microfabricated hinge pin has a rectangular rather than round cross section and the mask alignment restrictions result in hinge play [21]. The resulting spacing allows the hinge pin to move horizontally and vertically. Although the play in general is not detrimental to the functionality of the hinge, the angle accuracy of the assembled structures will be greatly affected due to this play. For some applications, the angle positioning error result form this play is acceptable. But there are applications that require much greater accuracy, especially in optics. Therefore, methods of improving the accuracy of the assembled components are necessary.

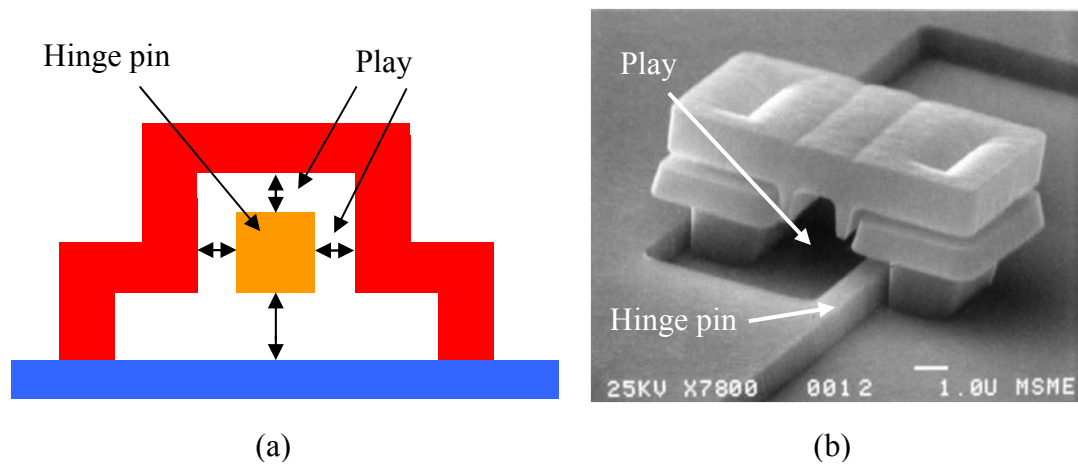


Figure 2-1 (a) Cross section view of the conventional hinge, (b) SEM image exhibits a large amount of play in the hinge [21].

In addition to the hinge design, the latch mechanism is also very important for 3-D structure assembly. In general, mechanical locks are used to control the rotation of the hinged plate. Figure 2-2 illustrates a basic mechanical lock design that is commonly used in micro-optics [8]. This mechanical locking mechanism consists of two hinged side plates with V-shaped openings, followed by a long, narrow groove. The assembly process of this design is demonstrated in Figure 2-3. After the hinged plate is rotated out of plane by a microprobe and becomes upright to the substrate, the side plates are folded onto the plate. Therefore, the upright plate is firmly locked into the groove. The disadvantage of this structure is that it involves too many operations to assemble the structure by using microprobes. There are totally three operations. First of all, the microprobe is used to lift the hinged structure to the upright position. Secondly, one of the two side plates is folded and engaged one side of the plate by a microprobe. Finally, a microprobe is used again to fold the other one onto the plate. This is a time consuming process and the probability of damaging the assembled structure is high. Another problem of this structure is that the device is held in place by friction forces between the hinged plate and the side plates. This leads to an uncertain position when the system undergoes a shock. The side plates may be

displaced away from the hinged plate, allowing the hinged plate to collapse from its vertical position and thereby destroy the 3-D structure.

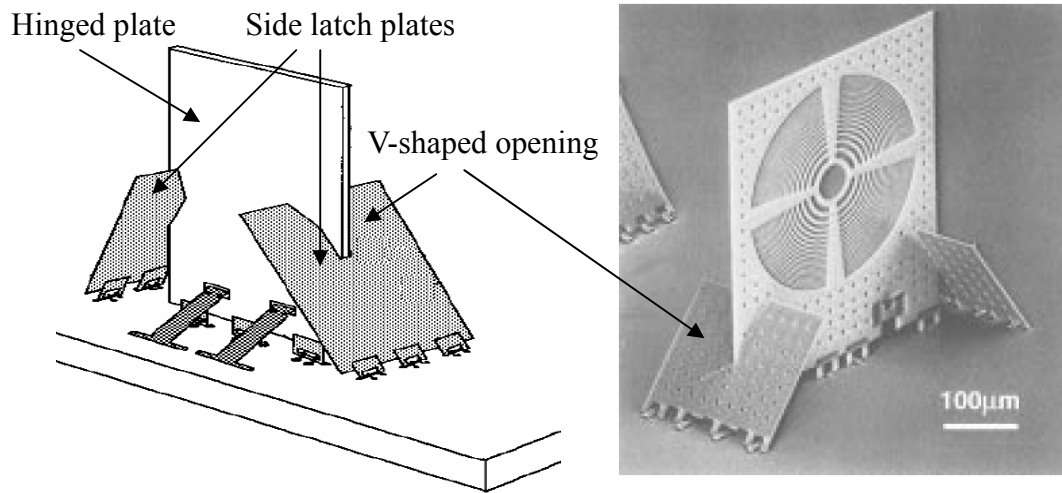


Figure 2-2 Side latch plates with V-shaped lock slots to fix the hinged plate [8].

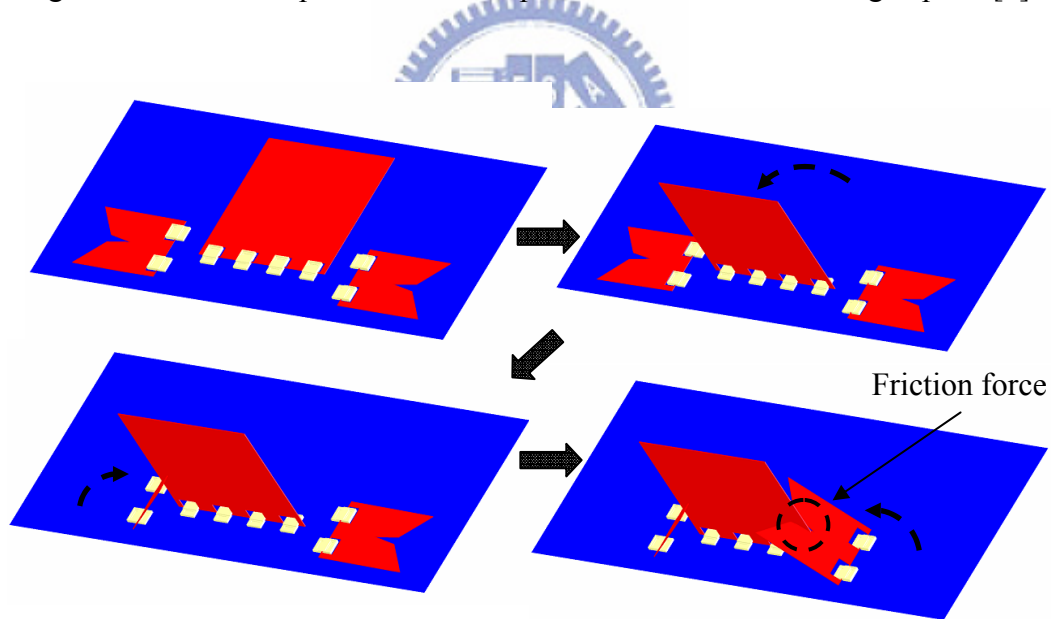
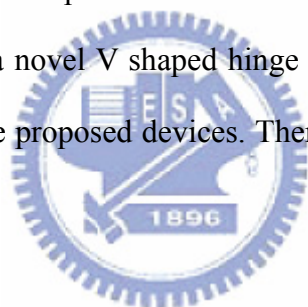


Figure 2-3 Multiple assembly processes are applied to complete the 3-D structure. The final assembled structure is fixed in position by friction force.

In traditional microprobe-assembled devices discussed above, the probes must be manipulated in different directions with precise and complex motion control. Sometimes they must be inserted into the gaps formed by the release of sacrificial layers or aligned with the thin flat structures on the surface before the assembly process. To eliminate the need for precise probe control, a novel assembly process and micro structures are proposed. In this approach, all probe motion is reduced to a simple one-push operation. Therefore, the probes only need to be aligned with a relatively large push pad with large alignment tolerance in the lateral directions. Since the probes move vertically in the push operation, the vertical alignment is not critical. Furthermore, the structures can be over pushed in the assembly process and thus the motion control is much eased compared to traditional techniques. In addition to the simplified assembly process, a novel V shaped hinge is used to eliminate the play in traditional hinge designs in the proposed devices. Therefore, the positioning accuracy can be improved.



## **2-2 Integration of SOI wafer and SU-8 structural layer**

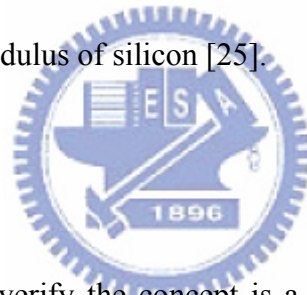
The technology of combining SOI wafer with SU-8 negative photoresist was proposed to fabricate the microoptical devices [22]. The optical frame structures are made of the SCS layer of the SOI wafer. The reasons to use SOI wafers instead of conventional silicon wafers are:

1. They do not have the stress problems in polysilicon micromaching,
2. They have better surface smoothness,
3. A broad range of made-to-order SCS layer thicknesses are available.

The SU-8 photoresist is used as another structural layer. Traditional surface micromachining usually uses thin polysilicon as the structural material. The reasons

for replacing it by SU-8 are:

1. Polysilicon deposition is a high temperature process. If circuits are integrated into the same substrate, the high temperature condition will affect the performance. The SU-8 process is a spin coating, low temperature process, and thereby suitable for circuit integration.
2. SU-8 can be used to create structures as thick as 2 mm and with aspect ratios up to 25 with standard UV-lithography [23].
3. SU8 has good mechanical property and chemical resistance. These features are highly favorable for mechanical microstructures. Furthermore, SU-8 is a soft material compared to other commonly used materials in MEMS. The Young's modulus of SU-8 is in the range from 2 to 7.5 GPa [24], which is about 40 times lower than the Young's modulus of silicon [25].



## **2-3 Device design**

The proposed device to verify the concept is a vertically standing mirror. The device must be assembled more easily, positioned more accurately, maintained more robustly, and have excellent optical properties.

### **2-3-1 Assembly process**

The layout view and the 3-D solid model of the proposed device are shown in Figure 2-4. It consists of a mirror plate, V-shaped hinges and flexible side support latches. The push pad is the place where the microprobe pushes. The backside cavity is used as a room for the assembly procedure. The mirror plate is made of single crystal silicon in the device layer of the SOI wafer. The V-shaped hinge and side support latch are made of SU-8 negative photoresist.

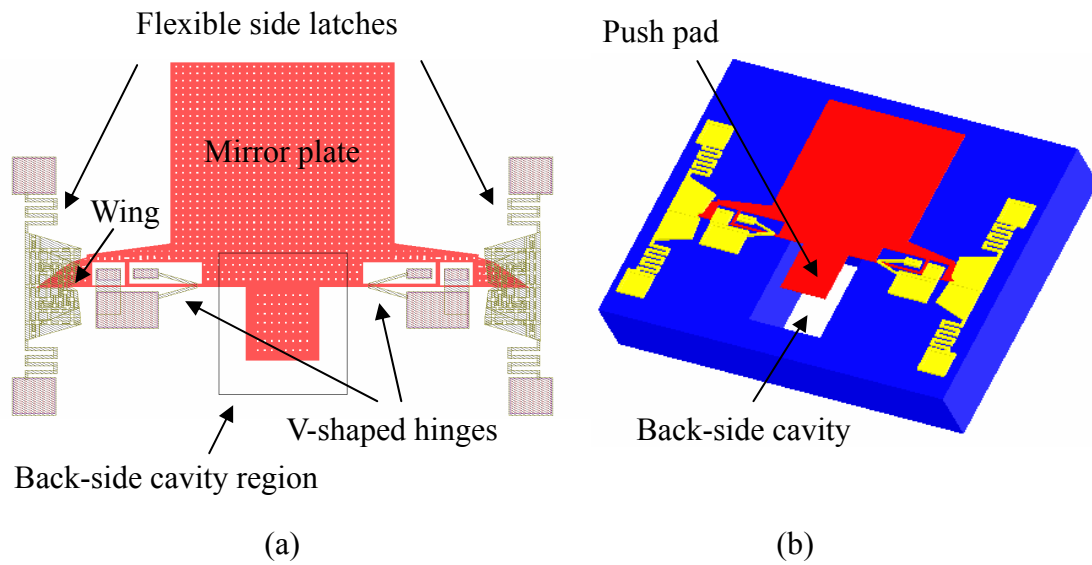


Figure 2-4 (a) Layout of the proposed micromirror device, (b) 3-D solid model of the micromirror device.

The assembly procedure of the device is shown in Figure 2-5. A microprobe station is utilized as the assembly equipment. The microprobe is first moved to align with the push pad (Figure 2-5 (a)). When the push pad is pushed down by the microprobe, the mirror plate rotates about the pin axis. Once the mirror plate moves out of the plane, the wing of the mirror plate contacts the bottom of the side latch. This upward force will simultaneously drive the flexible side latches to rotate out of the plane (Figure 2-5 (b)). As the mirror plate is rotated to the upright position, it will slide into the V-shaped slot of the flexible side latches (Figure 2-5 (c)). The V-shaped lock slot and the downward restoring force of the spring will firmly lock the mirror plate in place. At this time, the microprobe is moved away, and the whole assembly process is complete (Figure 2-5 (d)). The complete 3-D microstructure is assembled in just one push operation.

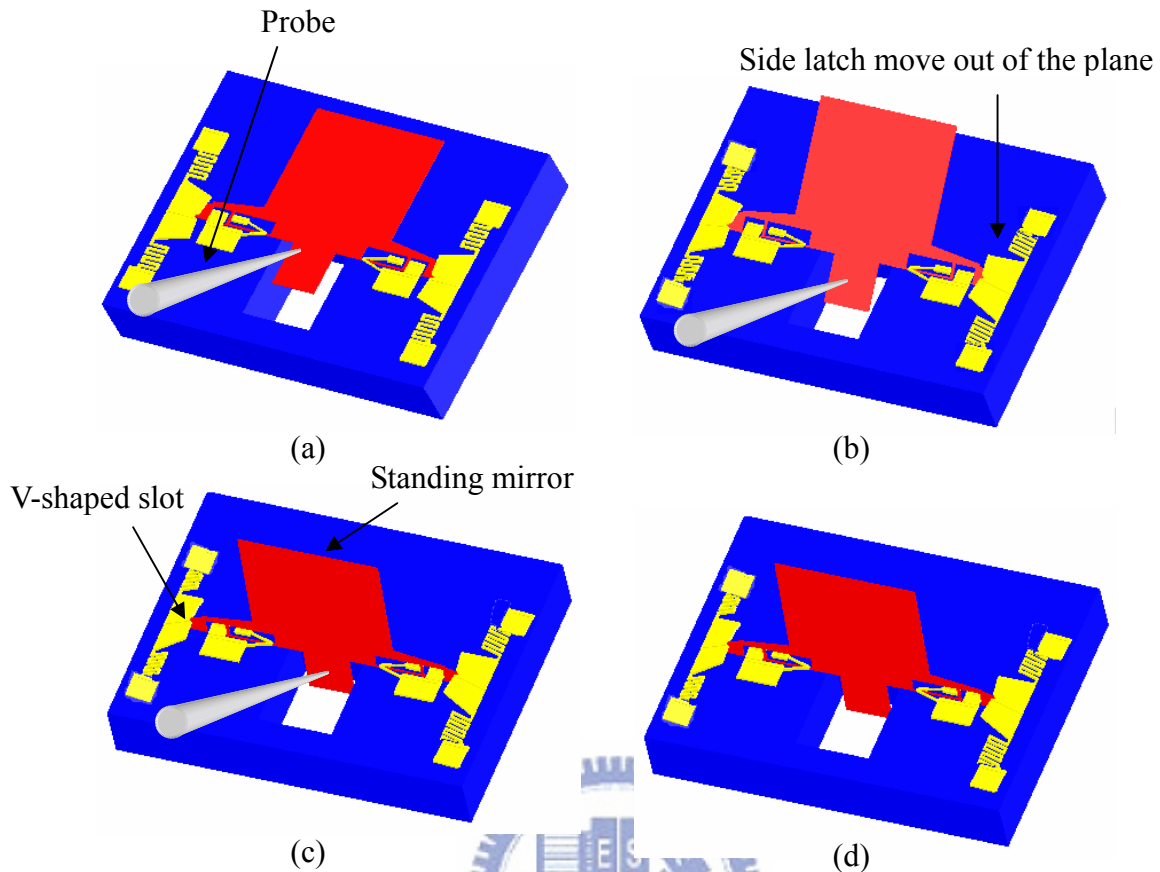


Figure 2-5 Assembly process with only one push operation.

### 2-3-2 Locking mechanism

In addition to the simplified one-push assembly process, the proposed device also employs a novel V-shaped hinge for better angle positioning compared to traditional micromachined hinges. Besides, flexible side latch is used to reduce the assembly process.

As discussed above, the hinge play of the conventional microhinge design results in angular deviation of the assembled structure. The novel V-shaped hinge element is proposed to address this issue. The layout view and 3-D solid model of this element are shown in Figure 2-6. The width of the hinge pin below the V-shaped hinge is greater than the total vertical spacing including the BOX (buried oxide) layer, the SCS

(single crystal silicon) layer, and the sacrificial layer in the SOI/SU-8 process. The assembly process of the V-shaped hinge is demonstrated in Figure 2-7. When the mirror plate is in the horizontal position (Figure 2-7 (a)), the wide hinge pin and the V-shaped hinge are not in contact. The mirror plate can rotate freely without bending the V-shaped hinge until the hinge pin touches the bottom of the V-shaped hinge (Figure 2-7 (b)). When the mirror plate is rotated further, the hinge pin causes the V-shaped hinge to bend. The hinge pin will be locked between the two sides of the V-shaped hinge when the mirror plate is in the upright position (Figure 2-7 (c)).

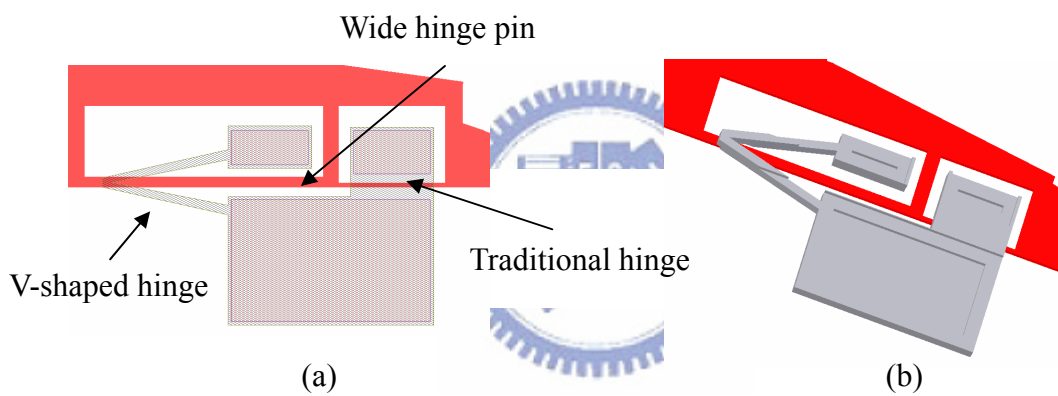


Figure 2-6 (a) Layout of the V-shaped hinge, (b) 3-D solid model.

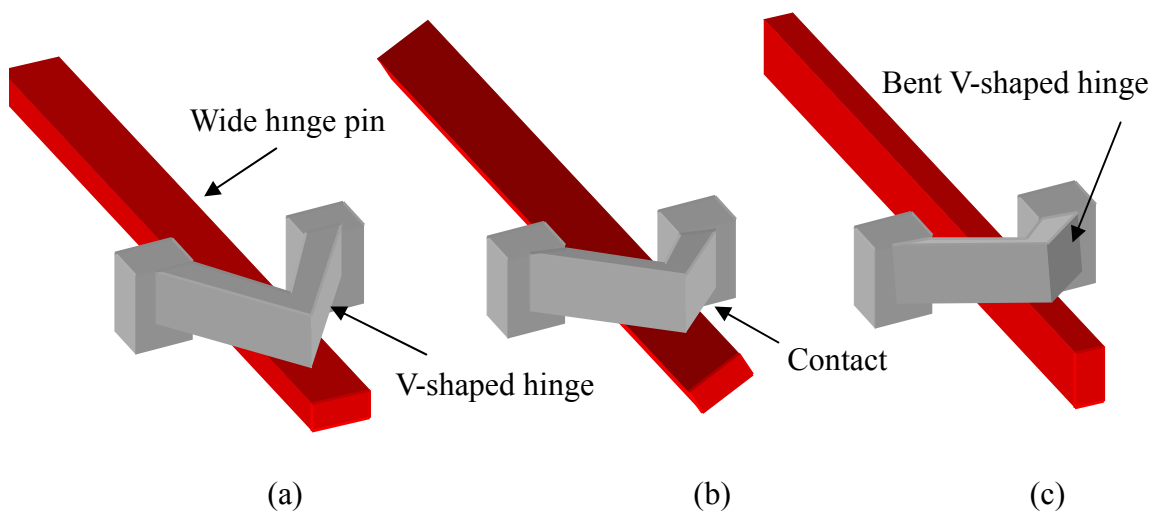


Figure 2-7 3-D view of the V-shaped hinge during assembly process.



Figure 2-8 shows the positioning principle of the V-shaped hinge. As shown in Figure 2-8 (b), the vertical play can be eliminated due to the downward restoring force of the flexible V-shaped hinge. This downward force locks the hinge pin in place. Furthermore, the hinge pin will be locked between the two sides of the V-shaped hinge when the mirror is in the upright position, as shown in Figure 2-8 (c). Hence the x-direction play and y-direction play can also be eliminated.

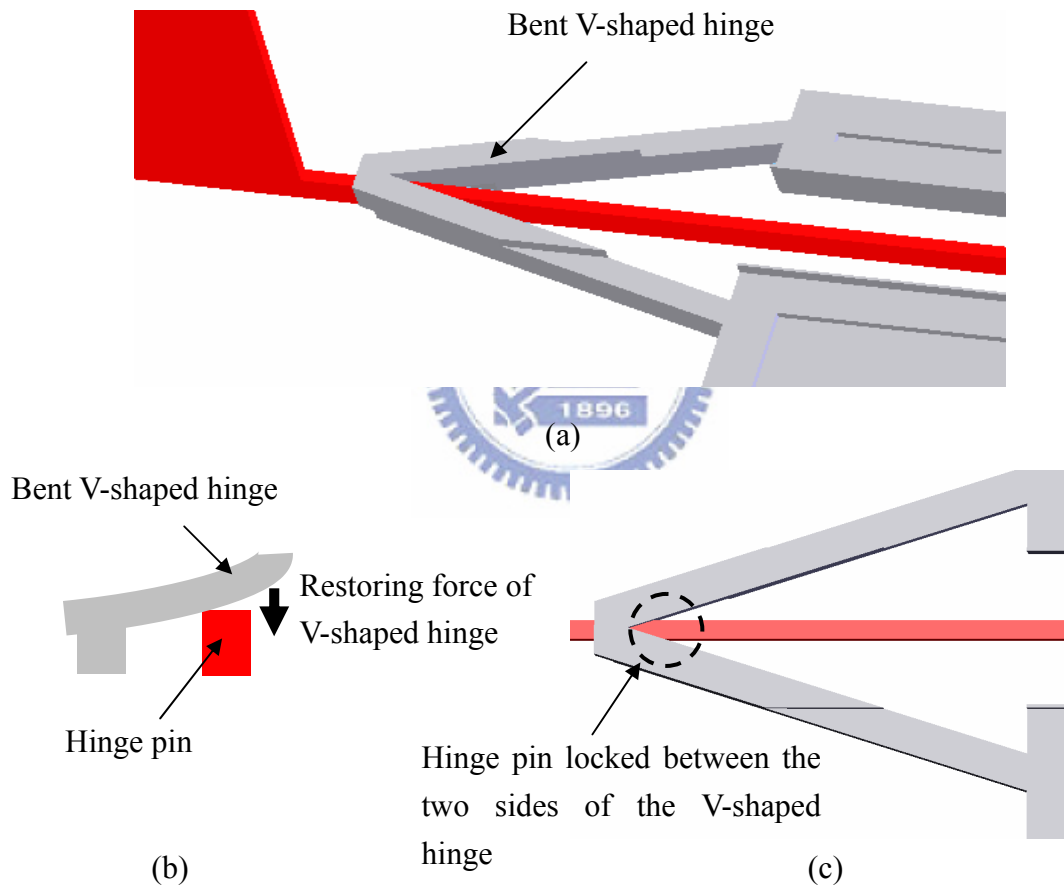


Figure 2-8 (a) 3-D solid model of the V-shaped hinge after assembly, (b) cross-section view of the restricted z-direction movement, (c) top view of the positioning mechanism.

Flexible side latch is another feature in the proposed device. The conventional side latch is susceptible to shock. In order to address this problem, the side latch is designed to exert a force on the hinged plate by a flexure mechanism. The conventional side plate is attached to the substrate by staple hinges. It can freely rotate about the pin axis. The locking mechanism is by the friction force. If the side plate is attached to the substrate by spring elements, it will be able to create a force due to the restoring force of the spring elements. This concept is illustrated in Figure 2-9.

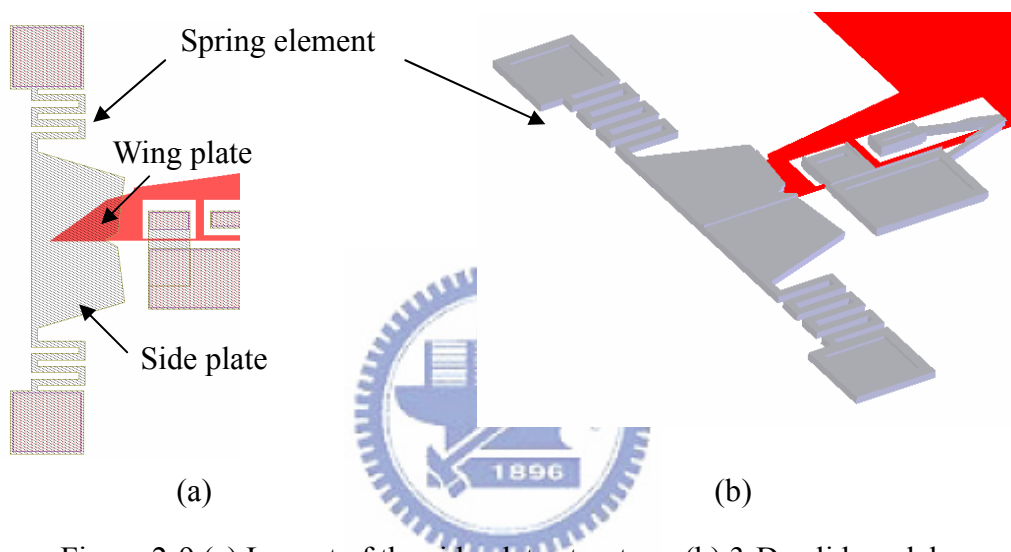


Figure 2-9 (a) Layout of the side plate structure, (b) 3-D solid model.

The operation of this side latch design is shown in Figure 2-10. Before the mirror plate is lifted, the wing plate and the side latch are not in contact (Figure 2-10 (a)). As the mirror plate is elevated, the wing plate touches the bottom of the side latch and causes it to rotate out of plane about the spring axis (Figure 2-10 (b)). The wing plate continuously drives the side latch to rotate until the mirror plate slides into the V-shaped opening. Once the mirror plate is rotated further to the upright position, it will slide into the lock slot in the side latch and lock firmly in place (Figure 2-10 (c)). The side plates now provide force upon the mirror plate. This will hold the mirror plate in position more robustly and enhance the shock resistance.

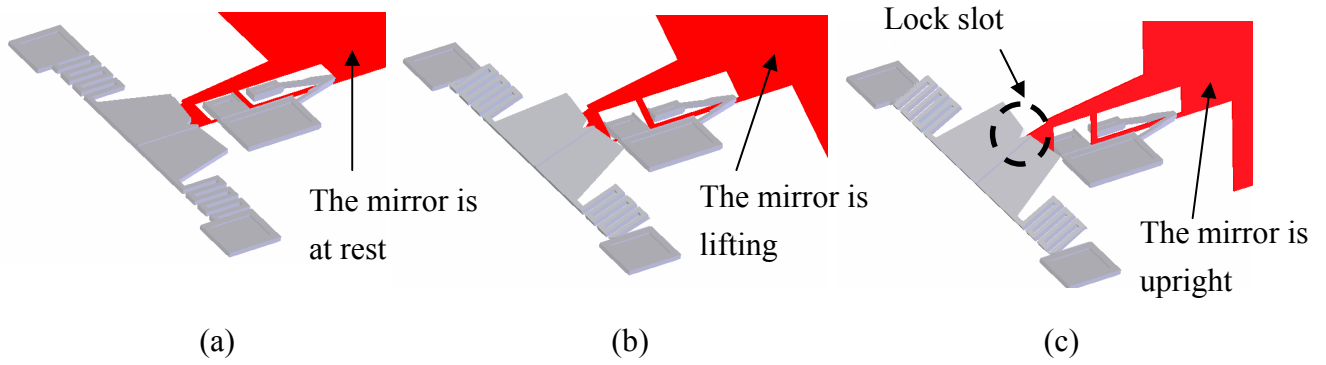


Figure 2-10 Flexible side latch assembly process

## 2-4 V-shaped hinge

J. E. Sader [26] proposed an analytical model for determining the spring constant of the V-shaped spring structure. Figure 2-11 illustrates the geometry of the V-shaped spring whose spring constant is:

$$k = \frac{Et^3d}{2L^3} \cos \theta \left\{ 1 + \frac{4d^3}{b^3} (3 \cos \theta - 2) \right\}^{-1} \quad (2-1)$$

$$\frac{k_{\Delta L}}{k} = \left( \frac{L}{L - \Delta L} \right)^3$$

where  $k$  and  $k_{\Delta L}$  are the spring constants when the load is applied to the end of tip and when it is applied a finite distance  $\Delta L$  from the end, respectively,  $E$  is Young's modulus of the spring material,  $t$  is the thickness of the structure, and  $d$ ,  $b$ ,  $L$ ,  $\theta$  are the geometric parameters as shown in Figure 2-11.

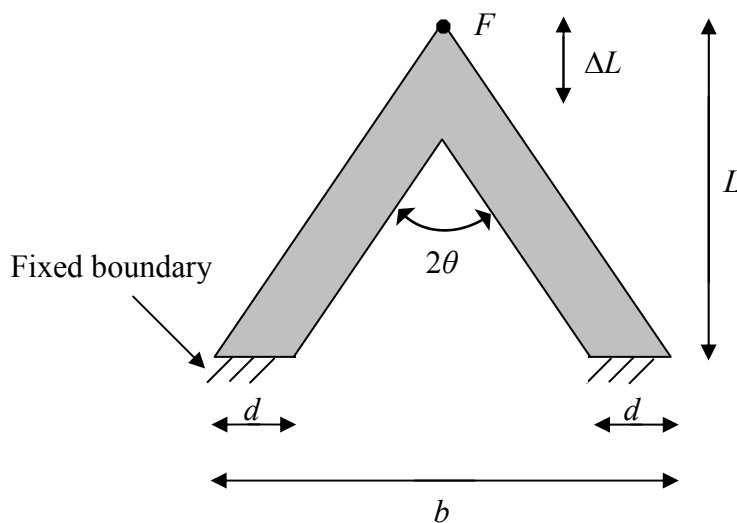


Figure 2-11 Top view of a V-shaped cantilever showing dimensions and loading  $F$ .

Figure 2-12 shows the bending of the V-shaped spring before and after assembly. The SCS layer of the SOI wafer is 5  $\mu\text{m}$  thick. The two sacrificial layers are 2- $\mu\text{m}$ -thick BOX and 3- $\mu\text{m}$ -thick PECVD oxide. The SU-8 spring layer is 13  $\mu\text{m}$  thick. The hinge pin is 11  $\mu\text{m}$  wide. The structure of the V-shaped hinge before release is shown in Figure 2-12 (a). The V-shaped hinge will bend upward by 1  $\mu\text{m}$  after assembly, as shown in Figure 2-12 (b). Hence, the V-shaped hinge must be designed to bend by 1  $\mu\text{m}$  without breaking.

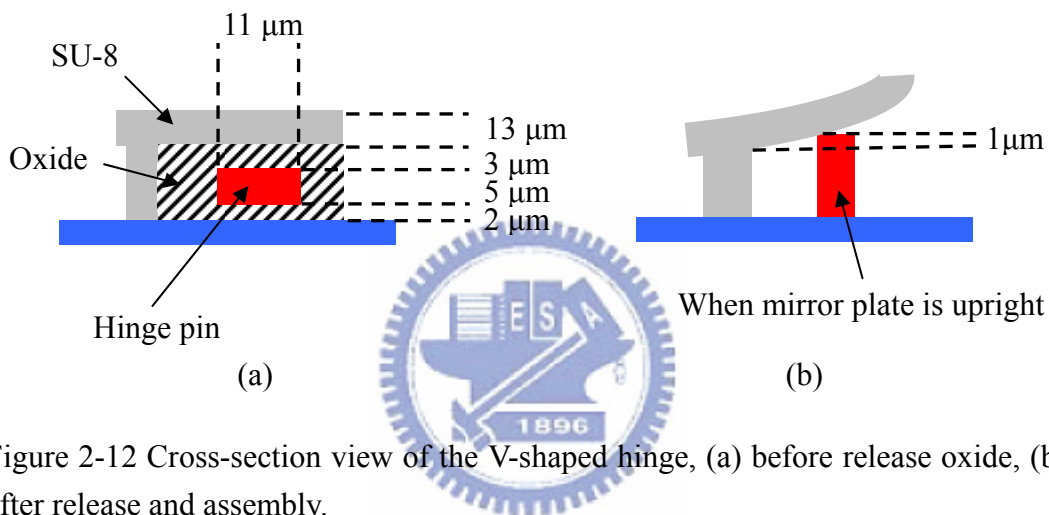


Figure 2-12 Cross-section view of the V-shaped hinge, (a) before release oxide, (b) after release and assembly.

According to Equation 2-1, the spring constant can be determined from the required bending of 1  $\mu\text{m}$  at the tip. In this thesis, the V-shaped hinge is designed in the space shown in Figure 2-13, determined by the dimension of the mirror plate. Since this is a preliminary feasibility study of the V-shaped hinge mechanism, further optimization of the spring design is in progress. The geometric parameters are listed in the Table 2-1. The spring constant calculated by substituting these values into Equation 2-1 is 23.6 F/m. By Hooke's law, the downward restoring force due to the 1  $\mu\text{m}$  bending is then 23.6  $\mu\text{N}$ . ANSYS is used to simulate the stress distribution in the structure. The requirement is to have the stress well below the yield strength of the SU-8. Figure 2-14 shows the ANSYS simulation results. The x-component stress,

y-component stress, z-component stress, and Von stress are 6.8 MPa, 1.9 MPa, 1.92 MPa and 6.31 MPa, respectively. All stresses are below the yield strength of SU-8, which is about 50 MPa. The simulated value of the spring constant is 22.55 F/m and the simulated force to bend the tip by 1  $\mu\text{m}$  is 22.55  $\mu\text{N}$ .

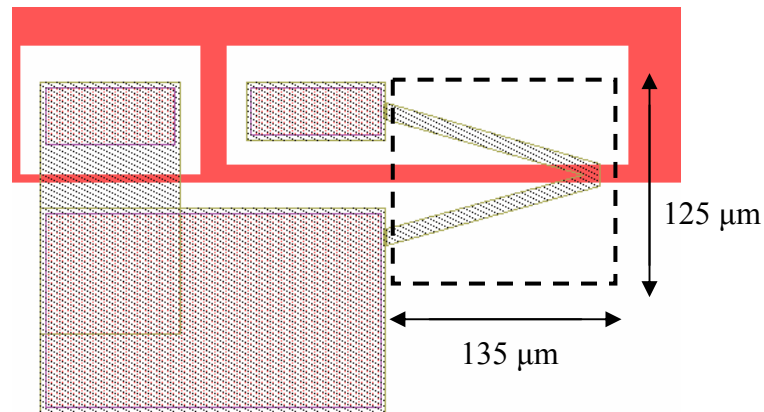


Figure 2-13 Design space for the V-shaped element.

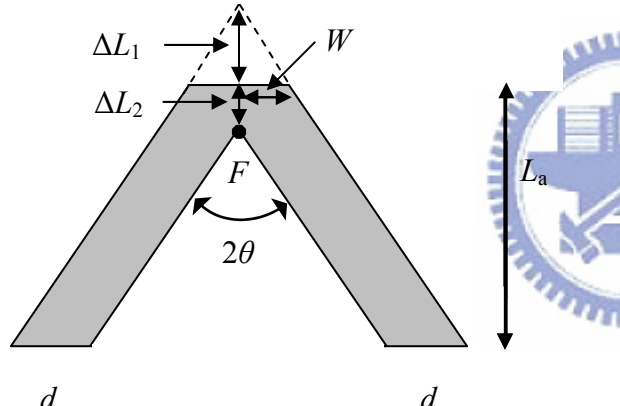
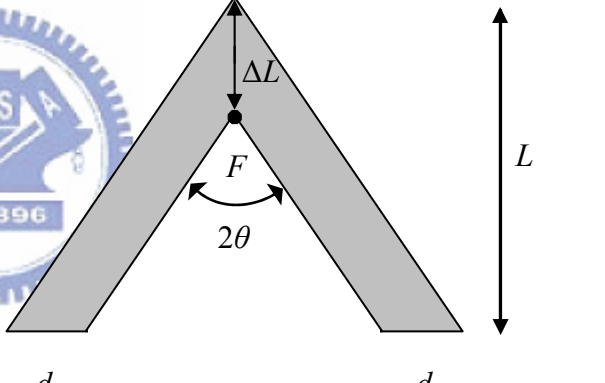
Table 2-1 SU-8 material properties and spring geometric parameters

Parameter	Dimension	Unit
Young's modulus $E$	4.02	GPa
Poisson's ratio	0.22	
Yield strength	50-70	MPa

Geometry of V-shaped hinge	Dimension	Unit
Thickness $t$	13	$\mu\text{m}$
Skewed rectangular width $d$	10	$\mu\text{m}$
V-shaped spring width $b$	88	$\mu\text{m}$
V-shaped spring length $L$	130	$\mu\text{m}$
Skewed angle $\theta$	15.8	degree

The comparison of the analytical and simulated spring constants is listed in Table 2-2. The relative error is 4.5% . The difference of these two structures is that the proposed V-shaped hinge is not exactly the V-shaped structure in [26], as shown in Table 2-2. There is also a 2% difference between the analytical equation and original FEM simulation [26]. Therefore, Equation 2-1 can still be used as a guideline for the V-shaped hinge design.

Table 2-2 Comparison of two V-shaped structures

Proposed V-shaped hinge	V-shaped spring [26]
	
$\Delta L_1=24 \mu\text{m}, \Delta L_2=10 \mu\text{m}, L_a=130 \mu\text{m}, W=7\mu\text{m}$ $d=10 \mu\text{m}, b=88 \mu\text{m}, t=13 \mu\text{m}, \theta=15.8^\circ$	$L=154 \mu\text{m}, \Delta L=34 \mu\text{m}$ $d=10 \mu\text{m}, b=88 \mu\text{m}, t=13 \mu\text{m}, \theta=15.8^\circ$
simulated value using ANSYS: → spring constant = 22.55 F/m	analytical value using Equation 2-1: → spring constant = 23.6 F/m

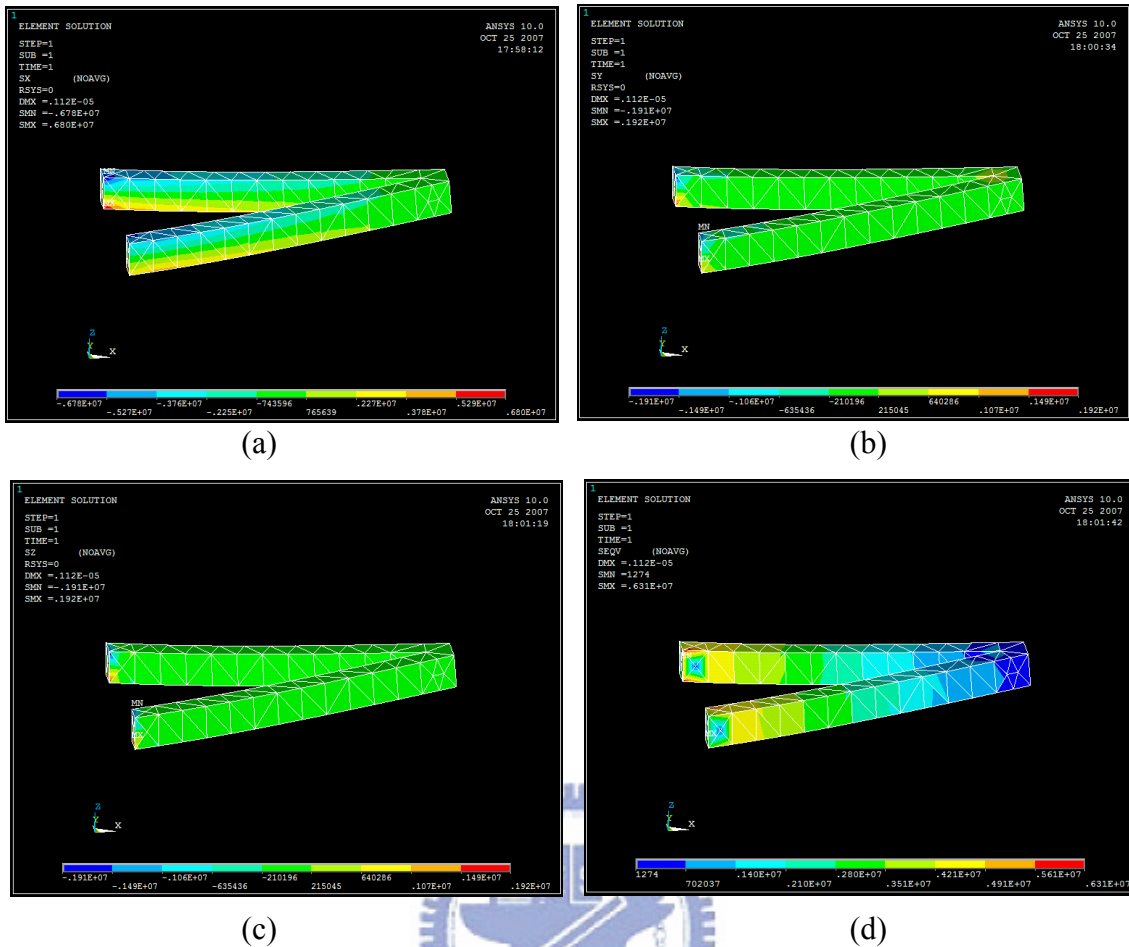


Figure 2-14 Simulations of the V-shaped spring (a) x-component of stress, (b) y-component of stress, (c) z-component of stress, (d) Von stress.

## 2-5 Flexible side latch

The side plates are attached to substrate by spring elements. Four types of springs are used in this thesis, namely the serpentine-type, box-type, meander-type, and skewed box-type, as shown in Figure 2-15. The characteristics of each spring design during in assembly process will be discussed in Chapter 4.

The box type spring is used as an example and shown in Figure 2-16. The left part of the spring can be viewed as two springs with length  $L_2$  and  $L_4$  connected with a rigid truss. If the required twist angle is  $10^\circ$ , we can design beam  $L_4$  and beam  $L_2$  to have a twist angle of  $4^\circ$  and  $6^\circ$ , respectively. The spring design is based on the following basic torsion formula of a beam with square cross section [27],

$$\theta = \frac{\Gamma L}{KG} \quad \text{and} \quad \tau_{\max} = \frac{0.601\Gamma}{a^3}, \quad (2-2)$$

where  $\theta$  is the twist angle,  $\Gamma$  is the twist moment,  $L$  is the beam length,  $G$  is the shear modulus,  $a$  is half of the side of the square cross section and  $K$  is equal to  $2.25a^4$ .

In this thesis, the thickness of SU-8 is 13  $\mu\text{m}$ . Therefore the width of each spring element is also 13  $\mu\text{m}$  and  $a$  is equal to 6.5  $\mu\text{m}$ . The maximum shear stress of SU-8 is about 7 MPa [28]. Thus the maximum shear stress  $\tau_{\max}$  in the structure must be smaller than this value and 6 MPa was adopted in the design. By substituting these values into Equation 2-2,  $K$  and  $\Gamma$  were calculated as  $4 \times 10^{-21} \text{ m}^4$  and  $2.7 \times 10^{-9} \text{ N}\cdot\text{m}$ . From  $L = \frac{\theta KG}{\Gamma}$ ,  $L_4$  and  $L_2$  can be calculated as 167  $\mu\text{m}$  and 272  $\mu\text{m}$ , respectively. The short truss is assumed as a rigid structure, therefore its torsion and bending are neglected. The four types of springs were designed according to the above concepts. The geometry parameters of the four spring types is also listed in Figure 2-15.

Several locking height are also designed. As shown in Figure 2-17, locking height is the vertical distance between the lock point and the substrate. Obviously, a larger locking height means a more robust structure after assembly. The locking heights include 38  $\mu\text{m}$ , 76  $\mu\text{m}$ , 114  $\mu\text{m}$ , 152  $\mu\text{m}$ , which are 5%, 10%, 15%, and 20%, respectively, of the mirror plate height 760  $\mu\text{m}$ .



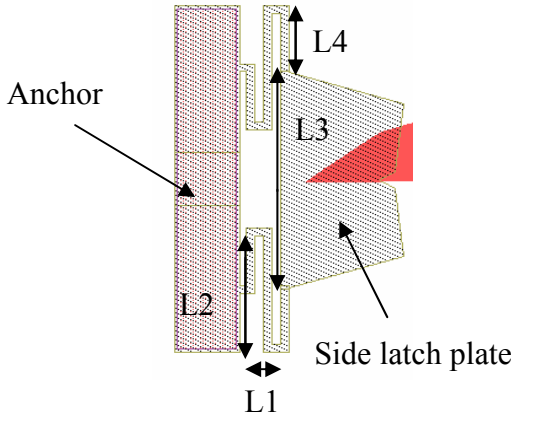
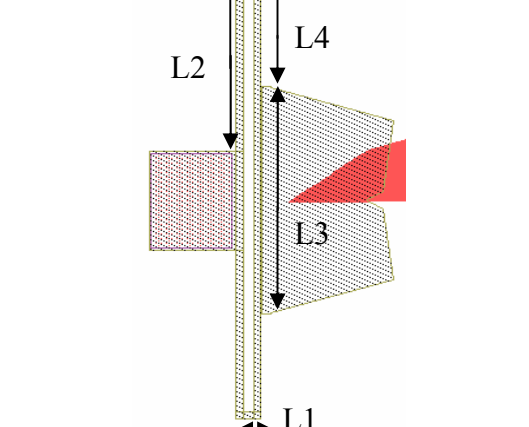
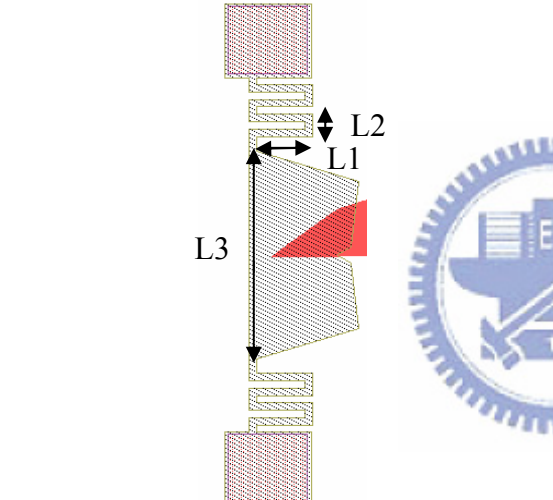
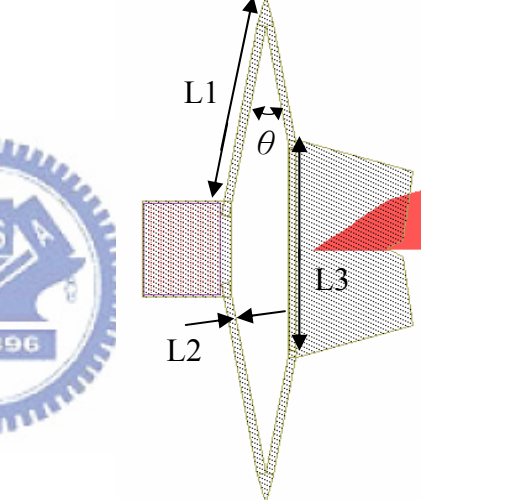
	
<p>L1=39 <math>\mu\text{m}</math>    L2=196 <math>\mu\text{m}</math> L3=340 <math>\mu\text{m}</math>    L4=111 <math>\mu\text{m}</math></p>	<p>L1=39 <math>\mu\text{m}</math>    L2=272 <math>\mu\text{m}</math> L3=340 <math>\mu\text{m}</math>    L4=167 <math>\mu\text{m}</math></p>
	
<p>L1=97 <math>\mu\text{m}</math>    L2=39 <math>\mu\text{m}</math> L3=340 <math>\mu\text{m}</math></p>	<p>L1=380 <math>\mu\text{m}</math>    L2=13 <math>\mu\text{m}</math> L3=340 <math>\mu\text{m}</math>    <math>\theta = 21^\circ</math></p>

Figure 2-15 Four types of springs, (a) serpentine spring, (b) box spring, (c) meander spring, (d) skewed box spring.

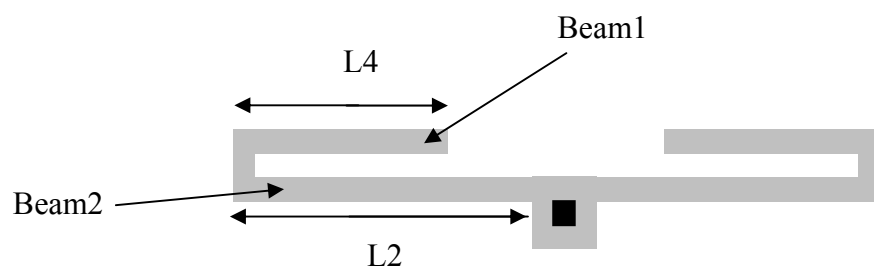


Figure 2-16 An example of box springs

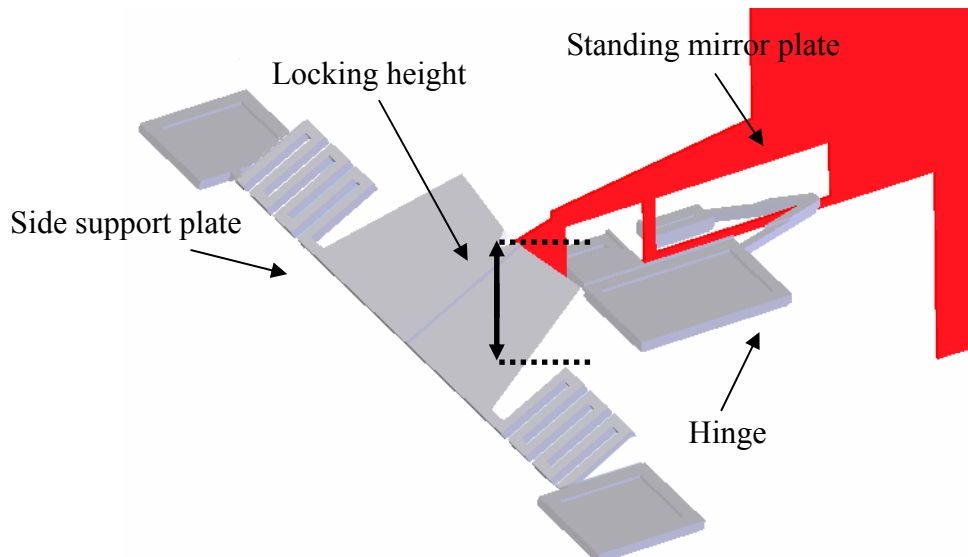


Figure 2-17 Cross-section view of the side latch.

## 2-6 Micromachined mirrors without etch holes

In order to free large microstructure, etch holes are inevitable in the surface micromachining. However, etch holes cause two major effects on the optical properties of micromachined mirrors, namely, diffraction and reduction of reflectivity [29]. These are undesirable in free-space optical systems. The etching holes can be eliminated if backside etch is employed, as shown in Figure 2-18. The big hole in the backside of the substrate was used for HF release without etch holes in the micromirror surface. However, the large open hole in the backside will cause the silicon device layer and buried oxide to break due to the residual stresses [30, 31]. Hence, another approach for backside etching was used to increase the yield of fabrication. As shown in Figure 2-19, the backside pattern was changed to an array of rectangles. The goal of this design is to make the exposed area of oxide after DRIE as small as possible, and therefore reducing the effect of the residual stresses. After the backside etch, the oxide layer could be etched by HF. The array of silicon pillars would drop during the release process. Hence the final pattern after release is identical to Figure 2-18 (b).

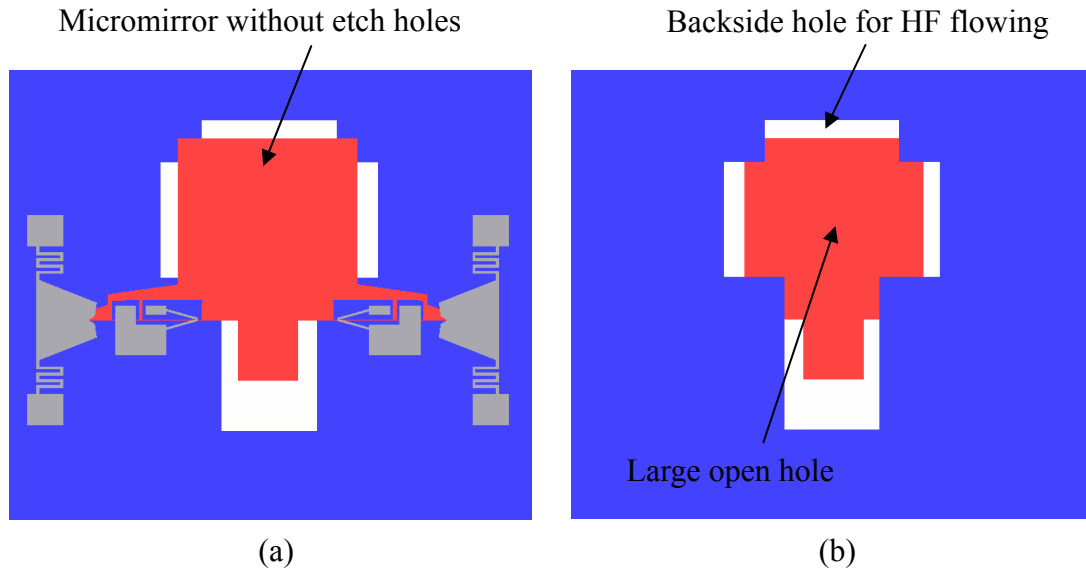


Figure 2-18 Backside pattern with a large open hole.

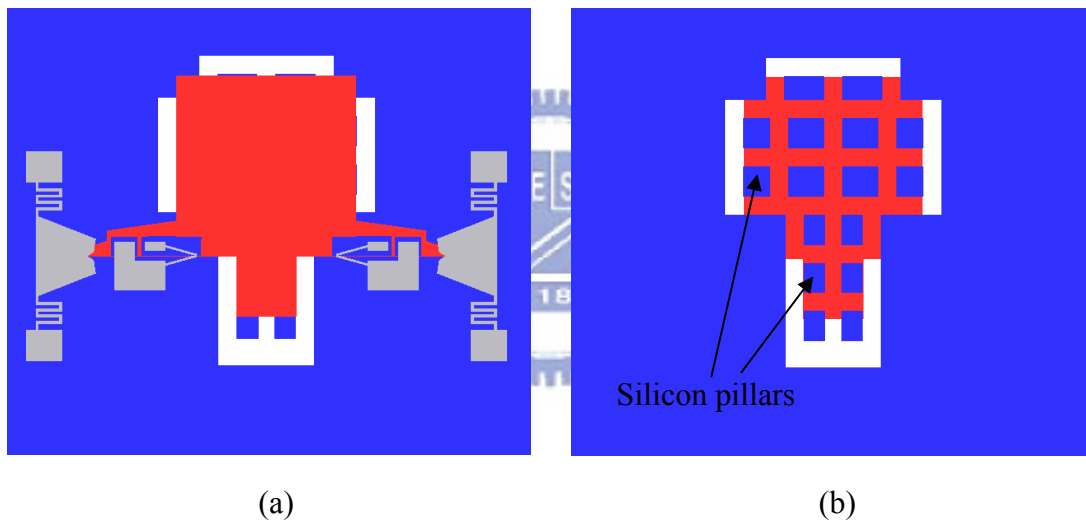


Figure 2-19 Backside pattern with a pillar array.

## 2-7 Summary

The V-shaped hinge is used to address the problems of play. Flexible side latch can provide a force on the hinged structure for better robustness. One-push operation reduces the assembly time and complexity. The mirror without etch holes is used to improve the optical characteristics. In the next Chapter, the fabrication process will be discussed.

# Chapter 3

## Fabrication Process

In this chapter, the surface micromachining-like fabrication process for the proposed device, which integrates the SOI wafer and the SU-8 photoresist, is described. The related process parameters are also presented. Finally, the encountered problems during fabrication are discussed.

### 3-1 Integration of SOI and SU-8

Flatness is an important requirement for optical devices. The SOI wafers are used due to its flat surface characteristic. Using SOI wafers also can simplify the process flow. SU-8 has good mechanical property and low process temperature. Therefore, the proposed device was fabricated by combining SOI wafers with SU-8. Table 3-1 is a brief comparison between the common surface micromachining fabrication technology and the proposed SOI with SU-8 fabrication process. The advantages of low process temperature and structure flatness make the SOI with SU-8 process much more suitable for optical applications compared with the general surface micromachining fabrication.

Table 3-1 Comparison of process

	Structural layers	Process temperature	Structure flatness	Process complexity
MUMPs	Polysilicon	High	Low	High
SOI+polysilicon	SCS and polysilicon	High	High	High
SOI+SU-8	SCS and SU-8	Low	High	Low

Figure 3-1 is the cross-section view of a 90° micromirror fabricated using this process. The detailed process flow and parameters will be discussed in the following sections.

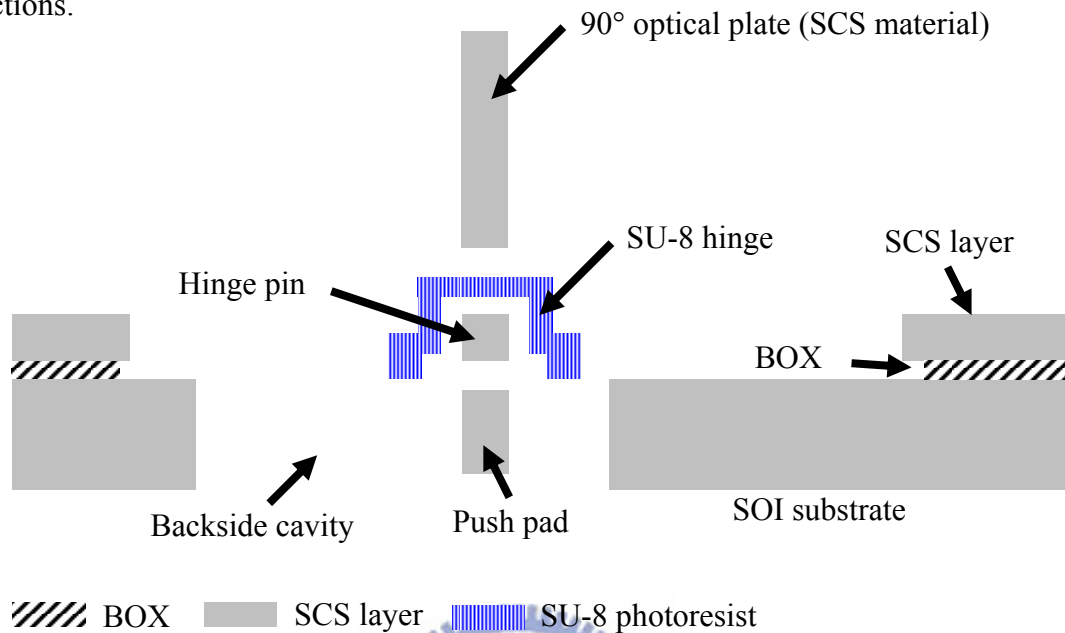


Figure 3-1 Schematic of a 90° micromirror.

### 3-2 Process Flow

The fabrication process for the proposed micromirror device is illustrated in Figure 3-2. Most fabrication processes were performed in the Nano Facility Center at National Chiao Tung University. The detailed process descriptions and parameters are presented as following.

#### Step A: SOI starting wafer

The process started with a SOI wafer, as shown in Figure 3-2 (1). The SOI specification is listed in the following.

Diameter	100 ± 0.1 mm
Device layer	5 ± 0.5 μm
BOX thickness	2 μm ± 5%
Handle layer	400 ± 10 μm

#### Step B: Wafer cleaning

First of all, a standard RCA clean process was performed on the bare SOI wafer. The purpose of this process is to remove contaminants on the surface of the wafer. Contamination results in reduced component service life, degraded performance characteristics and reduced reliability. The detailed RCA clean flow can be found in [32].

#### Step C: Backside oxide deposition

PECVD was utilized to deposit 3μm-thick silicon oxide on the backside of the wafer, as shown in Figure 3-2 (2). This oxide layer was used as a hard mask in a later ICP process. The process parameters are listed in the following.

SiH <sub>4</sub> flow rate	5 sccm
N <sub>2</sub> O flow rate	90 sccm
Process pressure	400 mtorr
Process temperature	350 °C
RF power	10 W
Deposition time	45 min.

#### Step D: Photolithography process – optical frame structure definition (Mask1)

Mask1 defines the optical frame structures in the 5 μm thick layer. The SCS layer was etched with a photoresist mask by ICP. FH6400 positive photoresist was selected as the mask material. The process parameters are listed in the following.

HMDS priming	Vapor prime oven
Spin coating	Spread speed = 1000 rpm for 10 sec. Spin speed =2000 rpm for 35 sec.
Soft bake	90 °C hotplate for 150 sec.
Alignment	Karl Suss MA6 mask aligner
Exposure	90 sec
Development	Developer FHD-5 for 1 min.
Rinse	DI water for 1 min.
Hard bake	120 °C hotplate for 30 min.

#### Step E: ICP etching

ICP DRIE was used to anisotropically etch the 5  $\mu\text{m}$  thick device layer of the SOI wafer, as shown in Figure 3-2 (3). The ICP process was done by the ICP etching service of ITRC (Instrument Technology Research Center).

#### Step F: Photolithography process – anchor definition (Mask2)

Mask2 is used to define the anchor positions. The 2  $\mu\text{m}$  thick BOX of the SOI wafer was etched using RIE. AZ4620 photoresist was used as the RIE mask. The process parameters are listed in the following.

HMDS priming	Vapor prime oven
Spin coating	Spread speed = 1000 rpm for 10 sec. Spin speed =2500 rpm for 30 sec.
Soft bake	90 °C hotplate for 20 min.
Alignment	Karl Suss MA6 mask aligner
Exposure	350 sec.
Development	Developer AZ-300 for 4 min. 35 sec.
Rinse	DI water for 1 min.
Hard bake	120 °C hotplate for 60 min.

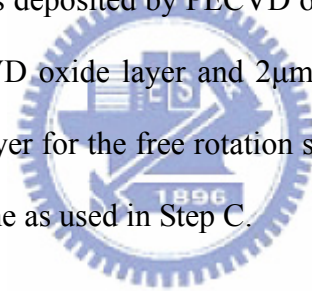
### Step G: Reactive ion etching

The SAMCO RIE-10N etcher was used to remove the BOX layer which was not covered by the photoresist mask. The etching depth was 2  $\mu\text{m}$ , as shown in Figure 3-2 (4). The following shows the RIE parameters.

SF <sub>6</sub> flow rate	30 sccm
CHF <sub>3</sub> flow rate	10 sccm
Helium back side cooling	15 sccm
Process pressure	50 mtorr
RF power	100 W
Etch time	22 min.

### Step H: Oxide deposition

A 3  $\mu\text{m}$  thick SiO<sub>2</sub> was deposited by PECVD on the top side of the SOI wafer. This 3 $\mu\text{m}$  thick PECVD oxide layer and 2 $\mu\text{m}$  thick BOX layer of SOI were used as a sacrificial layer for the free rotation space in the anchor. The process parameters are the same as used in Step C.



### Step I: Photolithography process – anchor definition (Mask2)

Mask2 was used again to define the anchor positions. The 3 $\mu\text{m}$  thick SiO<sub>2</sub> deposited in Step H was etched using RIE etcher. AZ4620 photoresist was used as the mask. The photolithography process parameters are listed in the following.

HMDS priming	Vapor prime oven
Spin coating	Spread speed = 1000 rpm for 10 sec. Spin speed = 2000 rpm for 30 sec.
Soft bake	90 °C hotplate for 30 min.
Alignment	Karl Suss MA6 mask aligner
Exposure	350 sec.
Development	Developer AZ-300 for 4 min. 35 sec.



Rinse	DI water for 1 min.
Hard bake	120 °C hotplate for 60 min.

#### Step J: Reactive ion etching

As shown in Figure 3-2 (5), the 3 $\mu$ m thick oxide was etched with the following RIE parameters.

SF <sub>6</sub> flow rate	30 sccm
CHF <sub>3</sub> flow rate	10 sccm
Helium back side cooling	15 sccm
Process pressure	50 mtorr
RF power	100 W
Etch time	32 min.

#### Step K: SU-8 photolithography process – latch and hinge definition (Mask3)

Mask3 defined the side latch structures and the hinge elements, as shown in Figure 3-2 (6). These structures were made of 13- $\mu$ m-thick SU-8 negative photoresist. The SU-8 process parameters are listed in the following.

Dehydration bake	120 °C hotplate for 30min.
Spin coating	Spread speed = 500 rpm for 10 sec. Spin speed =3000 rpm for 30 sec.
Pre-bake	65 °C hotplate for 1 min.
Soft bake	95 °C hotplate for 2 min.
Alignment	K-310P-100S
Exposure	4 sec.
Post-exposure bake	65 °C hotplate for 1 min. 95 °C hotplate for 2 min.
Development	SU-8 Developer for 3 min.
Rinse	IPA for 1 min
Hard bake	200 °C hotplate for 20 min.

#### Step L: Double side photolithography process – backside cavity definition (Mask4)

Mask4 defined the backside cavity of the substrate which was as a room for the assembly procedure. The oxide layer deposited in Step C, which was used as an ICP mask, was etched by RIE with photoresist AZ4620 mask. The photolithography parameters are listed in the following.

HMDS priming	Vapor prime oven
Spin coating	Spread speed = 1000 rpm for 10 sec. Spin speed =2000 rpm for 40 sec.
Soft bake	90 °C hotplate for 25 min.
Alignment	EV620 mask aligner
Exposure	12 sec.
Development	Developer EDP-1000 for 1 min. 10 sec.
Rinse	DI water for 1min.
Hard bake	120 °C hotplate for 60 min.

#### Step M: Reactive ion etching

As shown in Figure 3-2 (7), the 3 $\mu$ m thick backside oxide was etched with the RIE parameters as described in Step J.

#### Step N: ICP etching

The 400 $\mu$ m thick substrate of the SOI wafer was etched by ICP, as shown in Figure 3-2 (8). Oxide was chosen as the ICP mask instead of the photoresist due to the higher ICP selectivity of silicon to SiO<sub>2</sub> compared to that of silicon to photoresist. The thick etching depth, 400  $\mu$ m in this case, needs a thick photoresist as mask. This will increase the process complexity. Another reason is the photoresist may be burned during the long ICP process time. This will result in destroyed patterns. The backside ICP process was done by the ICP etching service of C SUM MFG. Ltd.

Step O: Oxide release

The devices were released when the sacrificial oxide layer was removed by 49% HF solution and rinsed in IPA for 10 minutes, as shown in Figure 3-2 (9).

Step P: Micromanipulator assembly

Finally, the released microstructures were manually assembled using micromanipulator station, as illustrated in Figure 3-2 (10).



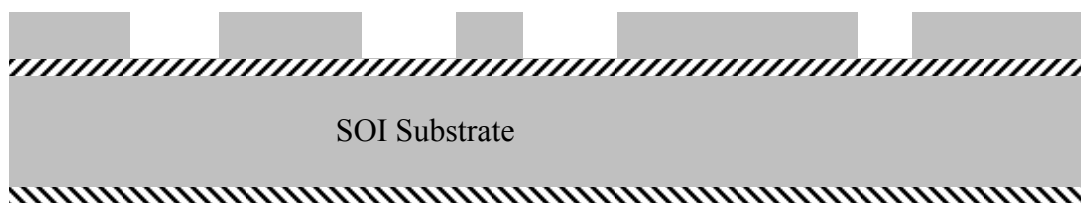
////// BOX    ■ SCS layer

(1) SOI wafer cleaning (Step A, Step B)



////// BOX    ■ SCS layer    \\\\\\\ PECVD Oxide

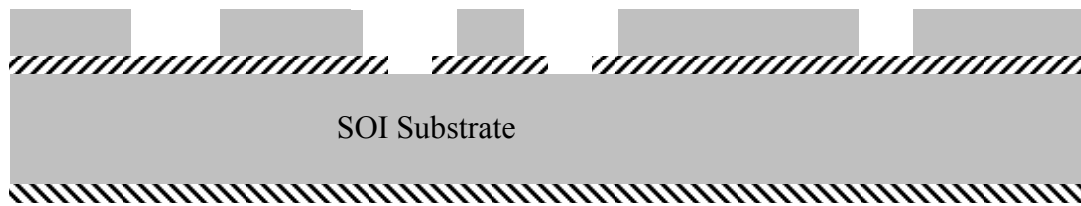
(2) Backside oxide deposition (Step C)

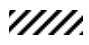




////// BOX    ■ SCS layer    \\\\\\\ PECVD Oxide

(3) Frontside ICP DRIE (Step D, Step E)




Figure 3-2 Fabrication process of the proposed device.



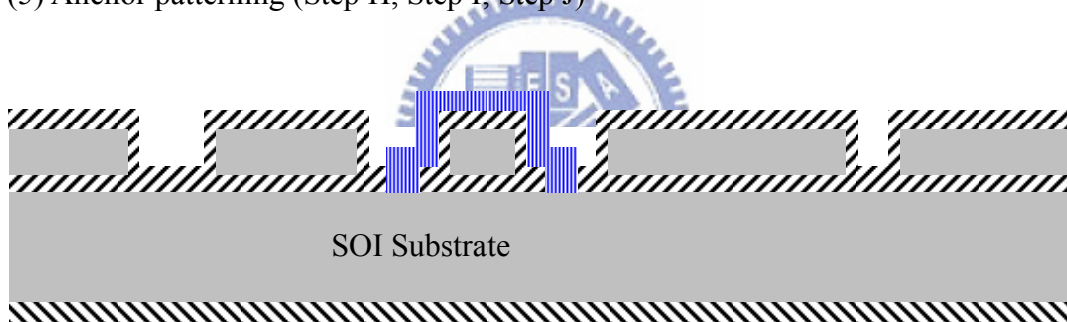
 BOX  
  SCS layer  
  PECVD Oxide

(4) Anchor patterning (Step F, Step G)



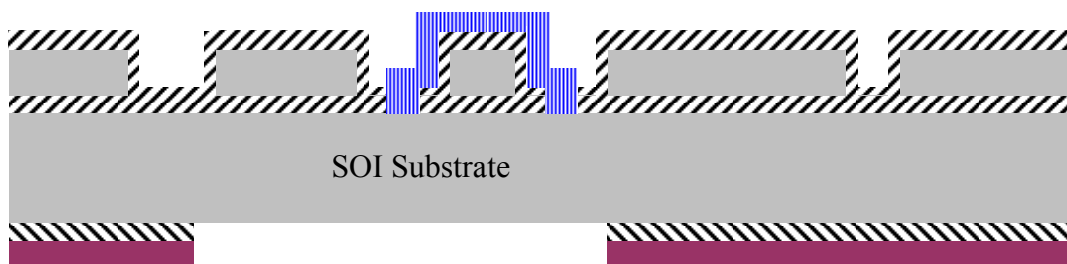
 BOX  
  SCS layer  
  PECVD oxide

(5) Anchor patterning (Step H, Step I, Step J)



 BOX  
  SCS layer  
  PECVD oxide  
  SU-8 photoresist

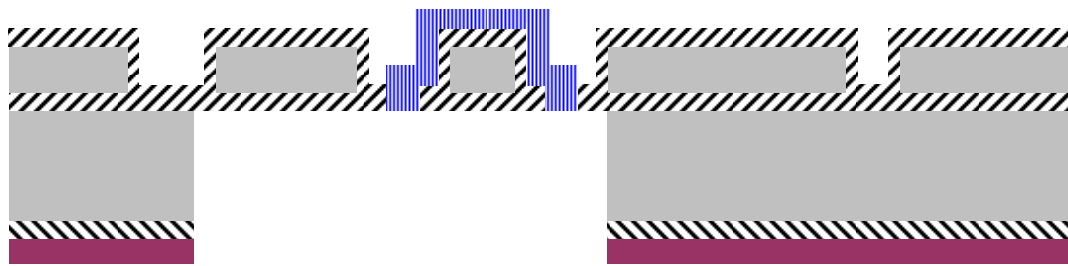
(6) SU-8 patterning (Step K)








 BOX  
  SCS layer  
  PECVD oxide  
  SU-8 photoresist  
 photoresist

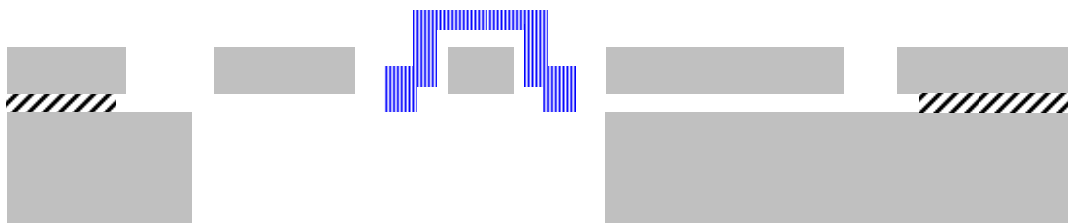
(7) Backside oxide patterning (Step L, Step M)

Figure 3-2 Fabrication process of the proposed device (continued).



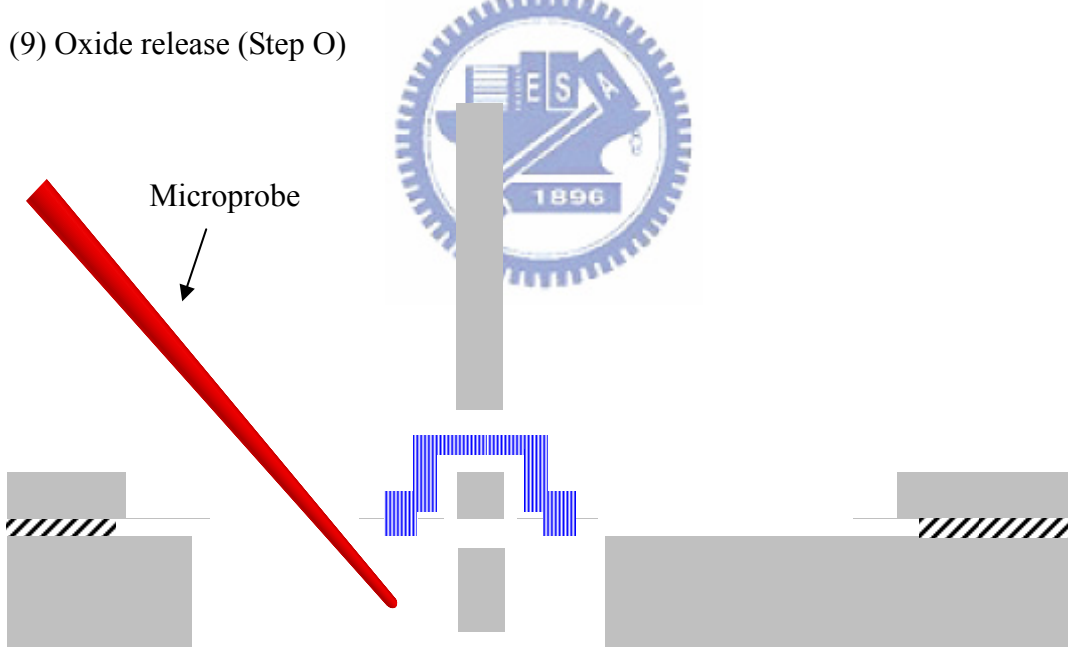
 BOX  
  SCS layer  
  PECVD oxide  
  SU-8 photoresist  
 photoresist




(8) Backside ICP etching (Step N)



 BOX  
  SCS layer  
  SU-8 photoresist

(9) Oxide release (Step O)



 BOX  
  SCS layer  
  SU-8 photoresist

(10) Microprobe assembly (Step P)

Figure 3-2 Fabrication process of the proposed device (continued).

The photographs of the device structures during the fabrication processes are presented in Figure 3-3. Figure 3-3 (a) and Figure 3-3 (b) show the minimum feature size (5  $\mu\text{m}$  hinge pin) was defined after frontside ICP. The SU-8 V-shaped hinge and side latch structures were well patterned as shown in Figure 3-3 (c) and Figure 3-3 (d). The released structures shown in Figure 3-3 (e) and Figure 3-3 (f) are mirrors with the push pad and without the push pad, respectively. The mirrors without etch holes after releasing are shown in Figures 3-3 (g)-(j). Figure 3-3 (g) has a backside pattern with a big hole; Figure 3-3 (i) has a silicon pillar array in the backside pattern.

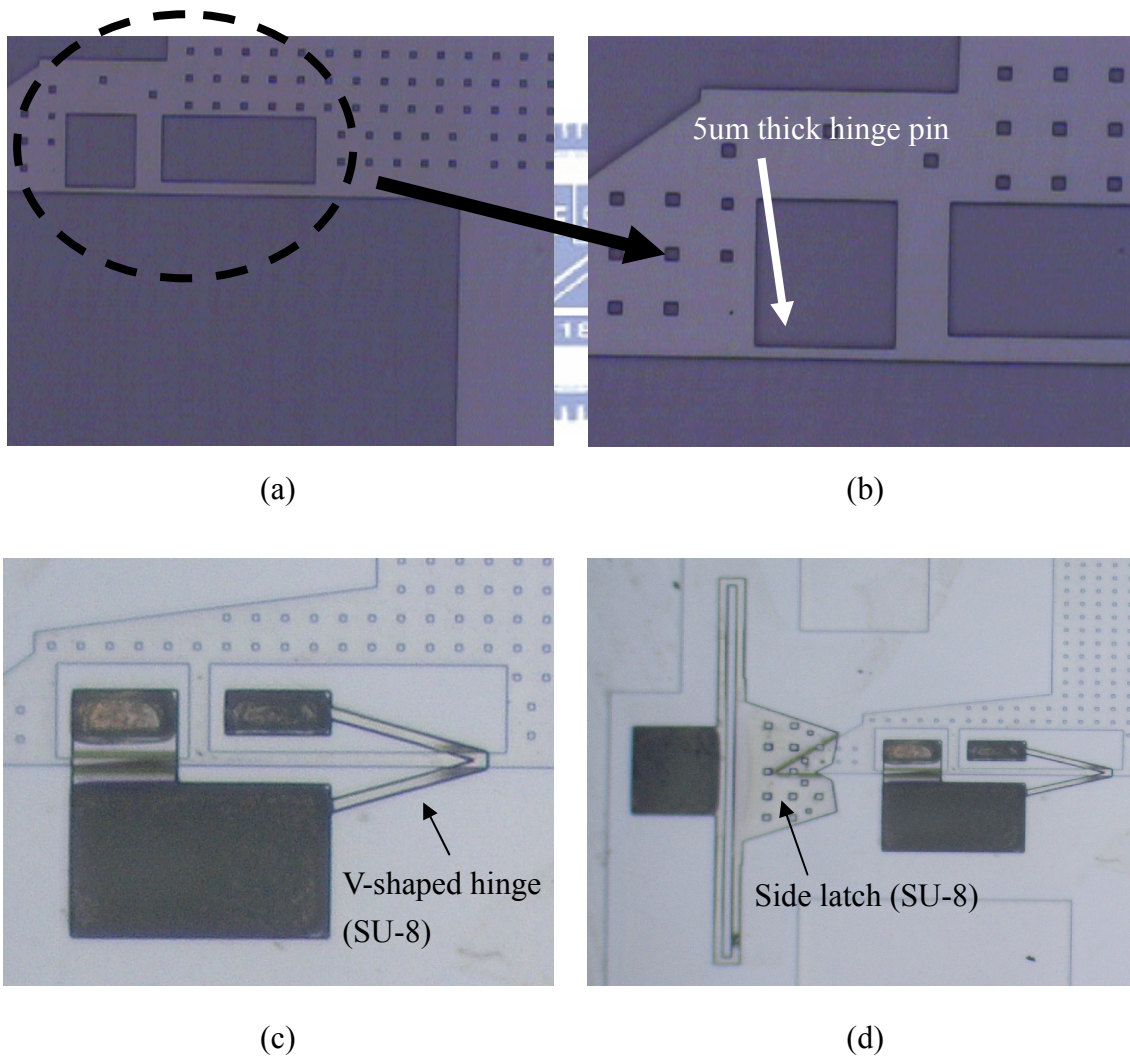
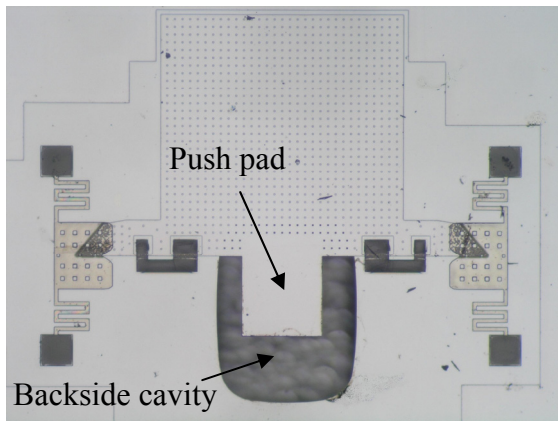
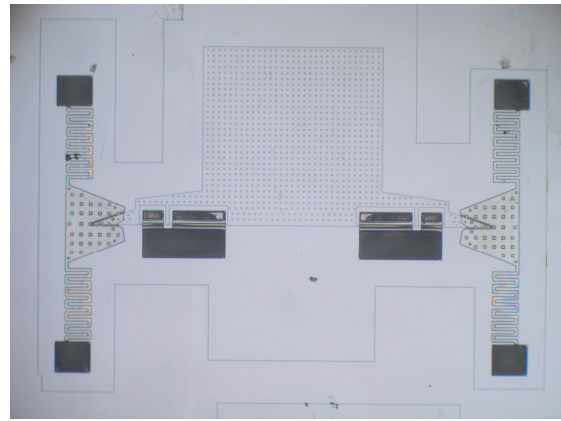


Figure 3-3 Photographs of the device structures during the fabrication processes.

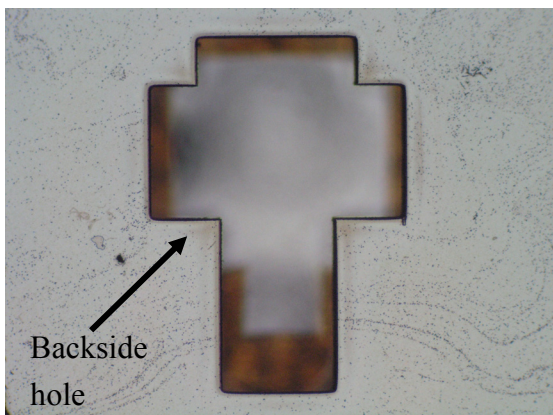




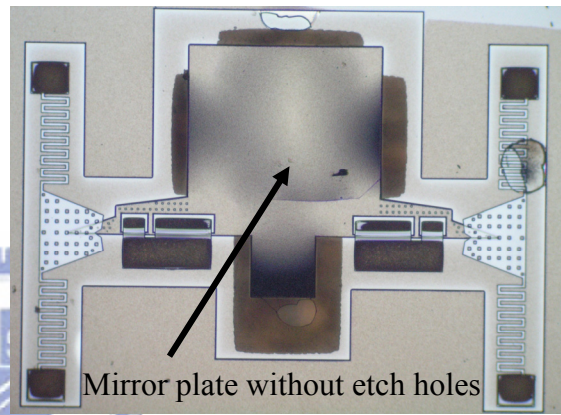
(e)



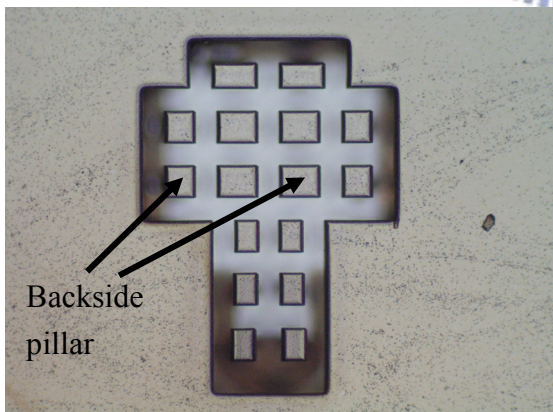
(f)



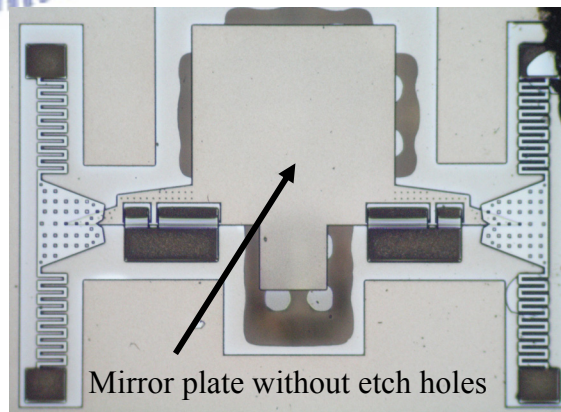
(g)



(h)



(i)



(j)

Figure 3-3 Photographs of the device structures during the fabrication processes (continued).

### **3-3 Fabrication problems and discussions**

Two potential problems with the fabrication process are SU-8 adhesion and stiction. The adhesion strength of SU-8 to silicon is susceptible to fabrication parameters. The stiction between large mirror plate and substrate causes the assembly failure. The solutions to address these problems are discussed and presented in following sections.

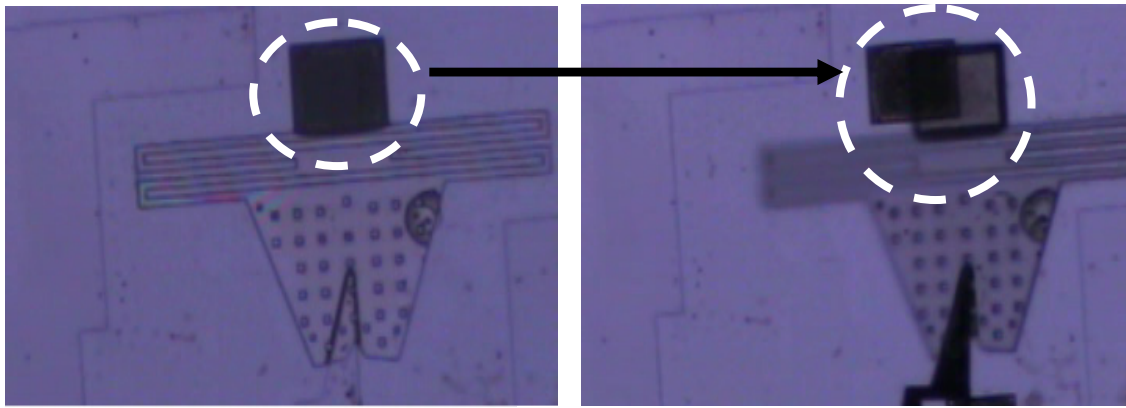
#### **3-3-1 Adhesion of SU-8 structures**

During the SU-8 related process steps, the adhesion strength of the SU-8 structures to the silicon substrate may be weak. This can cause the SU-8 layer to peel off during the fabrication or operation. Figure 3-4 shows that a weak SU-8 anchor peeled off during the assembly process. In order to enhance the adhesion of SU-8 to the substrate, the process parameters are modified.

From [33-34], the adhesion of SU-8 to silicon can be easily affected by substrate cleanness and process parameters. The silicon wafer surface has to be extremely dry and clean. Peeling can also happen in the presence of a native oxide layer on the silicon before SU-8 coating. The SU-8 curing parameters are another important factor for adhesion failure. Slow ramping of the curing temperature is needed in order to improve the substrate adhesion. Accordingly, the process parameters of the SU-8 are modified as in Table 3-2, obeying the following rules,

1. Dry and clean silicon substrate is critical.
2. Native silicon oxide is removed before SU-8 coating.
3. Slow ramping of the SU-8 curing temperature is very important to enhance adhesion.





(a)

(b)

Figure 3-4 (a) The mirror plate is lifted by a probe, (b) as the plate is lifted further, the weak SU-8 anchor is detached.

Table 3-2 Modified SU-8 parameters

Step	Parameter	Comment
HF dip	100:1 HF dip 10 sec.	HF dips to remove native oxide layer prior to SU-8 deposition.
Dehydration bake	150 °C hotplate for 20 min,	Dry substrate is necessary.
Spin coating	Spread speed = 500 rpm for 10 sec. Spin speed =3000 rpm for 30 sec.	
Pre-exposure bake	45 °C → 65 °C for 1 min. 65 °C → 95 °C for 2 min. 95 °C → 40 °C Where ramp rate is 1 °C / min.	(1) Curing temperature with slow ramping is very important to adhesion. (2) Slow cooling ramping is also required.
Alignment	K-310P-100S	
Exposure	4 sec.	
Post-exposure bake	45 °C → 65 °C for 1 min. 65 °C → 95 °C for 2 min. 95 °C → 40 °C Where ramp rate is 1 °C / min.	(1) Curing temperature with slow ramping is very important to adhesion. (2) Slow cooling ramping is also required.
Development	SU-8 Developer for 3 min.	
Rinse	IPA for 1 min.	

The adhesion of SU-8 structures fabricated with the modified parameters are studied and analyzed in the following experiments. First, the adhesion problem is analyzed by the occurrence percentage of delamination in all processed SU-8 structures. Second, SU-8 spring structures are randomly pulled and intentionally broken using microprobes. It is recorded whether the SU-8 spring structures peel off before breaking. If the anchor area of the SU-8 spring is not detached before breaking, it means the SU-8 adhesion is strong enough. Figure 3-5 shows the micrographs of the experimental process. The SU-8 was pulled and broken by using a microprobe as shown in Figures 3-5 (a)-(c). Figure 3-5 (d) shows that the SU-8 anchor was still well in place even the spring was broken. There were totally 361 fabricated SU-8 samples. 86 samples were randomly selected for test. Experimental results show that the delamination of SU-8 anchors after release is zero among the 86 samples. The number of detached SU-8 anchors after breaking was 5. Therefore the failure rate is only 6%.

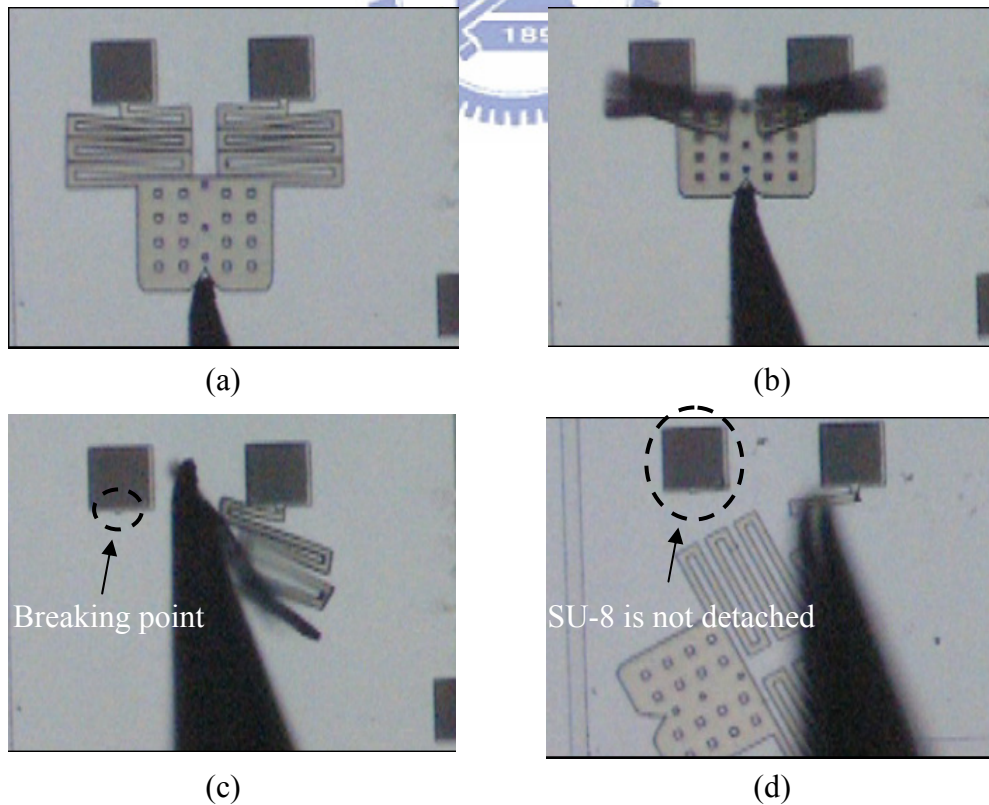


Figure 3-5 Experimental process of SU-8 adhesion test.

### 3-3-2 Vapor HF release

The final step in the fabrication process is to release the microstructure from the sacrificial oxide layer. When an aqueous HF solution is used for the release process, the surface tension can pull two structures together and result in the stiction of suspended structures to the substrate after rinsing in DI water or IPA. This stiction phenomenon can significantly reduce yield. As shown in Figure 3-6, the assembly process failed due to the stiction between large mirror plate and substrate. The mirror plate was not lifted as the pad was pushed down (Figure 3-6 (b)). The pad was broken as it was pushed further (Figures 3-6 (c), (d)). Vapor phase etching is a promising solution to address the stiction problem because it avoids the wet etching and rinsing steps. Hence the modified release process uses vapor HF to etch the oxide layer. Nevertheless, the vapor HF technique usually needs complicated apparatus. In this thesis, a simple method proposed by [35] was adopted for vapor HF releasing.

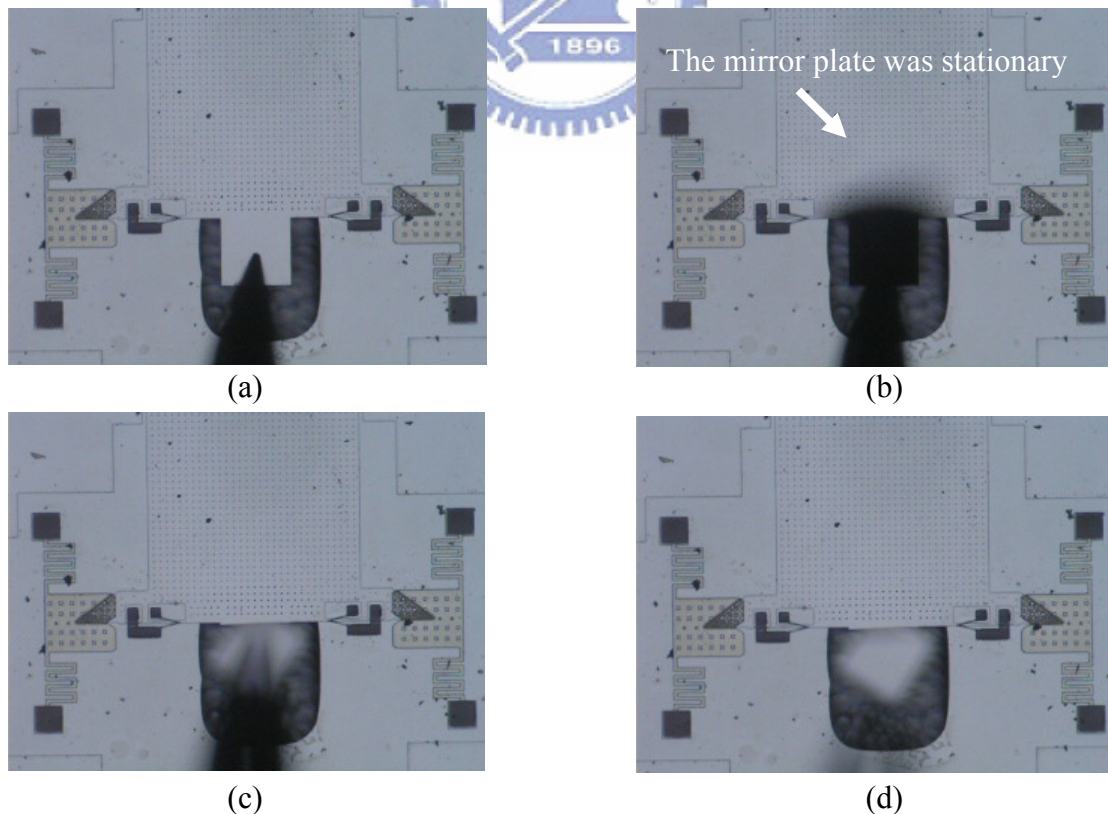


Figure 3-6 Assembly failure due to the stiction.

Figure 3-7 schematically illustrates the experimental setup of the vapor HF process. This system consists of two Teflon dishes, one plastic film, and one light bulb. First, liquid HF was poured into a Teflon beaker. Then the Teflon beaker was covered with a plastic film. The chip is placed on this plastic film with holes to ensure the HF vapor can pass through to the chip. Another Teflon dish caps the HF vessel to keep the HF vapor inside and avoids any leakage. The light bulb is used to warm up the chip and to control the temperature during the process. Figure 3-8 shows the setup used in this thesis. Obviously, these components are very cheap and simple; no complicated apparatus is necessary.

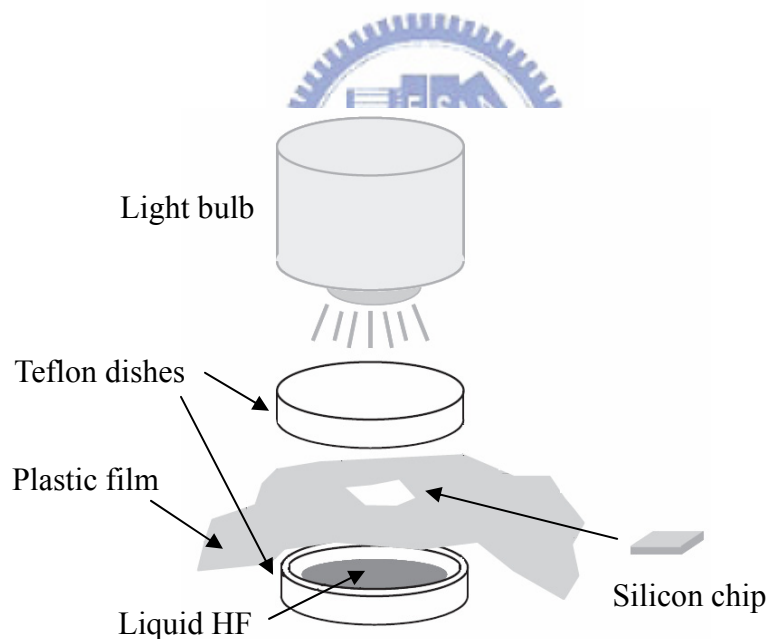


Figure 3-7 Schematic illustration of a vapor HF release apparatus. The chip is placed on a plastic film.

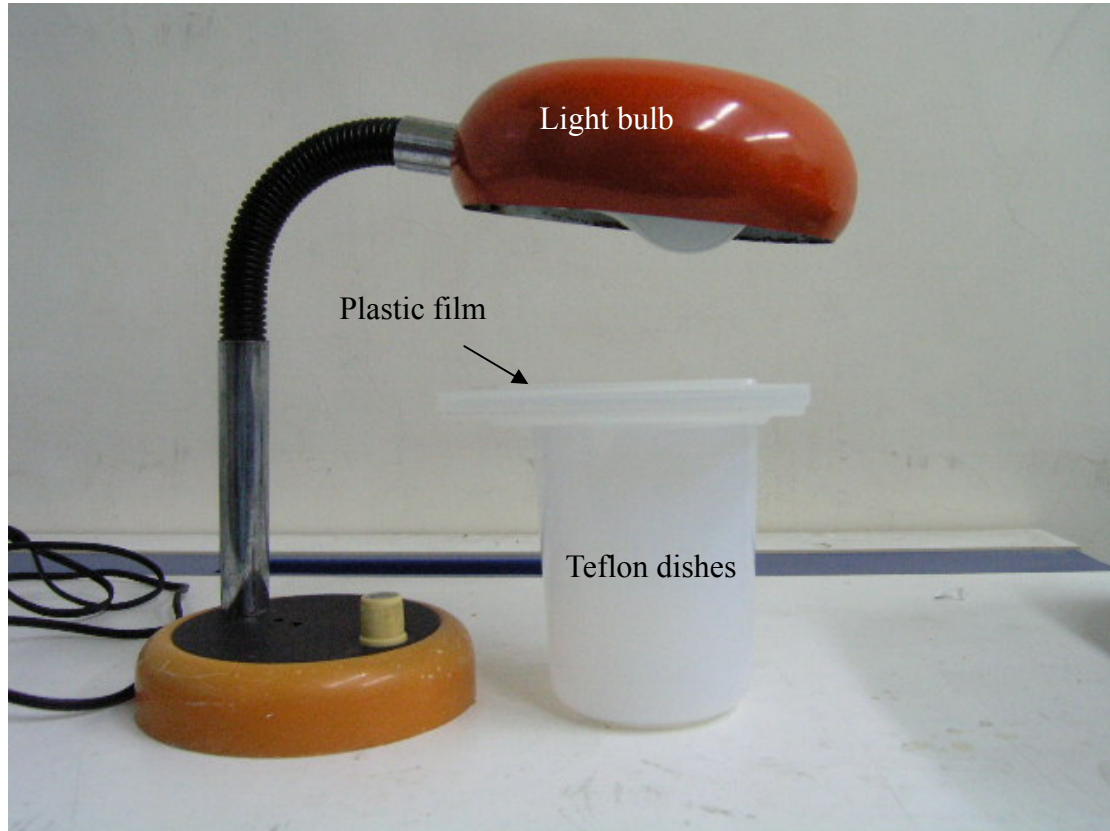
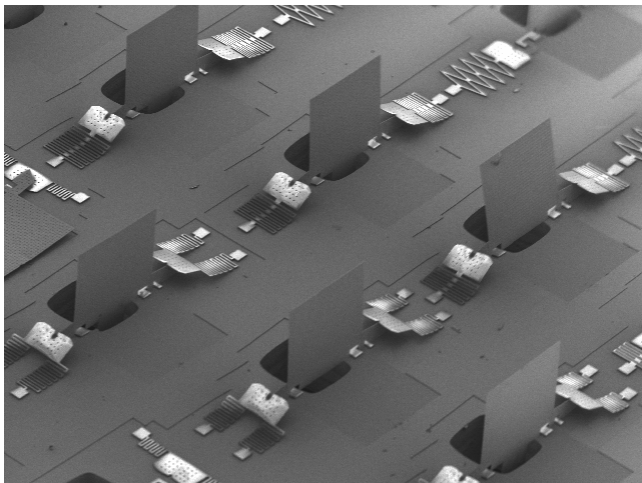


Figure 3-8 Vapor HF setup used in this thesis.

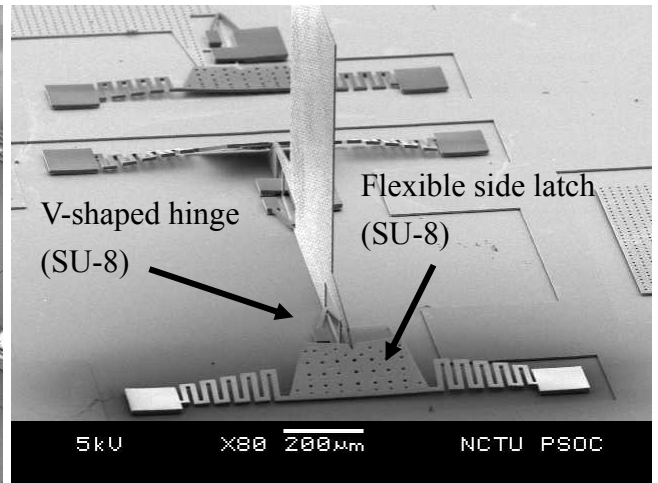
### 3-4 Fabricated structure

Figure 3-9 shows the SEM photographs of the device after assembly. Figure 3-9 (a) shows an array of the assembled mirrors. Figure 3-9 (b) is the mirror without the push pad and with the V-shaped hinges. Figure 3-9 (c) shows the mirror with the push pad and V-shaped hinges. Figure 3-9 (d) is the mirror without the etch holes and with conventional hinges. Figures 3-9 (e) and (f) are the close-up view of the V-shaped hinge and the cross-section view of the mirror, respectively. The assembly experiment will be discussed in Chapter 4.

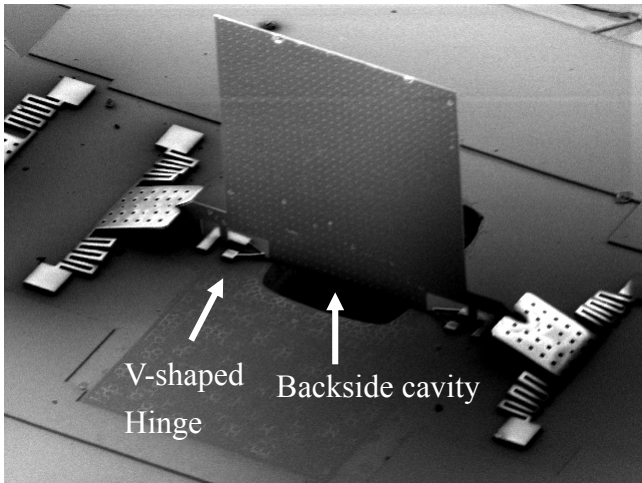




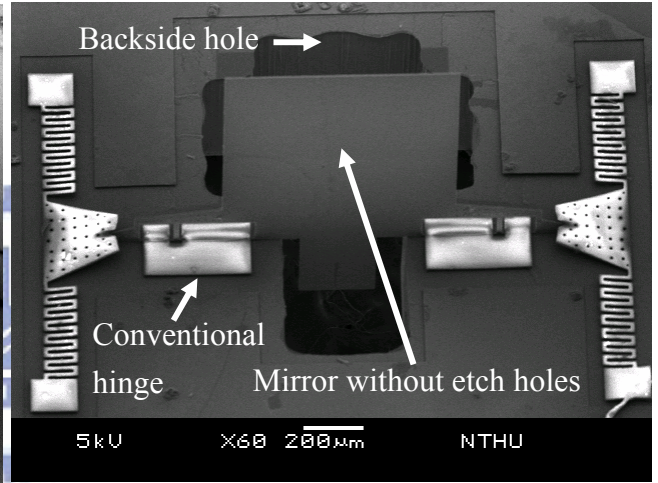
(a)



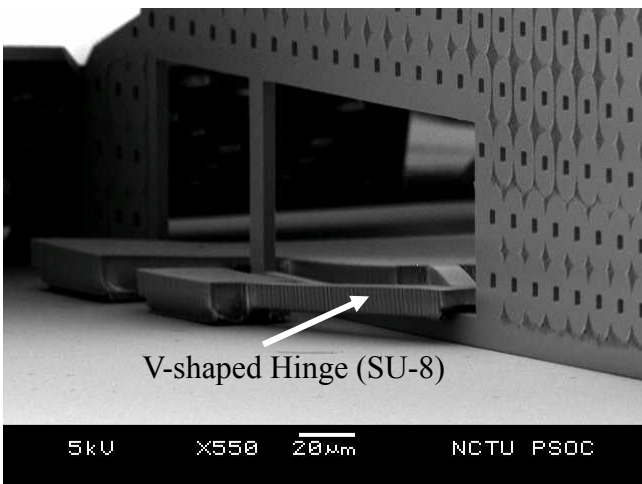
(b)



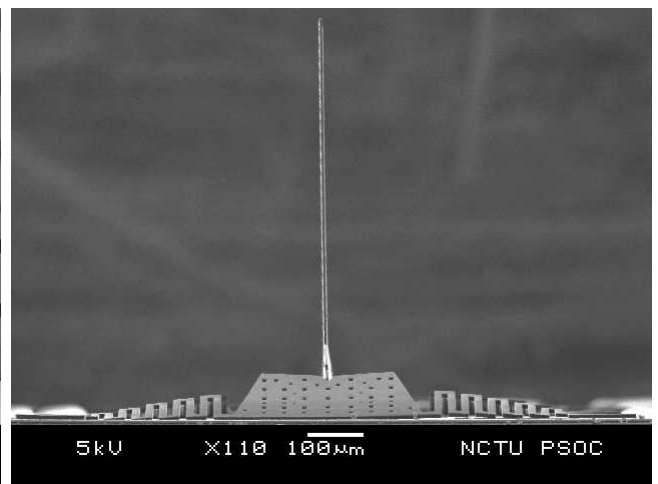
(c)



(d)



(e)



(f)

Figure 3-9 SEM photographs of assembled devices.

### **3-5 Summary**

The SU-8 adhesion and stiction problems can be improved by modified fabrication parameters and vapor HF release, respectively. The SEM photographs of assembled devices indicate the feasibility of the proposed assembly process. In the following chapter, the assembly experiment will be discussed.



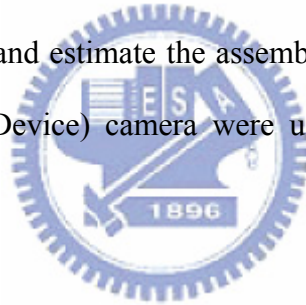
# Chapter 4

## Measurement and Experiment Results

This chapter presents the results of experiment and measurement. The assembly processes and failure modes are discussed in the first part. The second part shows the measurement of the V-shaped hinge and the mirror without etch holes.

### 4-1 Assembly Experiment

Devices were assembled with one push operation by micromanipulators. The experiments were used to verify the feasibility of this concept, find the problems during the assembly process, and estimate the assembly time. An optical microscope and CCD (Charge Coupled Device) camera were used to observe and record the experiments.



#### 4-1-1 Feasibility

A mirror with conventional hinges, a mirror with V-shaped hinges and a mirror without etch holes were assembled to verify the feasibility of the proposed assembly process. Figures 4-1 - 4-3 show the respective assembly results. All assemblies were very successful and the feasibility of the one push operation is verified. The mirror plate was smoothly lifted as the microprobe pushed the pad down, such as in Figures 4-1 (b) and 4-2 (b). Therefore, there is no stiction between the large mirror plate and the substrate. In Figure 4-3 (b), the backside of the mirror without etch holes is a cavity, therefore stiction is not an issue in this case. As the mirror plate was elevated further, the side latches were well pushed out of plane. Finally, the mirror plate slid into the V-shaped slots and locked in the upright position, such as in Figures 4-1 (c),



4-2 (c), and 4-3 (c). Figure 4-2 (e) shows the close-up view of the V-shaped hinge after assembly. Figure 4-2 (f) shows that the mirror plate slid well into the V-shaped slot of the side latch after assembly.

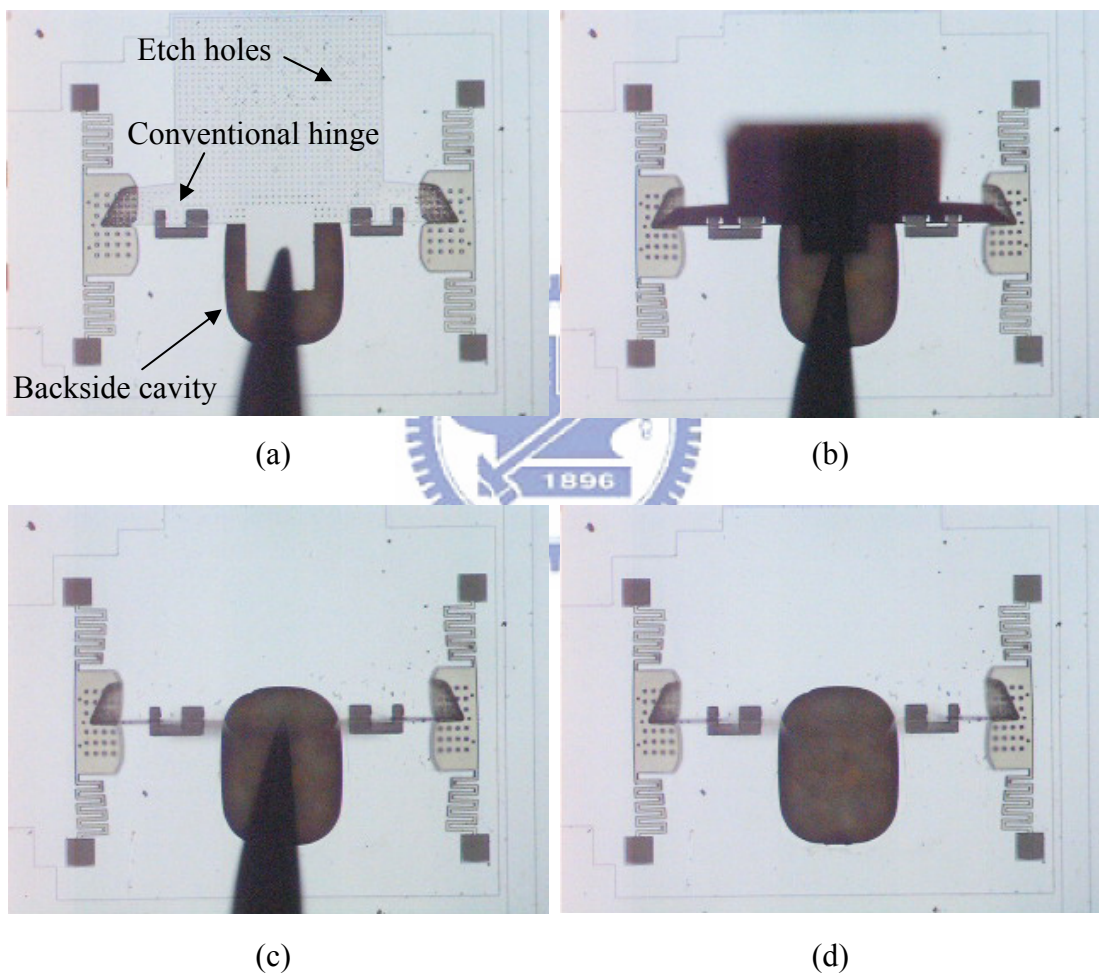


Figure 4-1 Assembly process of a 90° mirror with conventional hinges.

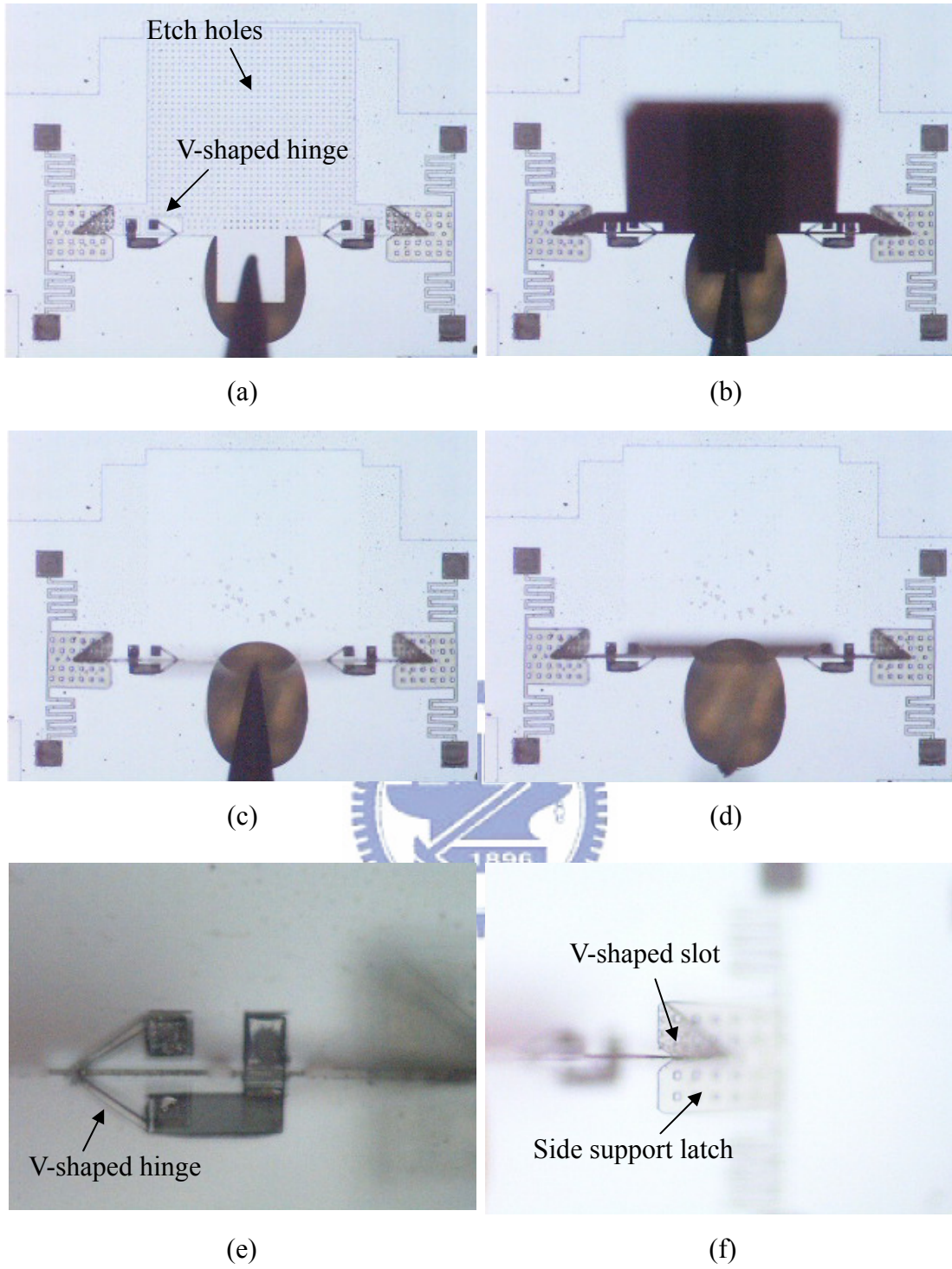


Figure 4-2 Assembly process of a 90° mirror with V-shaped hinges.

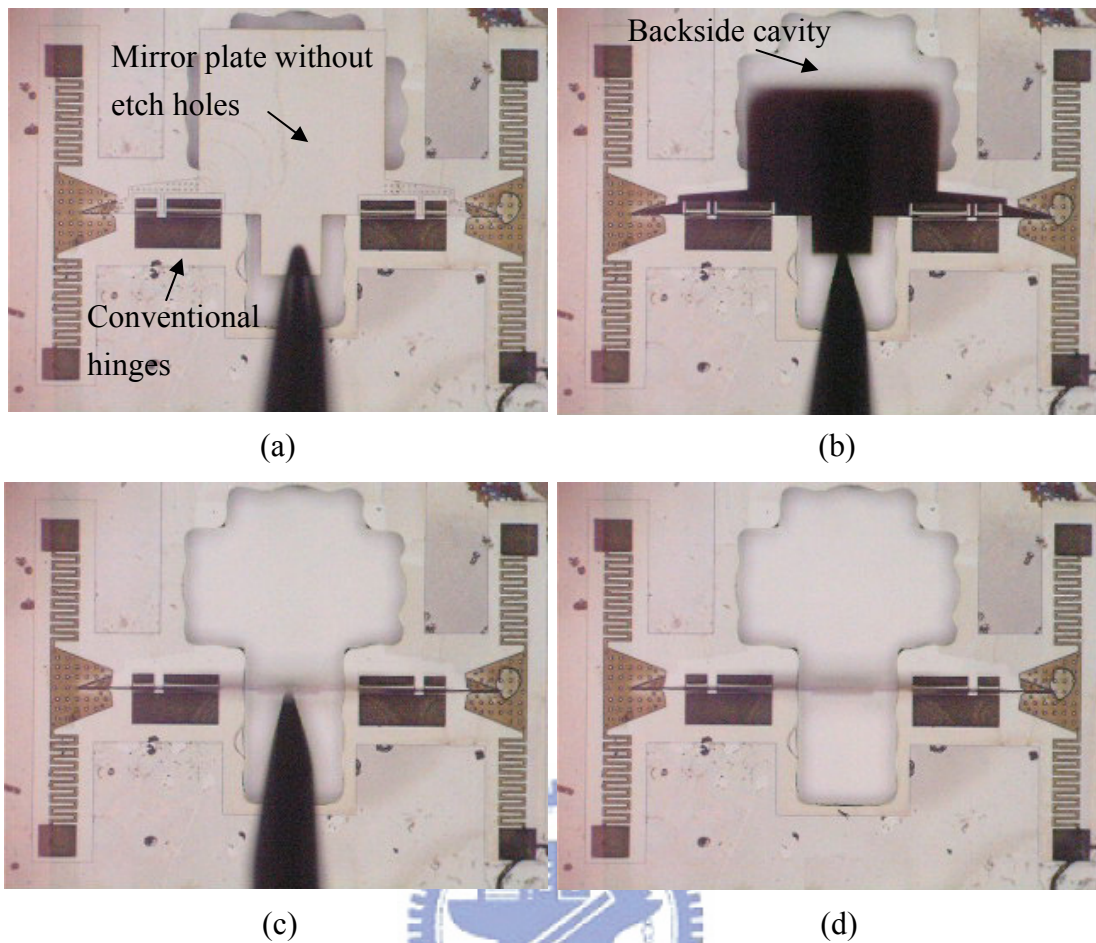


Figure 4-3 Assembly process of a 90° mirror without etch holes.

#### 4-1-2 Problems during the assembly process

Some problems during the assembly process were observed. As shown in Figure 4-4, Figure 4-4 (a) shows the mirror in the horizontal position. The side latch rotated out of plane when the mirror plate was lifted. Ideally, the mirror plate will slide into the V-shaped slot of the side latch when it is in the upright position. If the spring is too soft, the friction force between side plate and mirror plate can cause lateral displacement of the side plate as the mirror plate was rotated toward the upright position, as shown in Figures 4-4 (b) and (c). Hence the mirror plate did not slide into the V-shaped slot when it was upright. Another microprobe was needed to push the side plate back into correct position, as shown in Figures 4-4 (d) and (e). This, of course, increases the assembly time and complexity. The same situation happened to



other spring designs. Figures 4-5 (a), (c), (e) show the mirror was in the horizontal position. When the mirror plates were in the upright position, as shown in Figures 4-5 (b), (d), (f), they did not slide into the V-shaped slots. Optimization of spring design is need in the future.

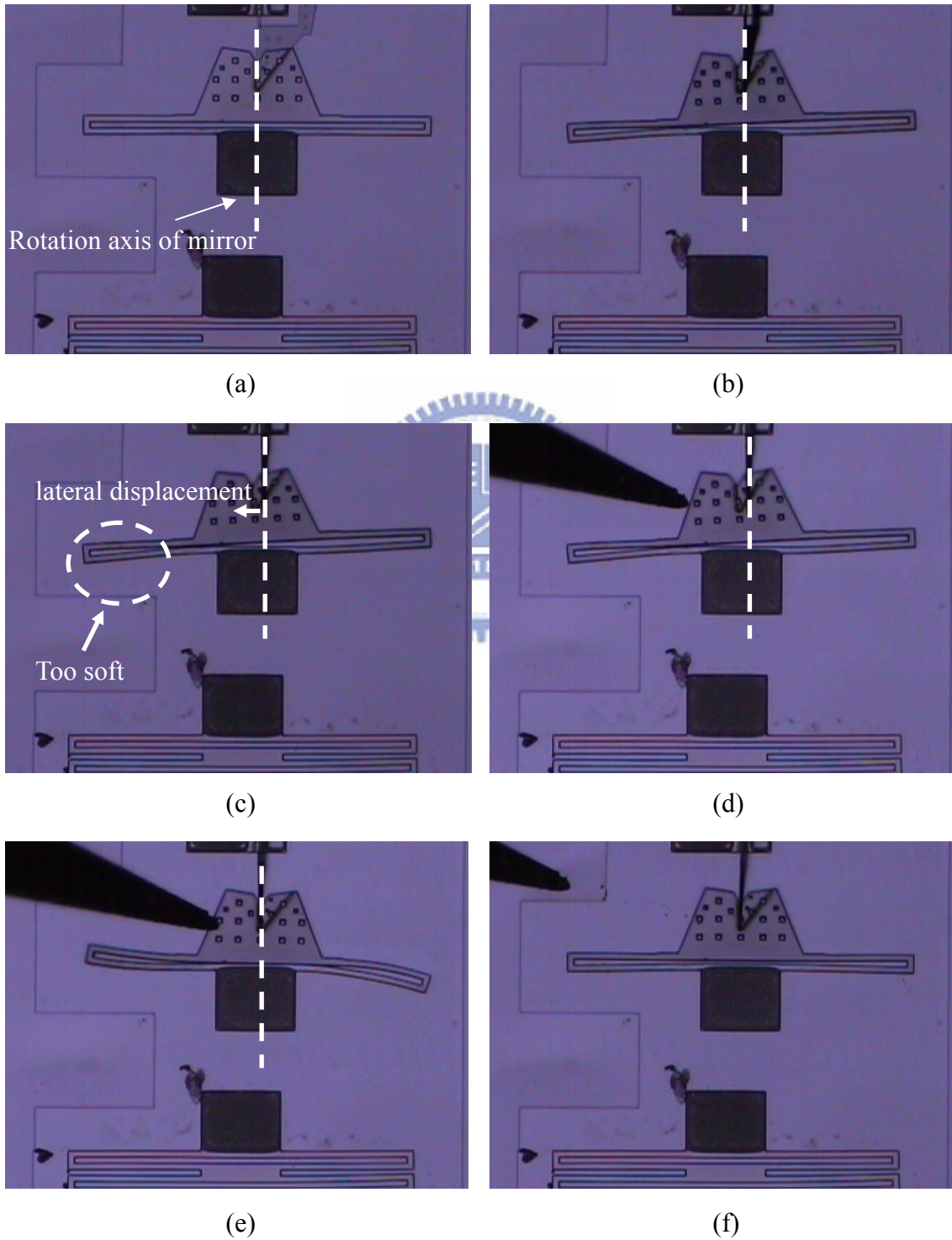
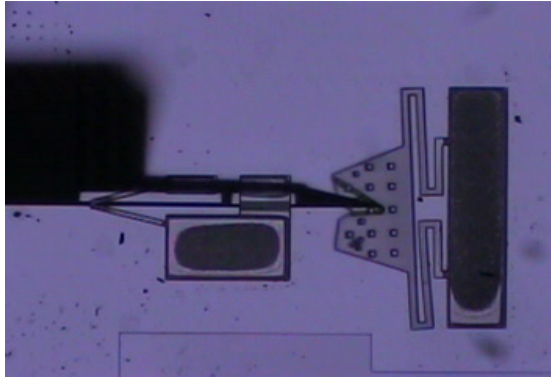
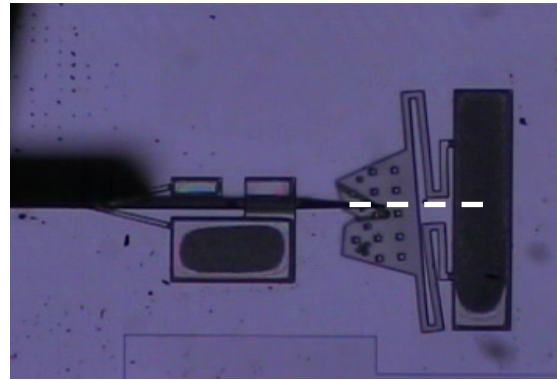


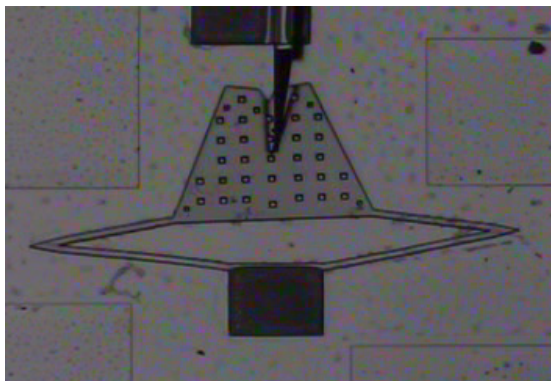
Figure 4-4 Assembly failure due to soft springs (box-type spring).



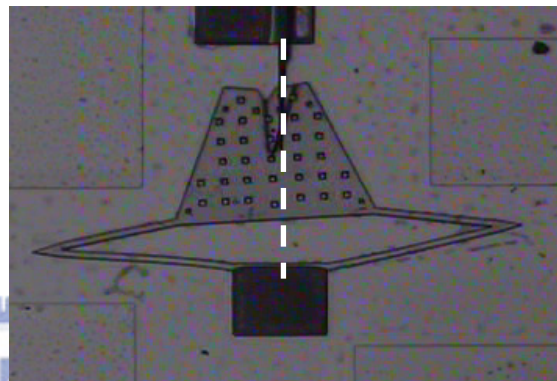
(a)



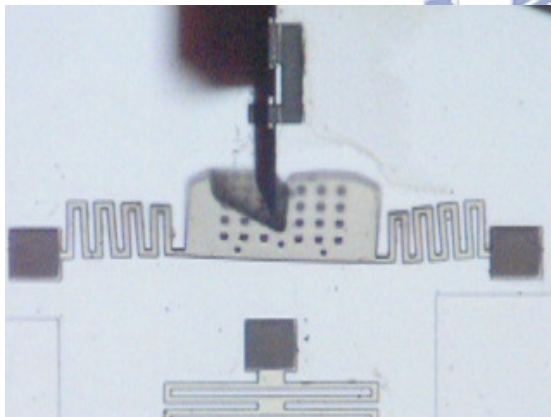
(b)



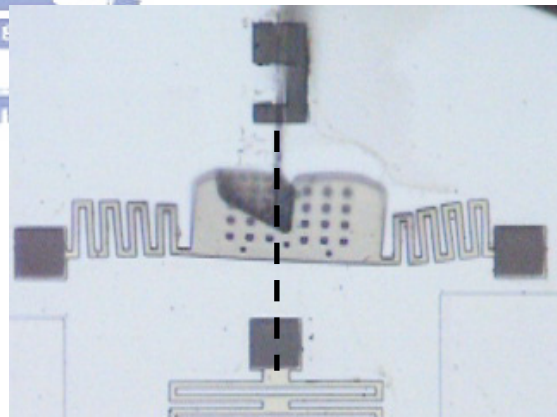
(c)



(d)



(e)



(f)

Figure 4-5 Assembly failure due to soft springs (other spring designs).

Another problem during the assembly process is the displaced hinge pins. When the mirror plate was lifted by the microprobe, ideally it rotated around the axis as shown in Figure 4-6 (a). The hinge pin should stay at the rotation axis after assembly, as shown in Figure 4-6 (b). The hinge pin was well locked between the two sides of the V-shaped hinge. But sometimes the hinge pin was displaced away from the rotation axis due to an unbalanced force during the assembly process, as shown in Figures 4-7 (b) and (c). Figure 4-7 (d) shows hinge pin was not locked between the two sides of the V-shaped hinge after assembly. Another probe was needed to push it back to the correct position, and therefore increasing the complexity.

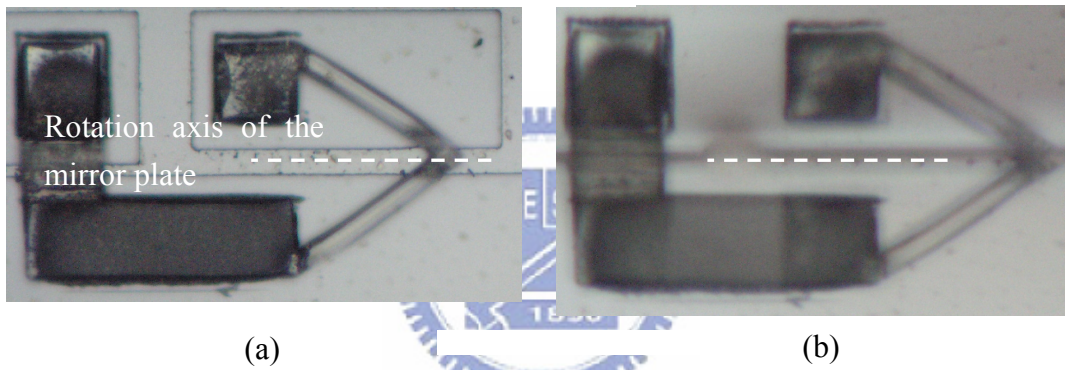


Figure 4-6 Successful assembly process.

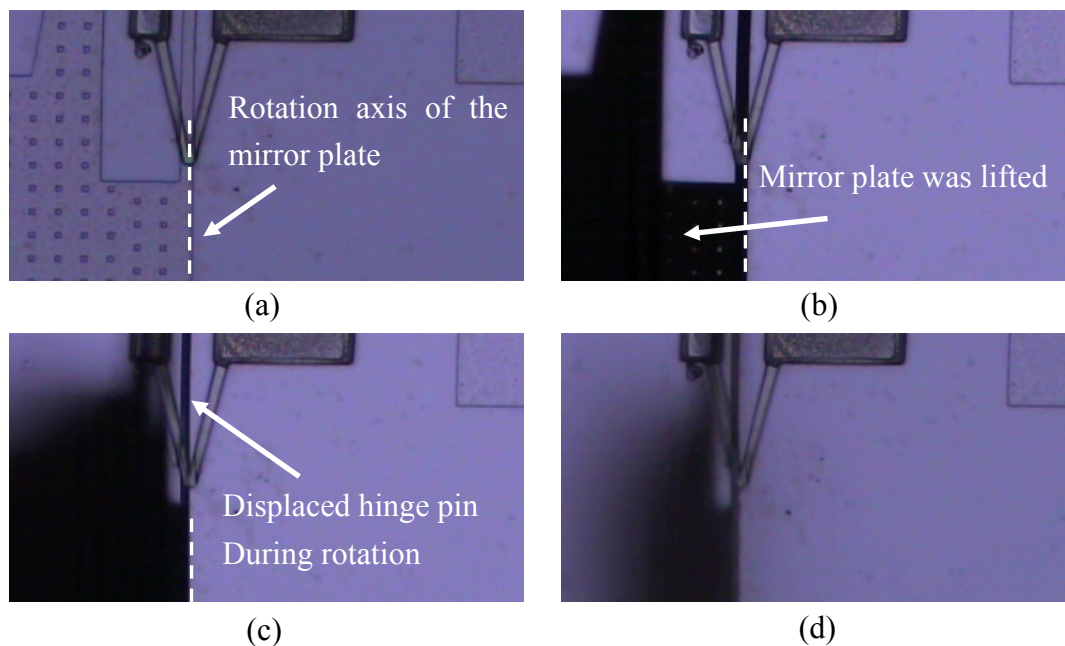


Figure 4-7 Failed assembly due to displaced hinge pins.



Assembly process with one push operation can greatly reduce the assembly time. In this experiment, a number of samples were assembled for estimating the assembly time. Assembly time was measured from the moment when the microprobe is moved to push pads to the moment when the whole assembly is completed. Table 4-1 lists the experiment results. If the mirror plate did not smoothly slide into the V-shaped opening of the side latch, the average assembly time was more than 80 seconds since another probe or even two probes were needed to push the side latch back into the correct position, as mentioned in previous sections. Nevertheless, a smooth assembly was only about 30 seconds. This saves a lot of assembly time.

Table 4-1 Assembly time of 10 samples

Device (smooth assembly)	Time(sec)	Device (non-smooth assembly)	Time(sec)
1	25	1	71
2	23	2	66
3	31	3	60
4	25	4	50
5	36	5	121
6	35	6	66
7	21	7	58
8	32	8	53
9	21	9	196
10	24	10	74
Average time	29.4	Average time	81.5

## 4-2 Device Measurement

The deformation of V-shaped hinges after assembly was measured by using white light interferometers. The angle measurement of assembled device is also discussed. Finally, the measurement of mirror without etch holes is presented.

### 4-2-1 V-shaped hinge measurement

The deformation of a V-shaped hinge after assembly was measured by a WYKO NT1100 interferometer. The cross section view of the V-shaped hinge after assembly is shown in Figure 4-8 (a). As discussed in Chapter 2, the V-shaped hinge was designed to bend by  $1\ \mu\text{m}$  at the tip. The SEM photograph of the V-shaped hinge after assembly is shown in Figure 4-8 (b). The interferometric measurement of the hinge bending is shown in Figure 4-9. It can be seen that the height difference between point A and point B is  $1.1\ \mu\text{m}$ , which is very close to  $1\ \mu\text{m}$  according to the design. The height difference between point C and point D is  $11.5\ \mu\text{m}$ , which is also very close to  $11\ \mu\text{m}$  according to the design.

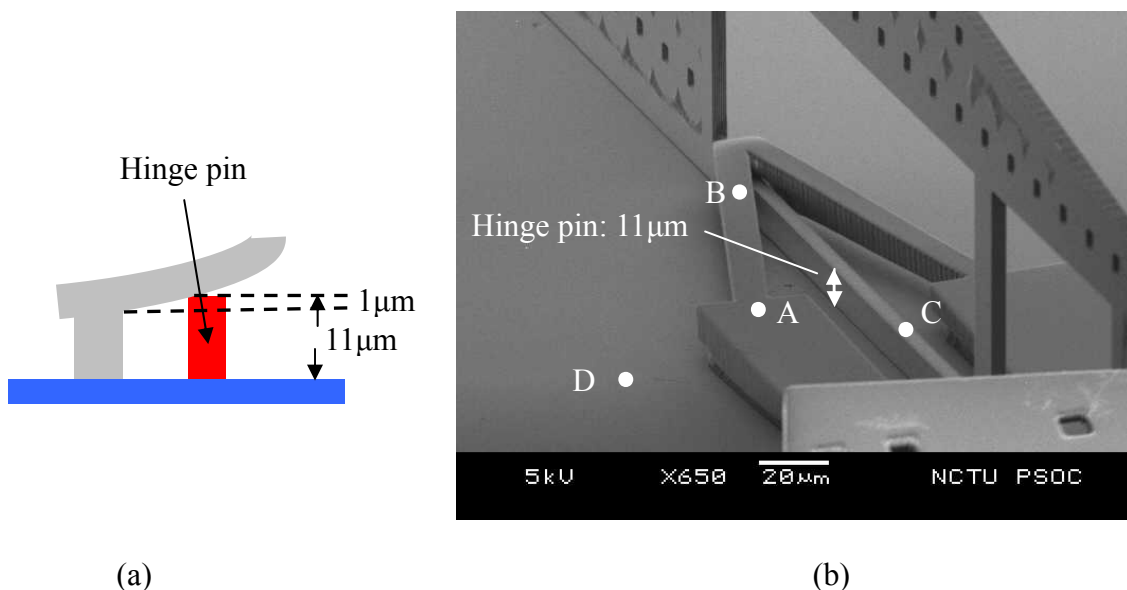
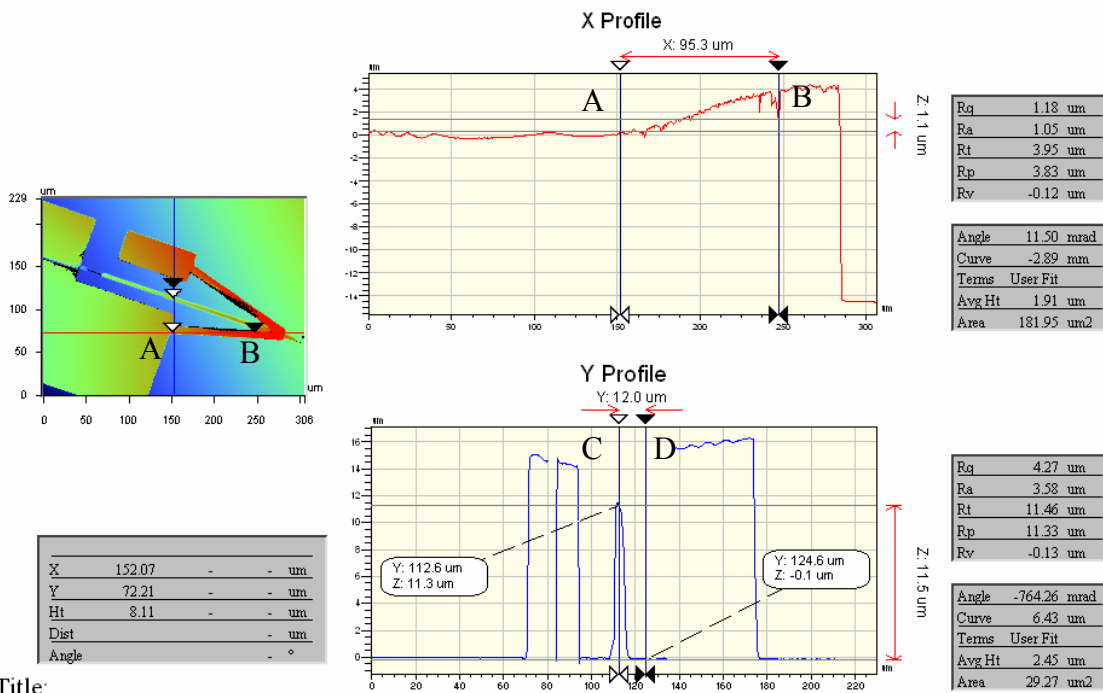


Figure 4-8 Bending of the V-shaped hinge after assembly.





Title:

Note:

Figure 4-9 Bending of the V-shaped hinge after assembly, measured by interferometry.



#### 4-2-2 Angle measurement

The devices should be ideally assembled at  $90^\circ$ . The angle measurement was made by using SEM photograph. Figure 4-10 shows the SEM photograph of an assembled sample and the geometric scale. The angle was calculated as  $89.14^\circ$ . Table 4-2 lists the angle measurement results of 6 samples randomly selected from the wafer.

The main reasons for the large deviation from  $90^\circ$  are shown in Figure 4-11. In Figure 4-1 (a), the mirror plate was not exactly locked into the center of the V-shaped slot. It was happened when the locking height was  $38 \mu\text{m}$ . The layout of this design is shown in Figure 4-11 (b). The wing plate of the  $38\text{-}\mu\text{m}$  design is too thin. It was easily bent as the mirror plate was in the upright position, as shown in Figure 4-11 (c). Another reason was the displaced hinge pins, as shown in Figure 4-11 (d). The angle error of the correctly assembled devices is about  $\pm 0.1^\circ$ .

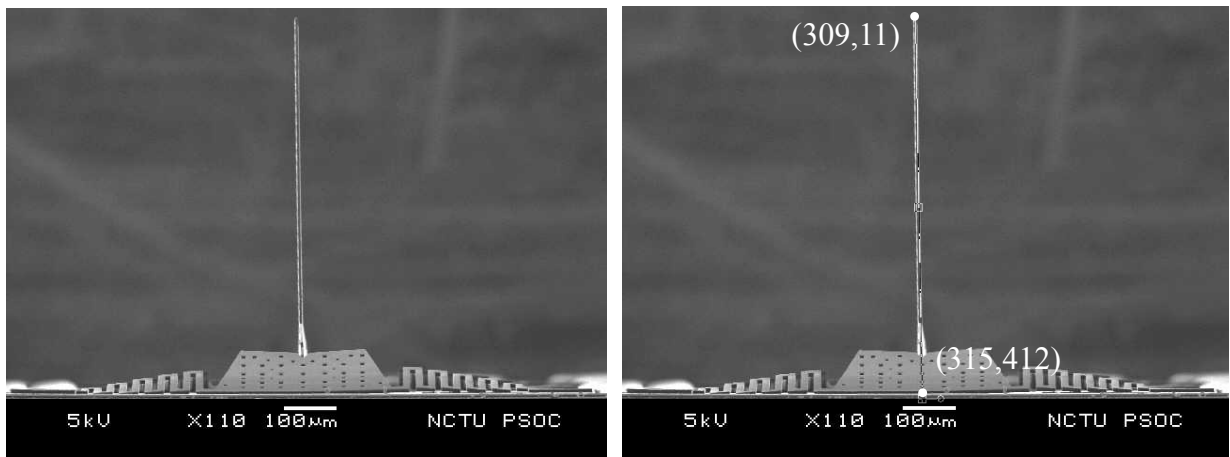
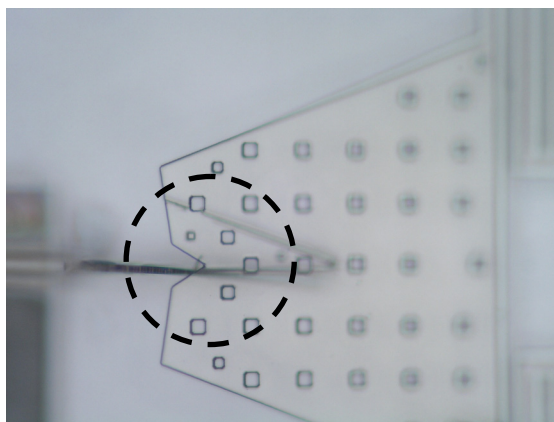


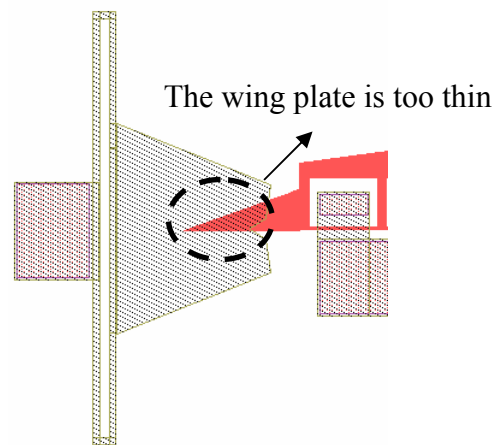
Figure 4-10 A mirror sample at 89.14°

Table 4-2 Angle measurement of 10 samples

Device	Angle measurement
1	89.14°
2	89.21°
3	89.09°
4	89.87°
5	89.12°
6	88.89°
Average angle	89.22°



(a)



(b)

Figure 4-11 Reasons of the angle deviation.



Figure 4-11 Reasons of the angle deviation (continued).

Process limitation is another issue. As shown in Figure 4-12 (a), the fabricated side plate has a step in the backside in the overlapped area between the mirror plate and the side plate. Figure 4-12 (b) show the backside topography of the fabricated side plate. As shown in Figure 4-12 (c), when the mirror plate slides into the V-shaped opening, the step feature in the backside of the V-shaped opening may cause the angle deviation from 90°.

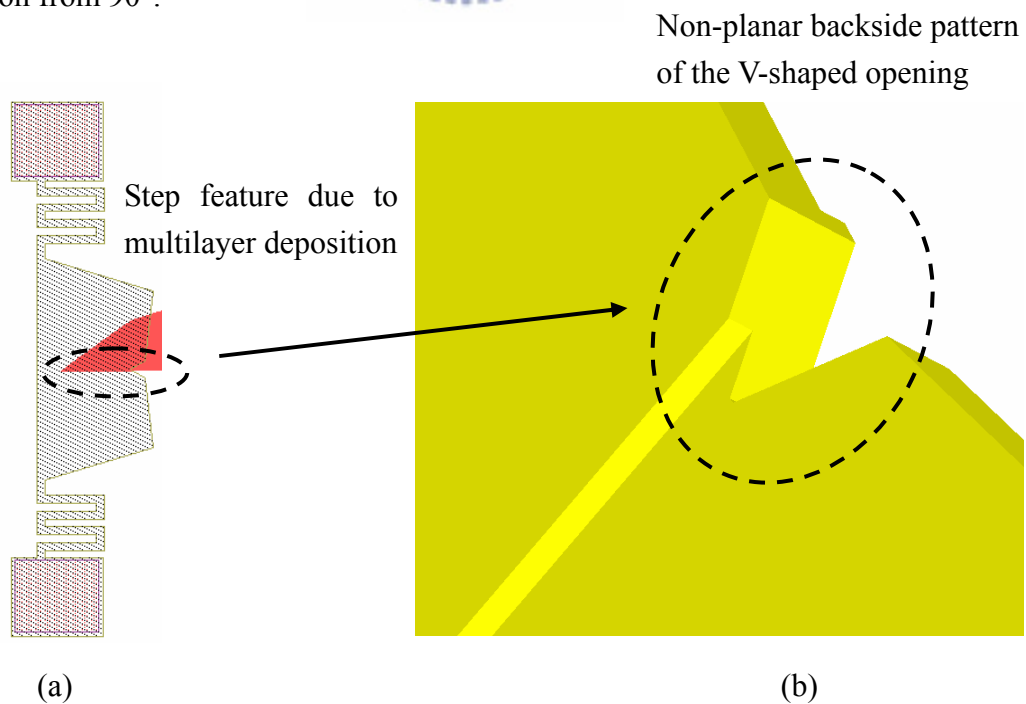


Figure 4-12 Backside step results in angle deviation.

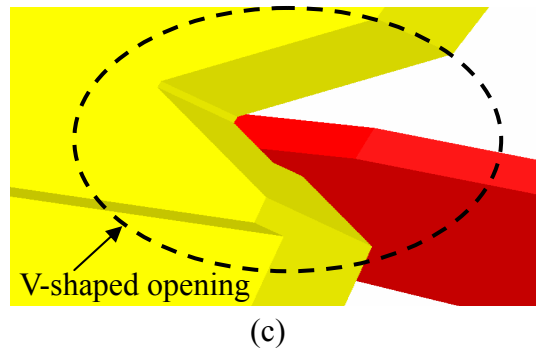


Figure 4-12 Backside step results in angle deviation (continued).

Table 4-2 shows that the six samples are assembled at angles less than  $90^\circ$ . The study of this phenomenon is in progress. More samples will be measured to clarify this problem.

#### 4-2-3 Optical measurement of mirror without etch holes

In order to eliminate the etch holes on the large mirror plate, the etching from the backside of the substrate was used. Two backside etching patterns were designed: one is a big hole and the other one is an array of pillars. As discussed in Chapter 2, the latter pattern was designed to avoid the effect of the residual stress of the buried oxide. After the ICP process, the deformations of these two designs were measured by WYKO NT1100 before the releasing process. The stress issue is discussed. Finally, the released structures were also measured and discussed.

- Before releasing

Figure 4-12 shows the photograph of a sample with the big hole backside pattern. Figure 4-11 (b) shows that the mirror plate was bended due to the residual stress of the buried oxide layer. The measurement result is shown in Figure 4-13. The radius of curvature is 9.71 mm in the x direction and 5.83 mm in the y direction. Figure 4-14 shows the photograph of a sample with the pillar array pattern. Figure 4-14 (b) indicates that the mirror plate is very flat. The WYKO measurement result is shown in Figure 4-15. The radius of curvature is 0.18 mm in the x direction and 0.19 mm in the

y direction. The measurement result verifies that this design can reduce the effect of the residual stress of the buried oxide.

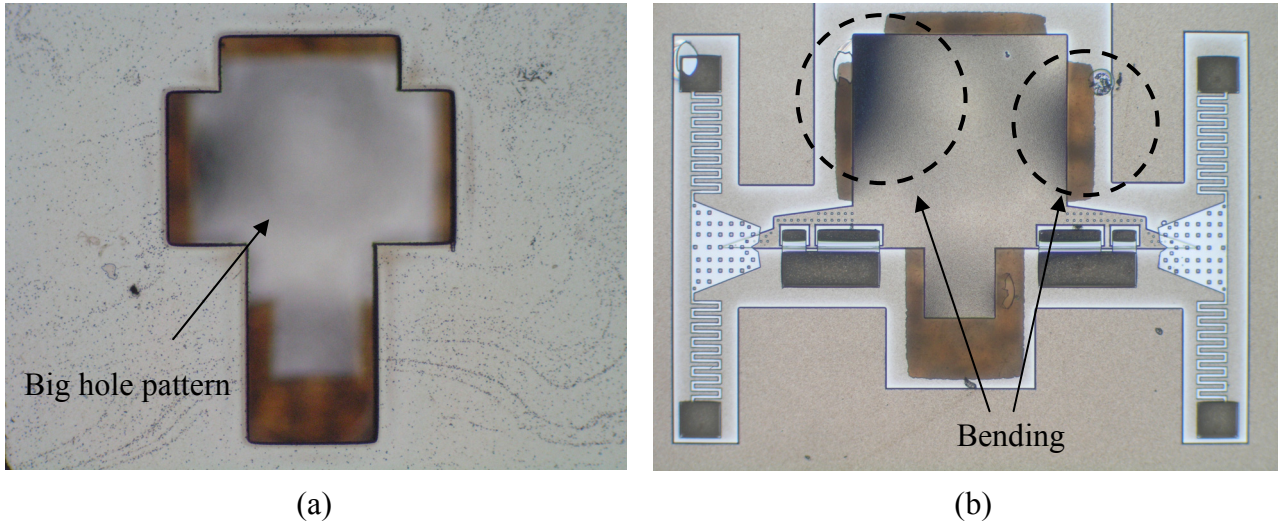
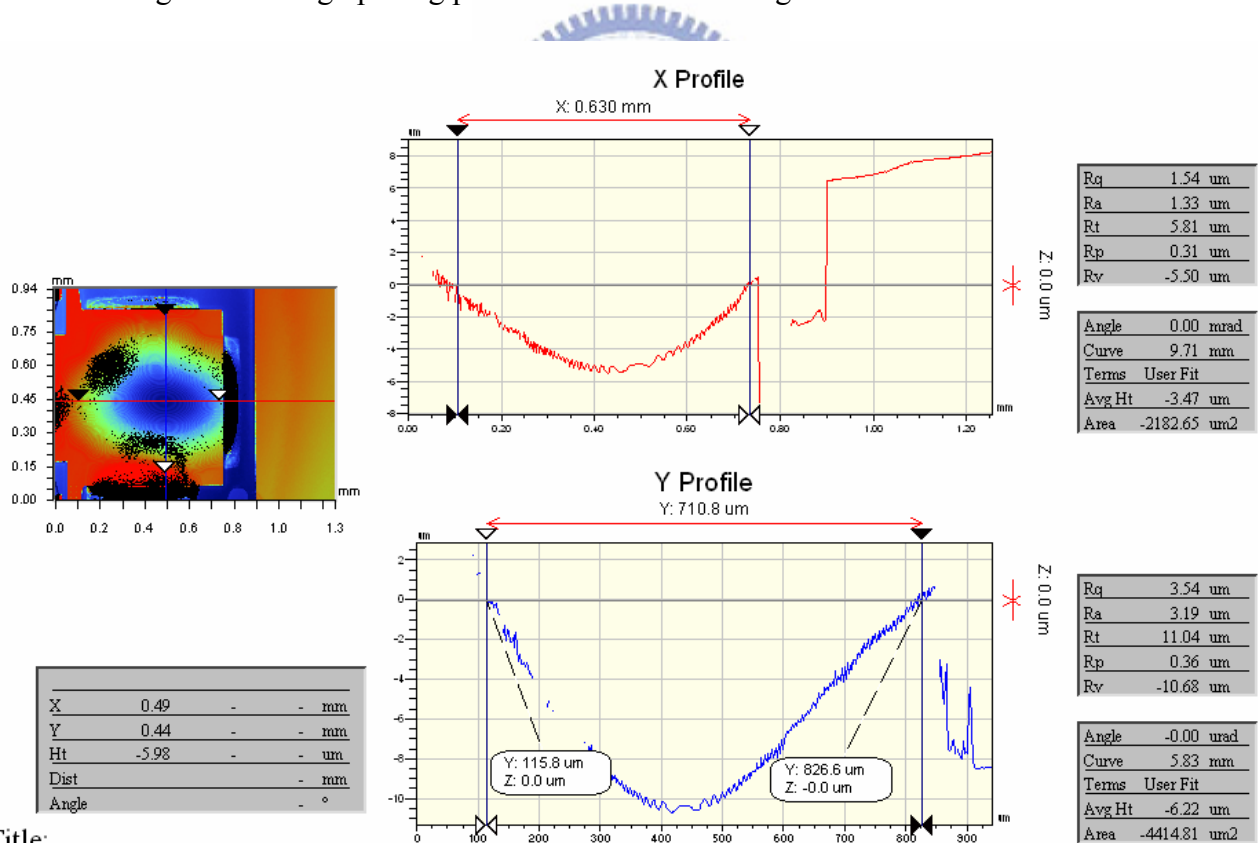


Figure 4-12 Big opening pattern causes the bending of the frontside mirror.



Title:

Note:

Figure 4-13 Mirror curvature of the device with big hole backside pattern.



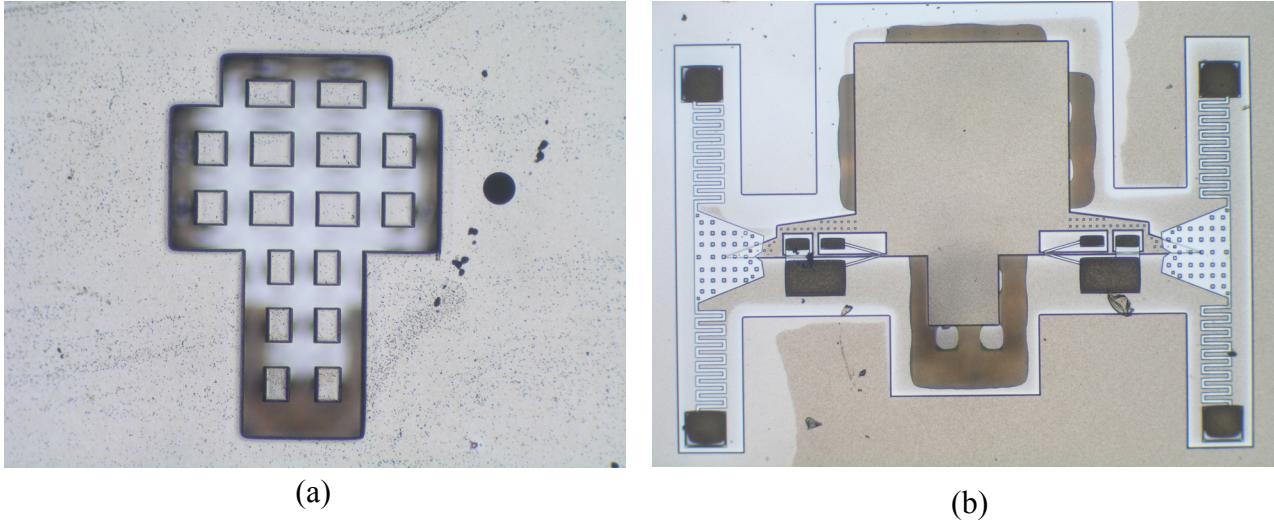
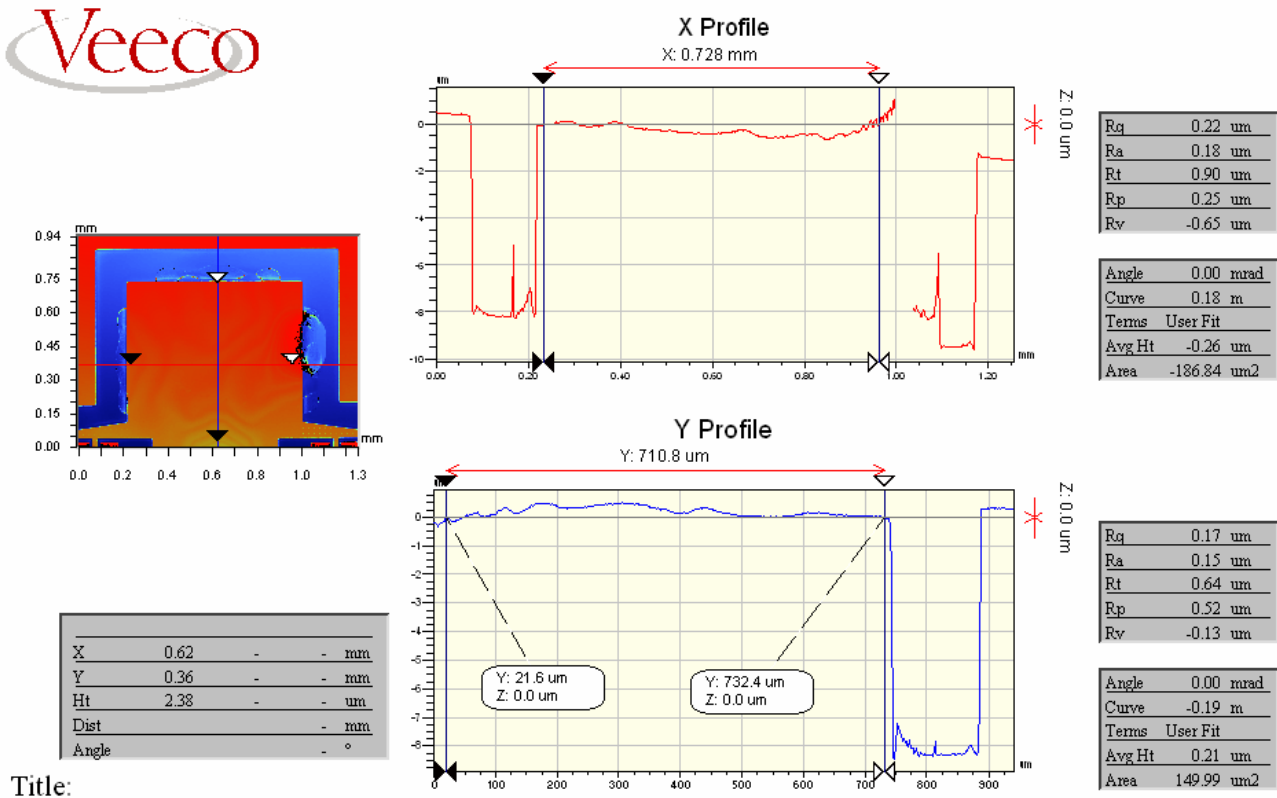


Figure 4-14 Pillar opening pattern results in flat frontside structure.



Title:

Note:

Figure 4-15 Mirror curvature of the device with pillar array pattern.

- After releasing

Figure 4-16 shows the photographs of these two samples after the releasing process. The released mirrors seem very flat. The residual stress of the buried oxide acts on the frontside mirror structure, as shown in Figure 4-12 (b), was eliminated after releasing the oxide. Therefore the mirror plate with the big hole backside pattern becomes flat. The profile of the mirror with the big hole backside pattern after releasing is shown in Figure 4-17. The radius of curvature is 0.33 m in the x direction and 0.43 m in the y direction. Figure 4-18 shows the measurement result of the mirror with the pillar array pattern after releasing. The radius of curvature is 0.51 m in the x direction and 0.23 m in the y direction.

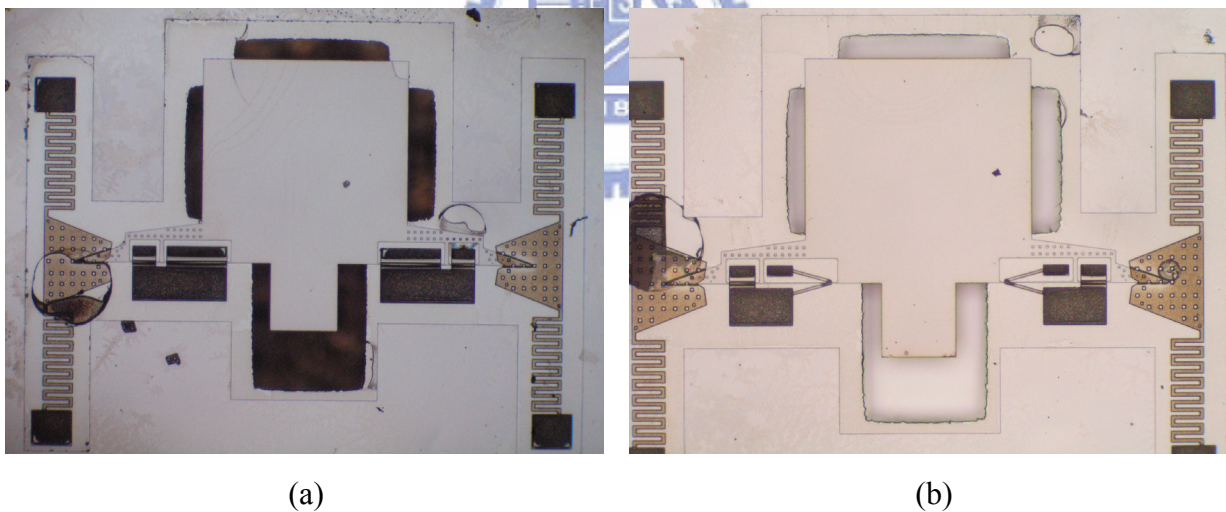
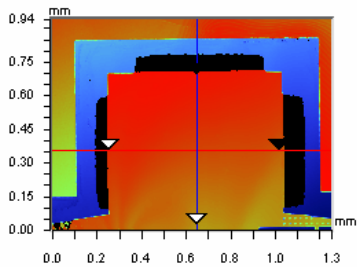


Figure 4-16 Two samples after releasing process, (a) mirror with the big hole backside pattern, (b) mirror with the pillar array pattern.

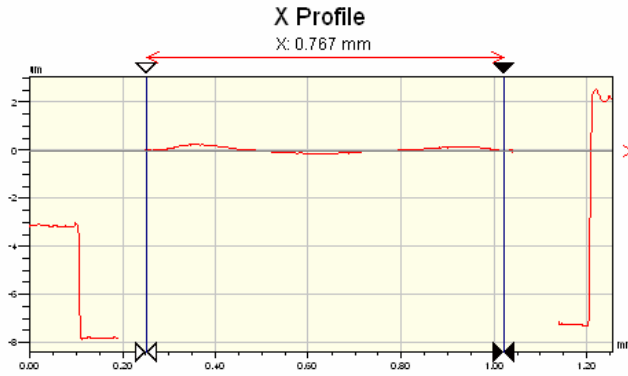




X	0.65	-	-	mm
Y	0.35	-	-	mm
Ht	1.73	-	-	um
Dist	-	-	-	mm
Angle	-	-	-	°

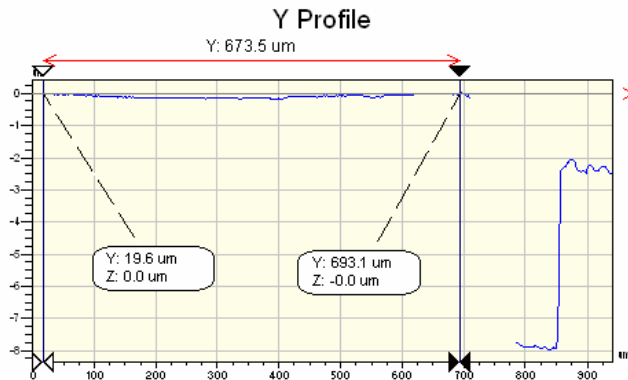
Title:

Note:



Rq	0.11 um
Ra	0.09 um
Rt	0.38 um
Rp	0.26 um
Rv	-0.12 um

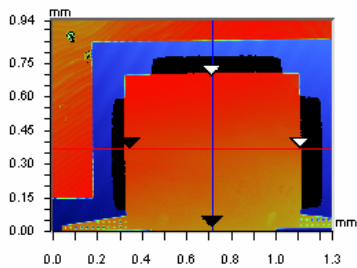
Angle	-24.44 urad
Curve	0.33 m
Terms	User Fit
Avg Ht	0.04 um
Area	30.05 um <sup>2</sup>



Rq	0.05 um
Ra	0.04 um
Rt	0.17 um
Rp	0.01 um
Rv	-0.16 um

Angle	-23.01 urad
Curve	0.43 m
Terms	User Fit
Avg Ht	-0.08 um
Area	-51.60 um <sup>2</sup>

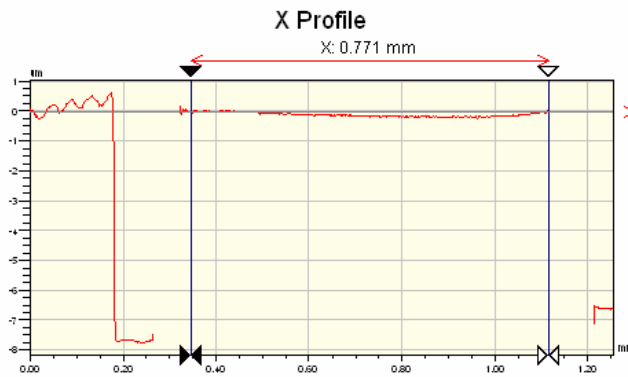
Figure 4-17 Curvature of the mirror with big hole pattern after releasing.



X	0.72	-	-	mm
Y	0.36	-	-	mm
Ht	1.42	-	-	um
Dist	-	-	-	mm
Angle	-	-	-	°

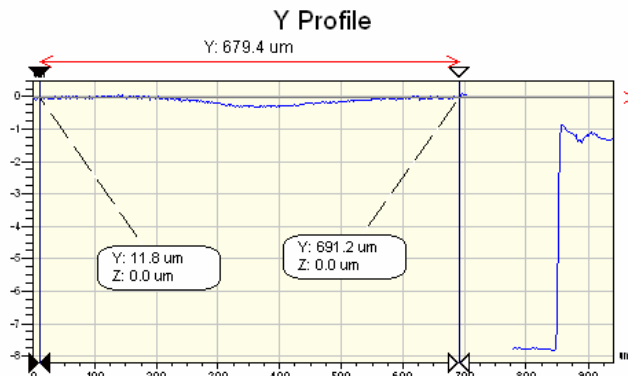
Title:

Note:



Rq	0.07 um
Ra	0.06 um
Rt	0.33 um
Rp	0.10 um
Rv	-0.23 um

Angle	0.00 mrad
Curve	0.51 m
Terms	User Fit
Avg Ht	-0.11 um
Area	-82.68 um <sup>2</sup>



Rq	0.10 um
Ra	0.09 um
Rt	0.39 um
Rp	0.07 um
Rv	-0.32 um

Angle	0.00 mrad
Curve	0.23 m
Terms	User Fit
Avg Ht	-0.09 um
Area	-62.73 um <sup>2</sup>

Figure 4-18 Curvature of the mirror with array pattern after releasing.

### 4-3 Summary

The feasibility of the proposed one-push assembly process, V-shaped hinge elements and flexible side latch plates, is verified. Some problems in the assembly process still need to be improved. The mirror plate without etch holes is also fabricated and assembled. The stress issue can be eliminated by using the pillar array backside pattern.



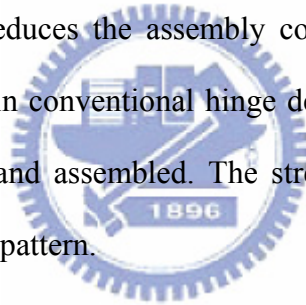
# Chapter 5

## Conclusion and Future Work

### 5-1 Conclusion

The novel fabrication process to integrated SU-8 and SOI wafer is demonstrated and used to fabricate the 90° micromirrors in this thesis. The stress-free and single-crystalline natures of the SOI device layer and the low process temperature of SU-8 makes this process ideal for integration of mechanical structures, optical devices, and circuits.

The assembly of one-push operation has been verified the feasibility. This novel assembly technique greatly reduces the assembly complexity. V-shaped hinges are proposed to address the play in conventional hinge design. The mirror plate without etch holes is also fabricated and assembled. The stress issue can be eliminated by using the pillar array backside pattern.



### 5-2 Future work

Since this is a feasibility study of the proposed structure and method, further optimization and experiments are needed to improve this technology. The devices were assembled individually in this thesis. Experiments shall be conducted in the future to demonstrate the batch assembly process.

#### 5-2-1 Device design

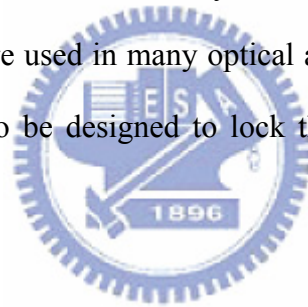
Design optimization of the side latches and the V-shaped hinges are necessary to improve the yield and accuracy of the one-time assembly process. From the observed data, all the side latch springs, whose width is 13  $\mu\text{m}$ , are too soft in the lateral

direction. A solution is to make the springs wider and enhance their rigidity.

The large angle errors after assembly can be solved by redesign the V-shaped opening and slot on the side latch so that the mirror can be more easily and accurately locked in place. The wing structure on the mirror plate is also too soft and can be bent by the side latch to cause positioning error. The optimization of the wings can be considered together with the spring design.

The lateral rigidity and vertical bending distance of the V-shaped hinges need to be considered to provide a large downward force while constrain the hinge pin from moving sideways. This can improve the accuracy of the pin position and the mirror angle.

Finally, the current design can be used only for 90° mirrors. However, 3D pop-up structures with other angles are used in many optical applications. Therefore, locking and push mechanisms need to be designed to lock the pushed-up structures at any angles.



### **5-5-2 Batch assembly**

Though the one-push operation was successfully demonstrated in this thesis, the devices were assembled individually using microprobes. This concept and process can be easily extended to batch assembly, as shown in Figure 5-1. Figure 5-1 (a) shows a push probe array similar to the pin grid arrays (PGA) widely used in IC packaging. With the position and diameter of the push pins aligned and matched to the push pads on the substrate, multiple mirrors can be assembled simultaneously by only one push operation of the array, as shown in Figure 5-1 (b). The push pin array only needs to be aligned with the relatively large push pads array with large alignment tolerance in the lateral directions. Since the push probes move vertically in the push operation and the push pads can be over pushed in the assembly process, the vertical alignment and

motion control are much eased compared to traditional techniques. These features make the one push operation a promising solution for the batch assembly of micro optical systems such as the micro optical pick-up head (Figure 5-2).

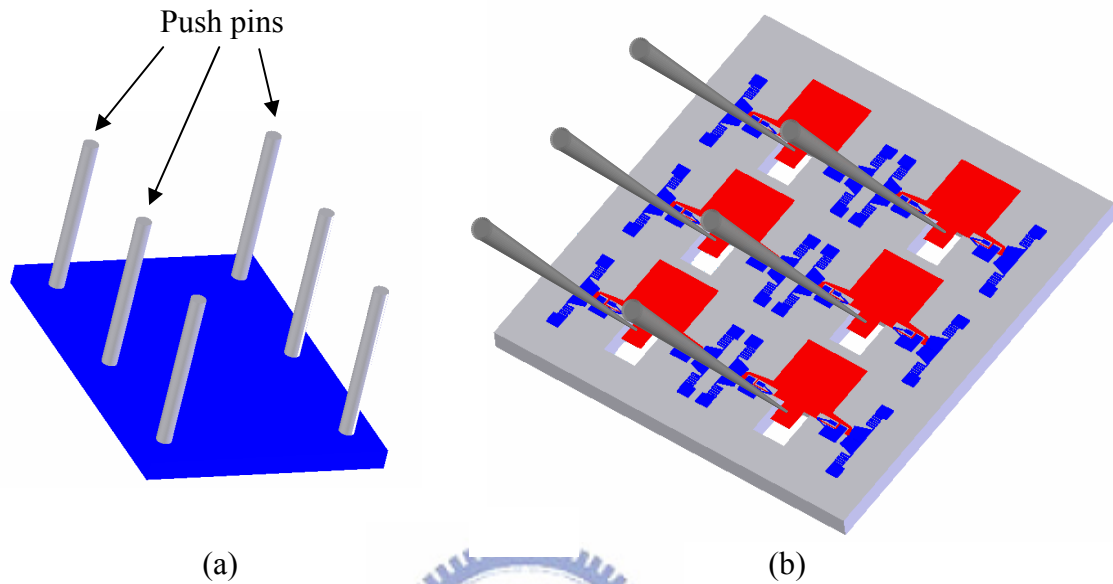


Figure 5-1 Batch assembly with one push operation, (a) push pin array, (b) one-push operation in batch

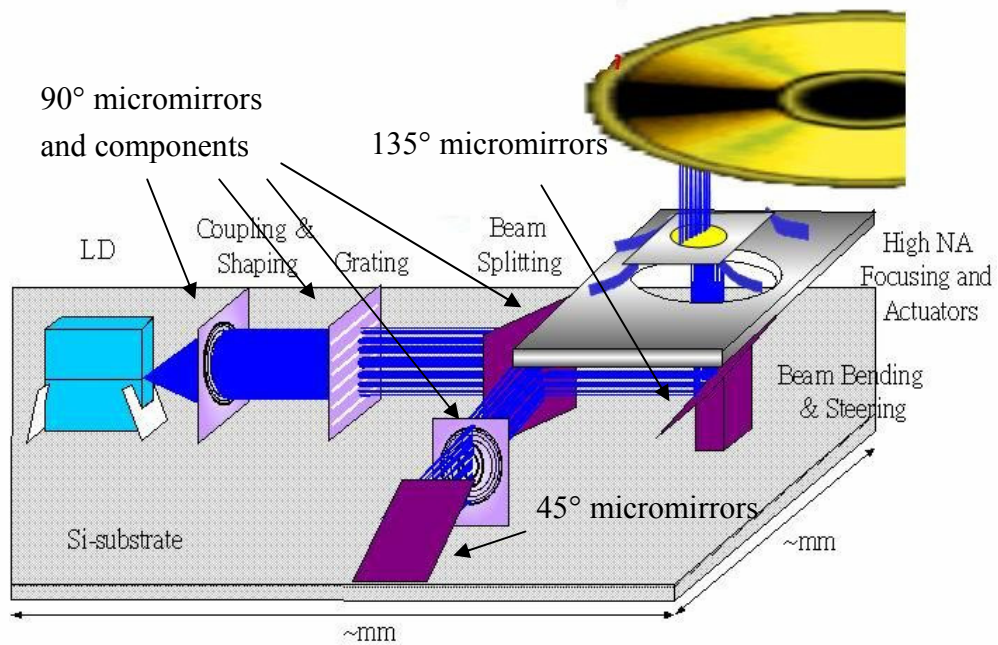


Figure 5-2 Micro optical pick-up head.

### 5-5-3 Optical components

The micromirrors without etch holes are fabricated in silicon. A high reflectivity coating, such as gold coating, is needed to enhance the reflectivity of the mirrors. However, residual stress in the metal film will induce an unwanted curvature in the mirrors, which can cause optical aberrations. A solution is to use a thicker mirror plate to increase the rigidity of the mirror. A broad range of made-to-order SCS layer thicknesses are available. An alternative approach is to compensate the curvature by depositing an oppositely stressed film of appropriate thickness. The basic concept is shown in Figure 5-3. The mirror plate is made in the SCS layer. The reflective layer provides the desired reflectivity. The corrective layer provides stress balance to eliminate the curvature of the mirror. The adhesion layer ensures that the reflective layer and corrective layer adhere to the substrate. If the reflective layer has a compressive force to make a convex curvature, a tensile corrective layer can be used to compensate this compressive force. A possible combination of layers is as such: titanium is used as the adhesion layer, the corrective layer is nickel, and gold is the reflective layer [36].



Figure 5-3 Curvature compensation by stress balance.

## Reference

- [1] G. T. A. Kovacs, N. I. Maluf, and K. E. Petersen, "Bulk micromachining of silicon," *Proceedings of the IEEE*, vol. 86, no. 8, pp. 1536-1551, 1998.
- [2] J. M. Bustillo, R. T. Howe, and R. S. Muller, "Surface micromachining for microelectromechanical systems," *Proceedings of the IEEE*, vol. 86, no. 8, pp. 1552-1574, 1998.
- [3] <http://www.dbanks.demon.co.uk/ueng/>
- [4] F. G. Tseng, "Silicon bulk micromachining" & "bioMEMS system," in *Micro Electro Mechanical Systems Technology & Application*, Precision Instrument Development Center, National Science Council, Taiwan, 2003.
- [5] D. A. Koester, "SmartMUMPs design handbook including MUMPS introduction and design rules," rev. 4, MEMS Technology Applications Center MCNC, 1996
- [6] <http://www.summitmicro.com/home/>
- [7] D. J. Young, V. Malba, J. J. Ou, A. F. Bernhardt, and B. E. Boser, "Monolithic high-performance three-dimensional coil inductors for wireless communication applications," *Electron Devices Meeting*, Technical Digest, pp. 351-354, 1997.
- [8] M. C. Wu, "Micromachining for optical and optoelectronic systems," *Proceedings of the IEEE*, vol. 85, no. 11, pp. 1833-1856, 1997.
- [9] S. H. Tsang, D. Sameoto, I. G. Foulds, R. W. Johnstone, and M. Parameswaran, "Automated assembly of hingeless 90 degree out-of-plane microstructures," *Journal of Micromechanics and Microengineering*, vol. 17, pp. 1314-1325, 2007.
- [10] G. W. Dahlmann and E. M. Yeatman, "High Q microwave inductors on silicon by surface tension selfassembly," *Electronics Letters*, vol. 36, no. 20, pp. 1707-1708, 2000.



- [11] K. S. J. Pister, M. W. Judy, S. R. Burgett, and R. S. Fearing, "Microfabricated hinges," *Sensors and Actuators*, vol. A, no. 33, pp. 249-256, 1992.
- [12] T. Akiyama and K. Shono, "Controlled stepwise motion in polysilicon microstructures," *Journal of Microelectromechanical Systems*, vol. 2, no. 3, pp. 106-110, 1993.
- [13] L. Fan, M. Wu, K. Choquette, and M. Crawford, "Self-assembled microactuated xyz stages for optical scanning and alignment," *International Conference On Solid-State Sensors and Actuators*, Chicago, pp. 319-322, 1997.
- [14] Y. W. Yi and C. Liu, "Magnetic actuation of hinged microstructures," *Journal of Microelectromechanical Systems*, vol. 8, no. 1, pp. 10-17, 1999.
- [15] W. J. Robert, "Electrostatic self-assembly of raised surface micromachined structures for optics," *Master Thesis, School of Engineering Science, Simon Fraser University*, 2000.
- [16] A. P. Hui, and W. J. Li, "Non-contact batch micro-assembly by centrifugal force," *The Fifteenth IEEE International Conference of Microelectromechanical Systems*, pp. 184-187, 2002.
- [17] R. R. A. Syms and E. M. Yeatman, "Self-assembly of fully three-dimensional microstructures using rotation by surface tension forces," *Electronics Letters*, vol. 29, no. 8, pp. 662-664, 1993.
- [18] R. R. A. Syms, E. M. Yeatman, V. M. Bright, and G. M. Whitesides, "Surface tension-powered self-assembly of microstructures - the state-of-the-art," *Journal of Microelectromechanical Systems*, vol. 12, no. 4, pp. 387-417, 2003.
- [19] N. Dechev, W. L. Cleghorn, and J. K. Mills, "Microassembly of 3-D microstructures using a compliant, passive microgripper," *Journal of Microelectromechanical Systems*, vol. 13, no. 2, pp. 179-189, 2004.

- [20] S. H. Tsang, D. Sameoto, I. Foulds, A.M. Leung, and M. Parameswaran, "Automated assembly of hingeless 90° out-of-plane microstructures," *Journal of Microelectromechanical Systems*, vol. 13, no. 2, pp. 1314-1325, 2004.
- [21] A. Friedberger and R. S. Muller, "Improved surface-micromachined hinges for fold-out structures," *Journal of Microelectromechanical Systems*, vol. 7, no. 3, pp. 315–319, 1998.
- [22] J. W. Wu, "MEMS based micro optical bench with integration of SOI and SU-8," *master thesis, Department of Electrical and Control Engineering, National Chiao Tung University*, 2006.
- [23] H. Lorenz, M. Despont, M. Fahrni, N. LaBianca, P. Vettiger, and P. Renaud, "SU-8: a low-cost negative resist for MEMS," *Journal of Micromechanics and Microengineering*, vol. 7, pp. 121-124, 1997.
- [24] D. Bachmann, B. Schoberle, S. Kuhne, Y. Leiner, and C. Hierold, "Fabrication and characterization of folded SU-8 suspensions for MEMS applications," *Sensors and Actuators A-Physical*, vol. 130, pp. 379-386, 2006.
- [25] K.Petersen, "Silicon as a mechanical material," *Proceedings of the IEEE*, vol. 70, no. 5, pp. 420-457, 1982
- [26] J. E. Sader, "Parallel beam approximation for V-shaped atomic force microscope cantilevers," *Review of Scientific Instruments*, vol. 66, no. 9, pp. 4583-4587, 1995.
- [27] R. Raymond and J. Raymond, "Roark's formulas for stress and strain," rev. 6, McGraw-Hill, 1989.
- [28] H. S. Khoo, K. K. Liu and F. G. Tseng, "Mechanical strength and interfacial failure analysis of cantilevered SU-8 microposts," *Journal of Micromechanics and Microengineering*, vol. 13 pp. 822-831, 2003.

- [29] J. Zou, M. Balberg, C. Byrne, C. Liu, and D. J. Brady, "Optical properties surface micromachined mirrors with etch holes," *Journal of Microelectromechanical Systems*, vol. 8, no. 4, pp. 506–513, 1999.
- [30] N. Belov and N. Khe, "Using deep RIE for micromachining SOI wafers," *Proceedings Electronic Components and Technology Conference 2002. IEEE*, pp. 1163-1166, 2002.
- [31] W. Chu, M. Mehregany, D. Hansford, and P. Pirouz, "Effect of thermal oxidation on the residual stress distribution throughout the thickness of p<sup>+</sup> silicon films," *Proceedings IEEE Solid-State Sensor and Actuator Workshop*, pp. 90-93, 1992.
- [32] <http://www.ece.gatech.edu/research/labs/vc/processes/rcaClean.html>
- [33] J. H. Daniel, B. Krusor, R. B. Apte, and R. A Street, "Large-area MEMS fabrication with thick SU-8 photoresist applied to an x-ray image sensor array," *Proceedings of SPIE-the International Society for Optical Engineering*, vol. 4174, pp. 40–48, 2000.
- [34] D. C. S. Bien, P. V. Rainey, S. J. N. Mitchell, and H. S. Gamble, "Characterization of masking materials for deep glass micromachining," *Journal of Micromechanics and Microengineering*, vol. 13, no. 4, pp. S34–S40, 2003.
- [35] Y. Fukuta, H. Fujita, and H. Toshiyoshi, "Vapor hydrofluoric acid sacrificial release technique for micro electro mechanical systems using labware," *Japanese Journal of Applied Physics*, vol. 42, pp. 3690–3694, 2003.
- [36] S. Guo and R. Hoffman, "Micro mirror structure with flat reflective coating," *US 6778315 B2*, Aug. 17, 2004.